

UC San Diego

UC San Diego Electronic Theses and Dissertations

Title

Applying optical forces and elastic light scattering for manipulation and analysis of biological objects

Permalink

<https://escholarship.org/uc/item/0pv063qh>

Author

Shao, Bing

Publication Date

2006

Peer reviewed|Thesis/dissertation

UNIVERSITY OF CALIFORNIA, SAN DIEGO

**Applying Optical Forces and Elastic Light Scattering for
Manipulation and Analysis of Biological Objects**

A dissertation submitted in partial satisfaction of the requirements for the degree
Doctor of Philosophy
in
Electrical Engineering (Photonics)

by

Bing Shao

Committee in charge:

Sadik C. Esener, Chair
Jules S. Jaffe, Co-Chair
Michael W. Berns
Michael J. Heller
Yu-Hwa Lo
Mihrimah Ozkan

2006

Copyright

Bing Shao, 2006

All rights reserved

The dissertation of Bing Shao is approved
and it is acceptable in quality and form for
publication on microfilm:

Co-Chair

Chair

University of California, San Diego

2006

For my beloved husband Fan, my grandparents and my parents.

Table of Contents

Signature Page.....	iii
Dedication.....	iv
Table of Contents.....	v
List of Tables and Figures.....	viii
Abbreviations and Symbols.....	xvi
Acknowledgements.....	xix
Vita and Publications.....	xxiv
Abstract.....	xxvi
1. Introduction	1
1.1. Significance	1
1.2. Scope	3
1.3. References	6
2. Light Scattering and Optical Trapping.....	8
2.1. Introduction to Light Scattering	8
2.2. Generalized Lorentz-Mie Theory (GLMT)	11
2.3. Extended GLMT for Coated Spheres	12
2.4. RM-I Method for Solid Spheroid	13
2.5. Introduction to Optical Trapping.....	19
2.5.1. Rayleigh Regime	21
2.5.2. Intermediate Regime	23
2.5.3. Mie Regime	23
2.6. Biomedical Application of Optical Traps.....	25
2.7. Summary.....	26
2.8. References	27
3. Angularly Dependent Light Scattering for Marine Microbe Characterization	30
3.1. Introduction on Light Scattering Measurement of Biological Cells	31
3.2. Background and Motivation of Marine Picoplankton Characterization.....	33

3.3.	Theoretical Modeling of Scattering from Microbes Based on RM-I and Its Extension	36
3.4.	Experimental Setup	39
3.5.	Sample Preparation.....	41
3.5.1.	Marine Microbes	41
3.5.2.	Liposome	42
3.6.	System Calibration and Validation.....	43
3.7.	Experimental Results.....	48
3.8.	Discussion.....	52
3.9.	Conclusions	53
3.10.	Acknowledgements	54
3.11.	References	55
4.	Axicon-Based Dynamically Resizable Three-Dimensional Annular Laser Trapping for Self-Propelled Cell Analysis	59
4.1.	Background and Motivation	60
4.2.	Single Point Optical Trapping for Sperm Motility Study	65
4.3.	Axicon and Its Applications	67
4.4.	Annular Laser Trap Based on Axicons	68
4.5.	Optical Design of the Annular Laser Trapping System	71
4.6.	Dynamically Resizable Annular Laser Trap	74
4.7.	Effect of Beam Profile on Trapping Performance.....	77
4.8.	Experiments with Annular Laser Trap Based on One Axicon.....	79
4.8.1.	Experimental Setup	79
4.8.2.	Three-dimensional Annular Trapping of Microspheres and Biological Cells.....	83
4.9.	Sperm Sorting and Analysis with the Annular Laser Trap.....	88
4.9.1.	Specimen Preparation	88
4.9.2.	Sperm Sorting	88
4.9.3.	Dynamic Monitoring of Sperm Swimming Behavior Change under Laser Trap.....	92
4.10.	Experiments with Resizable Annular Laser Trap.....	102
4.10.1.	Experimental Setup	102
4.10.2.	Experimental Result	104
4.11.	Discussion.....	105
4.12.	Conclusions	106
4.13.	Acknowledgements	107
4.14.	References	108
5.	Microscope-Integrated Micromanipulator Based on Multiple VCSEL Traps	112
5.1	Background and Motivations	113
5.2	Effect of beam symmetry and power clipping on laser trapping performance	115
5.3	Optical system design.....	122

5.3.1	Two-Dimensional Agile Laser Tweezers Array.....	122
5.3.2	Depth Adjustable Laser Tweezers.....	125
5.3.3	Independent Control of Multiple Laser Tweezers.....	127
5.4	Experiments.....	128
5.4.1	Experimental Setup.....	128
5.4.2	Sample Preparation.....	130
5.4.3	Experimental Results.....	130
5.5	Discussion.....	134
5.6	Conclusions.....	136
5.7	Acknowledgements.....	136
5.8	References.....	137
6.	Conclusions and Outlook.....	140
6.1.	Conclusions.....	140
6.2.	Innovative Contributions.....	143
6.2.1.	Submicron cell characterization with angularly dependent light scattering.....	143
6.2.2.	Annular laser trap for self-propelled cell analysis.....	144
6.2.3.	Micromanipulator based on multiple VCSEL traps.....	145
6.3.	Further Directions.....	145
6.4.	References.....	150

List of Tables and Figures

Tables:

Table 3-1: Three types of marine picoplankton to be studied, their scientific names, microscopy images, brief descriptions, and corresponding models for simulation.	36
Table 3-2: Extended RM-I for coated spheroids with three typical core geometries.	38
Table 4-1: Motility parameters measured by sperm tracking program.	89
Table 4-2: Percentage of tested sperm showing responses consistent to expectation (decreased motility when being trapped at a higher laser power, for a longer period, or affected by an external object).	102

Figures:

Figure 2-1: Scattering by an obstacle.	8
Figure 2-2: Scattering by an arbitrary sphere.	12
Figure 2-3: Core-shell model for extended GLMT. 1-core, 2-shell, a -radius of the core, b -radius of the entire coated sphere.	13
Figure 2-4: Schematic diagrams of RM-I, showing the modified laboratory coordinate system, the incident (I_0) and the scattered (I_s) beams, the orientation of the spheroid particle is determined by γ and ψ . Θ is the scattering angle, and δ is the angle of the spheroid orientation with respect to the bisectrix (BS).	15
Figure 2-5: The angular dependent scattering diagram of a spheroid with parameters of $a=0.3 \mu\text{m}$, $v=2$, $n_p=1.406$ in a medium of $n_m=1.339$ at different orientation (γ, ψ). Left: orientations of the spheroid, pink lines with arrows represent the long axis of the spheroid. Right: scattering diagrams in polar coordinate.	16
Figure 2-6: Definition of scattering angle θ and azimuthal angle φ	20
Figure 2-7: Three-dimensional optical trapping of a sphere.	22

Figure 2-8: Diagram demonstrating the direction of the force due to refraction (F_D) and reflection (F_R) for two rays incident on a dielectric sphere that is offset from the optical axis.	25
Figure 3-1: Schematics of optical setup used to record scattering diagrams from particles suspended in the cuvette.	40
Figure 3-2: Simulated scattering diagram from liposome with diameters of (a) 30 nm, (b) 200 nm, (c) 250 nm, and (d) 400 nm. All the four simulations use the coated sphere model as presented in Figure 3-3.	45
Figure 3-3: Coated sphere model for liposome scattering simulation, t ---the thickness of the lipid bilayer.	46
Figure 3-4: Scattering diagram of the log-normal-diameter-polydispersed liposome suspension with 30 nm nominal diameter in PBS1 \times solution. (a) Simulation based on extended GLMT of coated sphere. (b) Experimental curve.	47
Figure 3-5: Scattering diagrams of polystyrene microspheres with diameter of 0.6 μm , 0.8 μm and 1.0 μm , respectively. (a) Simulation with GLMT on intermediate-sized sphere. (b) Experimental measurements on low-concentration suspensions.	48
Figure 3-6: Scattering diagrams of <i>Synechococcus sp.</i> strain CC9311. (a) Simulation with RM-I method on a homogenous spheroid with $0.8\times 0.8\times 2.0$ μm outer dimensions ($a= 0.4$ μm , $\nu=2.5$ as in the spheroid equation) and $n_p=1.406$ in seawater ($n_m=1.339$). (b) Experimental measurements on low-concentration suspensions of <i>Synechococcus sp.</i> strain CC9311	49
Figure 3-7: Scattering diagram of <i>Flavobacterium sp.</i> strain ALC1. (a) Simulation with RM-I on a homogenous spheroid with $1.0\times 1.0\times 3.5$ μm outer dimensions ($a= 0.5$ μm , $\nu=3.5$ as in the spheroid equation), and $n_p=1.406$ in seawater ($n_m=1.339$). (b) Experimental measurements on low-concentration suspensions of <i>Flavobacterium sp.</i> strain ALC1.	50
Figure 3-8: Scattering diagram of <i>Ostreococcus sp.</i> strain CCE9901. (a) Simulation with extended RM-I on a coated spheroid with $1.0\times 1.0\times 2.0$ μm outer dimensions ($a= 0.5$ μm , $\nu=2$ as in the spheroid equation) and a concentric spherical core of radius 0.25 μm . ($n_1=1.40$ for the spherical core, $n_2=1.37$ for the shell) in seawater ($n_m=1.339$). (b) Experimental measurements on low-concentration suspensions of <i>Ostreococcus sp.</i> strain CCE9901.	51

Figure 3-9: Improved elliptical mirror design that is compatible with index matching liquid and self-aligned to the cuvette.	53
Figure 4-1: Optophoresis, schematic diagram. An optical gradient is imaged into the sample well. The well is translated at constant velocity past the stationary gradient to produce a moving optical gradient with respect to the cells. A cell experiences forces induced by the moving optical gradient, dissipative forces due to its relative motion with respect to the aqueous medium in which it is suspended and the surface of the well, and buoyancy-corrected gravity, as shown in the inset. ⁶	61
Figure 4-2: Optophoresis of blood cells. (a) Sample well containing cancer cells and normal red blood cells. (b) A scanning laser line is introduced to the sample well and three red blood cells are attracted to the optical gradient field. (c) All cells are trapped by the scanning laser line and move with it to the bottom of the field of view. (d) As the scanning laser line move faster, trapped cells significantly displace from the center of the gradient field. (e) Normal red blood cells all fall out of the trap and stay near the bottom of the field of view, while cancer cells stay in the trap. (f) Cancer cells are moved to the top of the field of view by the scanning laser line. (Courtesy of Genoptix, Inc.)	63
Figure 4-3: Interference to single trap sperm analysis introduced by non-targeted sperm. (a) A sperm (inside the white circle) is trapped by a single spot laser trap (indicated by the white dotted cross hair) for analysis. (b) A second sperm (inside the white square) swims towards the trapping spot. (c) The second sperm swims into the trapping spot, and interferes with the analysis of the first trapped sperm. (d) Both sperm swim out of the trap.	67
Figure 4-4: The axicons, also known as conical lenses or rotational symmetrical prisms. (a) photo (courtesy to Del Mar Photonics, Inc.), (b) schematic diagrams showing the cross-section of an axicon. R_{Ax} is the radius of the axicon, and H_{Ax} is the height of the conic surface. ²⁵	68
Figure 4-5: Applying a ring-shaped laser trap to facilitate sperm analysis. (a) A ring trap works as a force shield to protect sperm held by single point laser trap from interference introduced by other untrapped sperm. (b) In sperm motility and chemotaxis research, weak sperm with low swimming power and low response to central attractant are held back by the optical gradient field of the ring trap. (c) A sperm with strong response to the central attractant develops an above-threshold swimming force to pass through the ring trap and reach the attractant in the center of the ring.	70

Figure 4-6: Schematic diagram of the optics designed for annular laser trapping (not to scale), MO---Microscope Objective.	72
Figure 4-7: ZEMAX simulations of axicon-based ring trap system. (a) System layout. (b) Spot diagram at the specimen plane shows the size and quality of the ring focus. (c) Huygens PSF cross-section shows a strong gradient of light intensity on the specimen plane. (d) Close-up of the system layout near the specimen plane gives a cross-section view of the ring focus formation, only negligible amount of rays failed to focus due to coma.	74
Figure 4-8: Under a fixed total laser power, with increased ring size (from (a) to (c)), the average trapping power per sperm is reduced, thus more sperm can escape the annular trap and reach the center (assuming there is an attractant at the center of the ring).	75
Figure 4-9: Schematic diagram of the optics designed for resizable annular laser trapping (not to scale), MO---Microscope Objective.	76
Figure 4-10: ZEMAX simulations of adjustable annular laser trap with 63× NA1.40 oil immersion objective. (a) Layout, focus close-up, and sample plane spot diagram for maximal ring size, (b) Layout, focus close-up, and sample plane spot diagram for minimal ring size.	77
Figure 4-11: Effect of input beam intensity distribution on trapping performance of the ring. (a) For a Gaussian input, whose intensity decreases from the center, the beams after the axicon have a non-uniform and non-symmetrical intensity patterns. (b) The phase distribution on the specimen plane after the objective is not symmetrical. (c) The intensity distribution on the back focal plane of the objective (specimen plane). (d) For a top-hat incident with uniform intensity, each beam emerging from the axicon in one azimuthal angle incident the objective lens with a uniform intensity. (e) The phase distribution on the specimen plane after the objective is symmetrical. (f) The intensity distribution on the specimen plane after the objective.	79
Figure 4-12: The schematic diagram of the annular laser trapping system. M1-M7---Mirrors, TL1---Telescope lens 1, TL2---Telescope lens 2, FL---focusing lens, TL---Tube lens.	81
Figure 4-13: Photo of the single axicon annular trapping system. Inset: close up of the specially mounted dichroic.	82
Figure 4-14: Sequences of video frames showing (a), (b) a ring of trapped 5 μm silica beads being moved in the transverse direction, and then (c), (d) being lifted 100 μm in the axial direction.	84

Figure 4-15: Geometrical structure of the annular trap: experiment and simulation. (a) objective height $z=46\ \mu\text{m}$, (b) $20\ \mu\text{m}$, (c) $0\ \mu\text{m}$, (d) $-20\ \mu\text{m}$, and (e) $-46\ \mu\text{m}$. (f) ZEMAX simulation. Left: the cross-section of light rays in the chamber when $z=0\ \mu\text{m}$; right: the spot diagrams at the center of the chamber when the objective is at different heights corresponding to (a)-(e).	86
Figure 4-16: 3-D trapping of a human sperm. (a), (b) The trapped sperm near the top of the ring is moved in the transverse direction, and (c), (d) lifted in the axial direction.	87
Figure 4-17: Parallel sperm sorting with annular laser trap when the estimated average laser power is 25 mW per sperm. (a) The mean value of VCL, VAP and ALH for “fast” and “slow” sperm from a population of 83 sperm. (b) The statistics VCL and VAP distribution of all the 83 sperm.	91
Figure 4-18: Tens of sperm are stopped along the ring focus.	92
Figure 4-19: Guiding two sperm along the ring under an estimated average laser power of 25 mW per sperm. (a) Two sperm are freely swimming in opposite directions close to the ring (big red circle). (b) Affected by the optical gradient force from the ring trap, the two sperm start swimming along the curvature of the ring, one clockwise (green circle), the other counterclockwise (orange circle). (c) The two sperm continue swimming in opposite direction. (d) After swimming along the ring for about 180° , the two sperm are about to collide with each other. (e), (f) After collision, one sperm (green circle) is knocked out of the focus, while the other (orange circle) keeps swimming along the ring.	93
Figure 4-20: Swimming parameter change in an example of “power binary”, where a repeatable reduction/recovery of VAP, VCL, and ALH is observed as the sperm is swimming along/released from the ring trap.	95
Figure 4-21: Swimming parameter change in an example of “power gradient”, where an increase of VAP and VCL is observed with a decrease of the trapping power.	96
Figure 4-22: Swimming parameter change in an example of “fatigue”, where a decrease of VAP and VCL is observed after the sperm is swimming along the ring for more than 20 seconds. Both VAP and VCL increase after the sperm is released.	97
Figure 4-23: Swimming parameter change in an example of “load”, where a decrease of VAP, VCL and ALH is observed after the sperm starts pushing cell	

debris while swimming along the ring. All three parameters increase when the trapping power is decreased.	98
Figure 4-24: Swimming parameter change in an example of “block”, where a decrease of VAP, VCL and ALH is observed after the sperm’s forward movement along the ring is stopped by a dead sperm. All three parameters increase when the sperm is released.	99
Figure 4-25: Sequences of images showing a sperm pushing cell debris while it is swimming along the ring trap. (a) Frame #8, under a laser power of 25 mW per sperm, a sperm (green circle) is swimming along the ring (big red circle) counterclockwise, while a piece of cell debris is trapped by the ring (orange circle). (b) Frame #92, right before the sperm touches the debris. (c), (d) Frame #115 and #199, the sperm keep swimming along the ring by pushing the debris forward. (e), (f) Frame #385 and #469, the laser power is reduced to 20 mW per sperm, the sperm keep swimming along the ring with the load. The time interval between (a) and (b), (c) and (d), (e) and (f) are same, therefore the change of sperm swimming velocity could be clearly seen by examine the difference of circumferential displacement of the sperm, which is in agreement with Figure 4-22.	100
Figure 4-26: Sequences of images showing a sperm blocked by a dead sperm while it is swimming along the ring trap. (a), (b) Frame #1 and #51, under a laser power of 23 mW per sperm, a sperm (green circle) is swimming along the ring (big red circle) clockwise. A dead sperm stuck to the glass is on the ring (orange circle). (c), (d) Frame #325 and #375, the sperm encounters the dead sperm and could not keep moving forward. (e), (f) Frame #425 and #475, after the laser is turned off, the sperm changes its head orientation, bypasses the dead sperm and swims away. The time intervals between (a) and (b), (c) and (d), (e) and (f) are the same, therefore the change of sperm swimming velocity could be clearly seen by examining the difference of circumferential displacement of the sperm, which is in agreement with Figure 4-23.	101
Figure 4-27: Experimental setup of the dynamically adjustable annular laser trap. M1-M7---Mirrors, TL1---Telescope lens 1, TL2---Telescope lens 2, FL---focusing lens, TL---Tube lens.	103
Figure 4-28: Photo of the dynamically adjustable annular laser trapping system.	104
Figure 4-29: Size tunability. (a) At original axial position of Axicon 2, the diameter of the ring trap is 70 μm . (b) When Axicon 2 is shifted to the left for 10 mm, the ring diameter increases to 140 μm . (c), (d) ZEMAX simulated	

layout, focus close-up, and sample plane spot diagram for (a) and (b).
 Axi1---Axicon 1; Axi2---Axicon 2; Axi3---Axicon 3; FL---Focusing
 Lens; TL---Tube Lens; MO---Microscope Objective.105

Figure 5-1: The back aperture and back focal plane of a microscope objective in optical trapping. (A) Trapping beam pivots around the back aperture to maximize the NA while beam symmetry cannot be maintained. (B) Trapping beam pivots around the back focal plane to maintain beam symmetry while the effective NA is considerably reduced.117

Figure 5-2: Asymmetric beam experiment with a fixed microscope objective. (a) Experimental setup, (b) Power throughput vs. tilting angle.119

Figure 5-3: Asymmetric beam experiment with movable microscope objective. (a) Experimental setup, (b) Power throughput vs. tilting angle.121

Figure 5-4: Experimental schemes for beam deflection. (A) Mirror is tilted upward and trapping beam is tilted downward. (B) Mirror is not tilted and trapping beam is normal to the specimen plane. (C) Mirror is tilted downward and trapping beam is tilted upward. L_a – first telescope lens; L_b – second telescope lens, MP—multiplexing plane, MOBA -- microscope objective back aperture, MO – microscope objective, SP – specimen plane.123

Figure 5-5: Experimental scheme for agile optical tweezers array. CL – collimating lens, L_a -- first telescope lens, L_b -- second telescope lens, MOBA -- microscope objective back aperture.125

Figure 5-6: Depth adjustment in laser tweezers. (a) Lens pair with adjustable spacing in front of the telescope system. (b) Depth adjustment of objective focus. D_{in} – input beam diameter, D_M – beam diameter at multiplexing plane.126

Figure 5-7: Experimental setup of microscope-integrated micromanipulator based on VCSELs. CL 1, CL 2---collimating lenses, $\lambda/2$ ---half wave plate, PBS---polarizing beam splitter.129

Figure 5-8: Depth adjustment of VCSEL tweezers while trapping a 5 μm polystyrene microsphere. (A) Trapping at the maximal depth, which is about 7 μm under the origin on the specimen plane. (B) Trapping at the original depth, which corresponds to the location of the specimen plane. (C) Trapping at the minimal depth, which is about 7 μm above the specimen plane.131

Figure 5-9: Intra-array shift of a 4 μm bead in DI water. Inset: corresponding ON VCSEL in the 4 μm VCSEL array.	131
Figure 5-10: 4 μm VCSEL array used for microscope-integrated manipulator. (A) Layout of an ideal VCSEL array with all 16 VCSEL illuminating. (B) In the VCSEL array we used, only those VCSELs marked as black have appropriate polarization direction (polarization orthogonal to that of the single VCSEL used in the system). (C) VCSELs selected for the demonstration of micromanipulator.	132
Figure 5-11: Frames from micromanipulation experiment. (A) Initial state, (B) - (D) Single VCSEL tweezers collects 3 yeast cells and form them into a predefined array trapped by a VCSEL tweezers array, (E) - (G) Cell group is transported by agile VCSEL tweezers array, (H) - (J) Cell group is disbanded by single VCSEL tweezers.	133
Figure 5-12: Cell rotation with VCSEL tweezers. (A1-A5) Rotation of a pair of yeast cells counter-clockwise with double VCSEL traps. (B1-B5) Rotation of a PC-12 cell counter-clockwise with double VCSEL traps.	134
Figure 6-1: Utilizing annular trapped microspheres to impose spatial confinement to cell dividing. (a) A single cell before dividing. (b) - (c) The mother cell is dividend into two daughter cells and then four cells. (d) Due to the spatial confinement imposed by the trapped microspheres, the cells stop dividing. (e) - (f) After the size of the ring is increased, there is more room for cell dividing, and the four cells resume dividing into eight cells.....	148
Figure 6-2: Utilizing annular trapped microspheres to impose external obstacle for 3T3 cell migration. (a) - (b) Four 3T3 cells are migrating around the ring of microspheres. (c) Part of the ring trap is blocked so that the fence of microspheres is broken. (d) Without the trapped microspheres as obstacle, 3T3 cells start migrating into the ring.	149
Figure 6-3: Expanding the dimension and resolution of VCSEL tweezers array. (a) Interlacing two 4 μm VCSEL tweezers array. (b) Scanning two 1 μm VCSEL tweezers array independently in two orthogonal directions.	150

Abbreviations and Symbols

Abbreviations:

AI ---Artificial Insemination

ALH --- Amplitude of Lateral Head Displacement

AOD --- Acoustooptical Deflectors

CASA --- Computer Aided Sperm Analysis

CGH --- Computer Generated Hologram

DI H₂O --- Deionized Water

DMEM --- Dulbecco's Modified Eagle Medium

DOPC --- 1,2-Dioleoyl-*sn*-Glycero-3-Phosphocholine

EOD --- Electrooptical Deflectors

FBS --- Fetal Bovine Serum

FDTD --- Finite Difference Time Domain

GLMT --- Generalized Lorentz-Mie Theory

HTF--- Human Tubal Fluid

IMS --- Initial Motility Score

LUVET --- Large Uni-lamellar Vesicles prepared by Extrusion Techniques

MEMS---Micro-Electro-Mechanical System

MO --- Microscope Objective

MOBA -- Microscope Objective Back Aperture

MOT% --- Initial Motility

MP—Multiplexing Plane

NA --- Numerical Aperture

NSOM --- Near-field Scanning Optical Microscopy

PBS --- Phosphate Buffered Saline

PMT --- Photomultiplier Tube

RM-I --- A hybrid of Rayleigh-Debey method and Generalized Lorentz-Mie Theory

RPM---Revolutions Per Minute

SIL --- Solid Immersion Lens

SNR --- Signal to Noise Ratio
SOP --- Speed of Progression
SP – specimen plane
SSS --- Serum Substitute Supplement
VAP --- Smooth Path Velocity
VCL --- Curvilinear Velocity
VCSEL --- Vertical Cavity Surface Emitting Laser

Symbols:

a --- radius
 α --- azimuthal angle
 a_n and b_n --- scattering coefficients
 c --- speed of light in vacuum
 ϵ_0 --- the permittivity of free space
 f --- focal length of lens
 F_D --- optical force on dielectric particle due to diffraction
 F_G --- optical gradient force
 F_O --- radiation pressure force
 F_P --- photonic force
 F_R --- optical force on dielectric particle due to refraction
 F_S --- optical scattering force
 h --- Planck's constant
 η --- dynamic viscosity
 I --- intensity
 k --- wave vector (wave number)
 λ - wavelength
 m - mass of object
 M - magnification power of microscope objective
 n - index of refraction
 p_S --- the pitch on the specimen plane

p_{VA} --- the pitch on the VCSEL array

P_d - dipole moment

π_n and τ_n --- angle-dependent functions

θ - scattering angle or inclination angle

$\sigma\langle S \rangle$ --- scattering cross-section of the particle

V_C - critical velocity (optical tweezers force measurements)

Ω --- solid angle

ω_0 - beam waste of focused Gaussian beam

x --- particle size parameter

Acknowledgements

During my education at UCSD, I have had the fortune to be able to interact and collaborate with many wonderful people. Here I would like to thank them for their help and understanding.

First of all, I would like to express my sincere gratitude and appreciation to my advisor Prof. Sadik Esener, who has always inspired me to work on novel and challenging projects. Besides contributing many ideas that led directly to the research described herein, Dr. Esener has provided me with space, flexibility and freedom during research while providing support and guidance. He has given helpful advices and shown his care for not only my work but also my life here in a foreign country, and for that I shall always be grateful.

I would like to thank Dr. Jules Jaffe for his financial support and guidance when it was needed most. He has brought new and interesting ideas to my scattering project and helped me solve problems with intense discussions.

I would like to express my deep gratitude to Prof. Michael Berns who has been accommodating me with lab space, equipment and biological samples for my sperm trapping project. Dr. Berns' preciseness and passion in research have given me a lot of inspiration for my own research career.

Another person with whom I hold in very high regard is Prof. Mihrimah Ozkan, who has always stood by me, given me advice and encouragement in graduate research, and helped me in paper writing. I feel very lucky to have a mentor like her.

I am very grateful to Prof. Michael Heller and Prof. Yu-Hwa Lo for being my thesis committee and showing their encouragement to my research.

Sanja Zlatanovic deserves a good deal of credit in my research success at UCSD. We collaborated closely on the VCSEL array trapping project, where she proved to be a strong and capable collaborator who often provided direct strengths where I had weaknesses. I appreciated not only the discussion from her which brought me good ideas for research but also the steadfast friendship with her.

Jaclyn Nascimento is another collaborator whom I would like show special acknowledgement for her assistance with my sperm trapping project. In spite of being a junior researcher, she has been very helpful in getting the research completed. She has always proved eager, willing and competent in carrying out whatever research tasks were at hand. Her companionship and presence in the lab bring a lot of joyfulness to experiments, and her friendship has made my life more colorful.

As an excellent mentor, Dr. Elliot Botvinick has never stopped showing earnest interest in my work and throwing brilliant ideas to guide me through my research when it was needed most.

Deqiang Song has been a true friend and colleague in the past 5 years, always willing to discuss and help. His experience in research and passion in learning new things has been whipping me to work harder and improve myself continuously.

It is a pleasure to be able to work with Prof. Mirianas Chachisvilis, who proved to be a wonderful advisor in my scattering project. It is he who established the base of

the scattering project, and gave me great advice on not only theory but also experiments.

To those who paved the path for my optical trap research in our group, Richard Flynn, Aaron Birkbeck, Mark Wang thank you for laying the groundwork for what came later.

To Linda Shi, a postdoc in Dr. Berns' lab, who has always cared about my progress and made my experiment more fun and effective with her cool Labview programs.

To two postdocs in our group that help to guide and supervise me in my work at UCSD, Pengyue Wen and Matthias Gross, thank you both for being willing to listen and give advice and guidance when it was needed on matters both practical and theoretical.

On a personal level, I would like to thank my family for their support over the years. To my supportive and lovely husband, Fan Chang, who has always believed in me, been willing to listen to me, share the happiness and sadness with me, and helped me whenever I needed. Words cannot adequately express the depth of my love and appreciation. To my loving grandparents, my life would have been totally different without your excellent nurturing and education during the first 15 years. And you have always been the most important driving power in my study and life. And thanks to my parents, who have always had so much confidence in me, shown so much interest in my research, thank you for the guidance and support you have provided me over the years.

To everyone whom I have forgotten to write down, not for depth of feeling but failing of memory. Thank you for being there for me over the years, and enriching my life and happiness in innumerable ways.

This work was in collaboration with Scripps Institute of Oceanography, and Beckman CRES research center of the San Diego Zoological Society. Thanks Prof. Brian Palenik, Prof. Bianaca Brahamsha, and Xavier Mayali from Prof. Farooq Azam's lab for providing marine microbe samples.

Sections 4.5 --- 4.7 of Chapter 4 are, in part, reprints of material as it appears in "Dynamically adjustable annular laser trapping based on axicons," by B. Shao, J. M. Nascimento, E. L. Botvinick, M. W. Berns, S. C. Esener, *Applied Optics*, in press, 2006, and in "Axicon-based annular laser trap for sperm activity and chemotaxis study," by B. Shao, J. M. Vinson, E. L. Botvinick, S. C. Esener, M. W. Berns, Proceedings of the SPIE, v5930, 0D, SPIE 50th Annual Meeting, San Diego, California, USA, Jul. 31-Aug. 4, 2005. The dissertation author was the primary co-author and co-investigator of these papers.

Section 5.2 --- 5.4 of Chapter 5 is, in part, a reprint of material as it appears in "Microscope-integrated micromanipulation based on multiple VCSEL traps," by B. Shao, S. Zlatanovic, and S. C. Esener, Proceedings of the SPIE, v5514, p62, SPIE 49th Annual Meeting, Denver, Colorado, USA, Aug. 2-6, 2004. The dissertation author was the primary investigator and first author of this paper.

Section 5.3 --- 5.4 of Chapter 5 is, in part, a reprint of material as it appears in "Manipulation of microspheres and biological cells with multiple agile VCSEL traps," by B. Shao, S. Zlatanovic, M. Ozkan, A. Birkbeck, and S. C. Esener, *Sensors and Actuators, B, Chem*, v113, n2, p866-874, 2006. The dissertation author was the primary investigator and first author of this paper.

Vita

- 1999 B.S. in Precision Instrument, Measurement and Control Technology,
Tsinghua University, Beijing, P. R. China
- 1999-2001 M.S. in Optical Engineering, Tsinghua University, Beijing, P. R. China
- 2001-2006 Graduate Student Researcher, University of California, San Diego
- 2006 Ph.D. in Electrical Engineering (Photonics), University of
California at San Diego
- Ph.D. Dissertation Title: “Applying Optical Forces and Elastic Light
Scattering for Manipulation and Analysis of Biological Objects”

Publications

Journal Papers

1. B. Shao, J. M. Nascimento, E. L. Botvinick, M. Ozkan, M. W. Berns, S. C. Esener, “Size tunable three-dimensional annular laser traps based on axicons,” submitted to *Optics Letters*.
2. B. Shao, L. Z. Shi, J. M. Nascimento, E. L. Botvinick, M. Ozkan, M. W. Berns, S. C. Esener, “High-throughput sorting and fertility analysis of human-sperms with a ring-shaped laser trap,” to be submitted.
3. B. Shao, J. S. Jaffe, M. Chachisvilis, B. Palenik, S. C. Esener, “Angular resolved light scattering for discriminating among marine picoplankton: modeling and experimental measurements,” to be submitted.
4. B. Shao, J. M. Nascimento, E. L. Botvinick, M. W. Berns, S. C. Esener, “Dynamically adjustable annular laser trapping based on axicons,” *Applied Optics*, in press, 2006.
5. B. Shao, S. Zlatanovic, M. Ozkan, A. Birkbeck, and S. C. Esener, “Manipulation of microspheres and biological cells with multiple agile VCSEL traps,” *Sensors and Actuators, B, Chem*, v113, n2, p866-874, 2006.
6. R. A Flynn, B. Shao, M. Chachisvilis, M. Ozkan, S. C. Esener, “Counter-propagating optical trapping system for size and refractive index measurement of microparticles”, *Biosensors and Bioelectronics*, v21, n7, p1029-1036, 2006.

7. R. A. Flynn, B. Shao, M. Chachisvilis, M. Ozkan, S. C. Esener, "Two-beam Optical Traps: Refractive Index and Size Measurements of Microscale Objects", *Biomedical Microdevices*, v7, n2, p93-97, 2005.
8. R. A. Flynn, A. L. Birkbeck, M. Gross, M. Ozkan, B. Shao, M. M. Wang, and S. C. Esener, "Parallel transport of biological cells using individually addressable VCSEL arrays as optical tweezers", *Sensors and Actuators, B, Chem* v87, p239-243, 2002.

Conference Papers

1. B. Shao, J. S. Jaffe, M. Chachisvilis, B. Palenik, S. C. Esener, "Discrimination of Marine Picoplankton with Angularly Resolved Light Scattering Signatures: Modeling and Measurements," Ocean Optics XVIII, Montreal, Quebec, 9-13 October, 2006.
2. B. Shao, J. M. Vinson, E. L. Botvinick, S. C. Esener, M. W. Berns, "Axicon-based annular laser trap for sperm activity and chemotaxis study", Proceedings of the SPIE, v5930, 0D, SPIE 50th Annual Meeting, San Diego, California, USA, Jul. 31-Aug. 4, 2005.
3. B. Shao, J. M. Vinson, E. L. Botvinick, D. Song, S. Zlatanovic, S. C. Esener, M. W. Berns, "Dynamically Adjustable Annular Laser Trapping for Sperm Chemotaxis Study", OSA Topical Meetings, Information Photonics, ITuC4, Charlotte, North Carolina, USA, June 6-9, 2005.
4. B. Shao, S. Zlatanovic, and S. C. Esener, "Microscope-integrated micromanipulation based on multiple VCSEL traps", Proceedings of the SPIE, v5514, p62, SPIE 49th Annual Meeting, Denver, Colorado, USA, Aug. 2-6, 2004.
5. R. A. Flynn, A. L. Birkbeck, M. Gross, M. Ozkan, B. Shao, D. Song, S. C. Esener, "Simultaneous transport of multiple biological cells by VCSEL array optical traps", Optics in Computing, Washington, D.C., June 19, 2003.

Book Chapter

1. B. Shao, J. M. Nascimento, L. Z. Shi, and E. L. Botvinick, "Automated Motile Cell Trapping and Analysis Automated Motile Cell Capture and Analysis with Optical Traps", *Laser Manipulation of Cells and Tissues: Methods in Cell Biology* edited by M. W. Berns and K. O. Greulich, Academic Press, Elsevier Inc., in press.

Awards

Cal(IT)² Fellowship, 2001-2002

ABSTRACT OF THE DISSERTATION

Applying Optical Forces and Elastic Light Scattering for Manipulation and Analysis of Biological Objects

by

Bing Shao

Doctor of Philosophy in Electrical Engineering (Photonics)
University of California, San Diego, 2006

Sadik C. Esener, Chair
Jules S. Jaffe, Co-Chair

Non-invasive manipulation and analysis of biological objects with high resolution and efficiency have become extremely important. This dissertation presents three novel techniques based on light scattering and optical forces, which could bring high resolution and speed to submicron cell characterization, improve the throughput and functionality of self-propelled cell analysis and enhance the parallelism, portability and flexibility of cell manipulation instruments.

Elastic light scattering is used for submicron cell characterization. An important problem in oceanic microbial ecology is characterizing the constituents of the sea. To pursue this goal, the application of angularly-dependent light scattering on oceanic microbe differentiation has been explored. Good overall agreement is found

between scattering patterns simulated with developed models and those experimentally measured. The distinct scattering patterns of different species provide fingerprint information that will allow for routine identification of marine picoplankton.

Optical tweezers have been used not only for manipulating cells, viruses and organelles within cells, but also measuring biological forces on the order of picoNewtons. In the second part of this dissertation, a three-dimensional resizable annular laser trap is developed for self-propelled cell manipulation and analysis. This system offers high power efficiency and is potentially useful for high-throughput multi-level sperm sorting based on motility and chemotaxis. With only tens of milliwatts devoted to each sperm, this new type of laser trap offers a gentle way to study the effect of optical force, laser radiation and external obstacles on sperm swimming patterns and membrane potential in detail. Applications could be extended to motility and biotropy studies on other self-propelled cells, such as algae and bacteria, etc.

The third part of this dissertation involves manipulation of multiple biological cells both synchronously and independently. Substituting Vertical Cavity Surface Emitting Lasers (VCSELs) for standard diode and gas lasers in optical micromanipulation provides the ability to meet the miniaturization and parallelism demands of current lab-on-a-chip technologies, so that multiple experiments can be performed in parallel and at low costs. By combining a single VCSEL trap that can

move individual particles in 3-D with a VCSEL trap array, a micromanipulator capable of multi-step group operating and cell rotating is constructed.

1. Introduction

1.1. Significance

As people are getting more and more concerned about their living quality and environment, non-invasive biomedical analysis with high resolution and high efficiency becomes extremely important. The advance of the technologies for manipulation and analysis of biological objects on the microscale holds the promise of improving research in biomedical field, such as disease diagnosis and treatment, cell characterization and sorting. With its wavelength in the range of hundreds nanometers to one micron, light has shown its unique capabilities in interacting with biological objects and extracting useful information from them.

One important phenomenon induced by light-matter interaction, light scattering, is the secondary radiation emitted by dipoles that compose the matter under illumination by a primary radiation. When a cell is illuminated, the spatial distribution of the scattered light intensity is dependent on the cell's size, shape, refractive index, density, and morphology. Based on this theory, cell types, or more importantly cell states could be differentiated by examining the scattered light in appropriate angular ranges. Currently as the most popular cell sizing technique, flow cytometry has been used to identify biological cells with similar shapes according to the differences in the forward and side-scattered light and fluorescence properties,¹ which requests cell labeling with fluorescence dyes. In this dissertation, we show that the label-free angularly-dependent elastic light scattering measurements on low-concentration cell

suspensions could also be used for differentiation subgroups in picoplankton, which have very similar sizes and shapes.

As light deflection induced by local variation in refractive index, scattering results in photon momentum change, and thus optical force on particles. The axial optical force arises from the difference between total momentum and the forward momentum carried by the scattered light. One important application of optical force is laser trapping. As a noninvasive and microfluidic-compatible biomedical tool, laser trapping in the near infrared regime has been widely applied for manipulation and physiological study of biological cells² and organelles.³ More recently, calibrated optical traps have been used for the measurement of picoNewton forces involved in biological systems, such as those generated by molecular motors⁴ or by sperm while swimming.⁵ These cell-based measurements demonstrate the possibility of analyzing single cells based on optical force.

With the increasing exploration of the manipulation, sorting and analysis capabilities of optical trapping technologies, and its rapid merging with micro-fluidic systems, where the channel size is only on the order of 10 to 100 μm , there are always demands on high throughput, multi-functionality, portability, and low cost systems which could provide new information for biomedical applications.

This dissertation will discuss two novel optical trapping systems which would bring new information and improvement toward the manipulation, sorting and analysis of biological objects. First, we introduce a new type of optical trapping --- a ring-shaped laser trap based on axicons, which can be used to manipulate tens to hundreds

of biological cells in parallel and shows promise for high-throughput, multi-level sorting of self-propelled cells such as sperm according to their motility and biotropism response. It is free from mechanical scan which introduces a tangential drag force on the sample, as well as offers almost 100% power efficiency which is much higher than that of diffractive optics. With only tens of milliwatts devoted to each sperm, this new type of laser trap offers a more gentle way for sperm analysis and laser-sperm interaction study. Secondly, toward more parallel system, the flexibility and throughput of cell manipulation are improved with multiple VCSEL traps. The microscope-integrated micromanipulator was designed and developed to realize both synchronous and independent laser trapping on a static sample plane. Consisting of a single 3-D agile VCSEL tweezers and an array of VCSEL tweezers, the system is capable of independent control, rotation, and batch processing of biological cells.

1.2. Scope

The problem to be studied is “noninvasive manipulation and analysis of biological objects with optical scattering techniques.” The two approaches I use are “angularly dependent scattering” and “micromanipulation with optical forces.” Three optical systems have been developed to provide new information (submicron to micron-sized cell characterization, self-propelled cell analysis) and improvement (high throughput) to the current techniques of biological objects manipulation and analysis.

Chapter 2 focuses on explaining the basic physics of light scattering and optical trapping. In sections 2.1, the theory of light scattering in three size regimes will be reviewed. In section 2.2-2.4, Generalized Lorentz-Mie Theory (GLMT) for

solid sphere and its extension to coated-sphere and solid spheroid are introduced. Section 2.5 gives an overview on optical trapping theory. Various physical models are introduced that are commonly employed to describe optical traps in different size regimes. In section 2.6, the applications of optical traps in biomedical research are briefly overviewed. Finally, a summary of the chapter is given in section 2.7.

Chapter 3 studies the application of elastic light scattering for submicron to micron-sized cell characterization. After the introduction on light scattering measurement of biological cells in section 3.1 and the background of marine picoplankton characterization in section 3.2, the theoretical modeling based on GLMT and its extension is addressed in section 3.3, and a new simulation method is developed to model nonspherical eukaryote cells. Section 3.4 depicts the experimental setup of the scattering measurement system. The sample preparation procedures for marine microbes and liposome are described in section 3.5. In section 3.6, system calibration with liposome and validation with standard submicron microspheres of three different sizes are carried out. In section 3.7, angularly dependent light scattering from suspensions of three types of marine picoplankton in seawater is measured respectively and compared with simulation results. Following section 3.8, where potential solutions for system improvement are discussed, the chapter ends with conclusions drawn in section 3.9.

Chapter 4 introduces the dynamically resizable three-dimensional annular laser trap based on axicons. Following the background and motivation addressed in section 4.1, section 4.2 gives a review on the application of optical trapping for sperm motility

study, discuss the limitation of the current single point laser trapping approach. Section 4.3 introduces the axicon and its conventional applications in beam shaping, atom cooling and axial trapping. In section 4.4, the novel optical trapping system based on axicons is proposed and compared with alternative approaches of forming a ring-shaped laser trap. Our system can not only be used to manipulate tens to hundreds of microparticles in parallel, but also promise high-throughput, multi-level sorting of self-propelled cells such as sperm according to their motility and biotropy response. Section 4.5 goes through the optical design of the single-axicon system and shows the ray-tracing simulation results. Section 4.6 extends the system to a dynamically-adjustable annular laser trap with two additional axicons. In section 4.7, the effect of incident beam profile on the performance of the ring-shaped trapping is analyzed, and beam shaping is proposed accordingly. Section 4.8 illustrates the experiments with a single axicon on microspheres. Parallel three-dimensional trapping of microparticles are carried out and the optical forces in both transverse and axial directions are measured. Section 4.9 demonstrates parallel sorting and swimming pattern analysis of sperm with the annular laser trap. Section 4.10 proves the feasibility of dynamically-adjustable ring trap with microspheres. Section 4.11 discusses the application of the system for multi-level self-propelled cell sorting based on motility and biotropy and section 4.12 ends the chapter with conclusions.

Chapter 5 describes the utilization of VCSEL and VCSEL arrays to forming stable three-dimensional optical traps which can independently and synchronously manipulate biological cells without moving sample plane. Section 5.1 addresses the

motivation of this research and gives a brief review on previous research on VCSELs traps. Section 5.2 examines the effect of beam symmetry and power clipping on laser trapping performance, suggests the optical design guideline for the micromanipulator based on multiple VCSELs. Section 5.3 goes through the optics design of a three-dimensional agile VCSEL trap, an agile VCSEL trap array and system integration of a micromanipulator based on an independently controlled VCSEL and VCSEL array. Section 5.4 demonstrates the experiments on microspheres and biological cells with the micromanipulator. Optical forces are calculated from the experimental results. Finally, section 5.5 discusses potential applications of the VCSEL-based micromanipulator and section 5.6 concludes the chapter.

Chapter 6 summarizes the thesis work and concludes by suggesting several future research directions. Potential contributions of this work to the field of biological and medical engineering are discussed.

1.3. References

1. D. Marie, F. Partensky, S. Jacquet, and D. Vaultot, "Enumeration and Cell Cycle Analysis of Natural Populations of Marine Picoplankton by Flow Cytometry Using the Nucleic Acid Stain SYBR Green I," *Appl. Environ. Microbiol.* **63**(1), 186-193 (1997).
2. M. Ozkan, M. M.Wang, C.Ozkan, R. A. Flynn, and S. Esener, "Optical manipulation of objects and biological cells in microfluidic devices," *Biomedical Microdevices* **5**, 47-54 (2003).
3. M. W. Berns, "Laser scissors and tweezers," *Scientific American (International Edition)* **278**, 52-57 (1998).
4. C. F. S. K. Svoboda, B. J. Schnapp, and S. M. Block, "Direct observation of kinesin stepping by optical trapping interferometry," *Nature (London)* **365**, 721-727 (1993).

5. W. H. W. Y. Tadir, O. Vafa, T. Ord, R. H. Asch, M. W. Berns, "Force generated by human sperm correlated to velocity and determined using a laser generated optical trap," *Fertil. Steril.* **53**, 944-947 (1990).

2. Light Scattering and Optical Trapping

2.1. Introduction to Light Scattering

Scattering of light waves by any system is related to the heterogeneity of the system. Matter is composed of dipoles (pairs of electric charges), which when illuminated by an incident light (Figure 2-1), are set into oscillatory motion by the electric field of the incident wave. Accelerated dipoles radiate electromagnetic energy in all directions; this secondary radiation is called scattering.¹

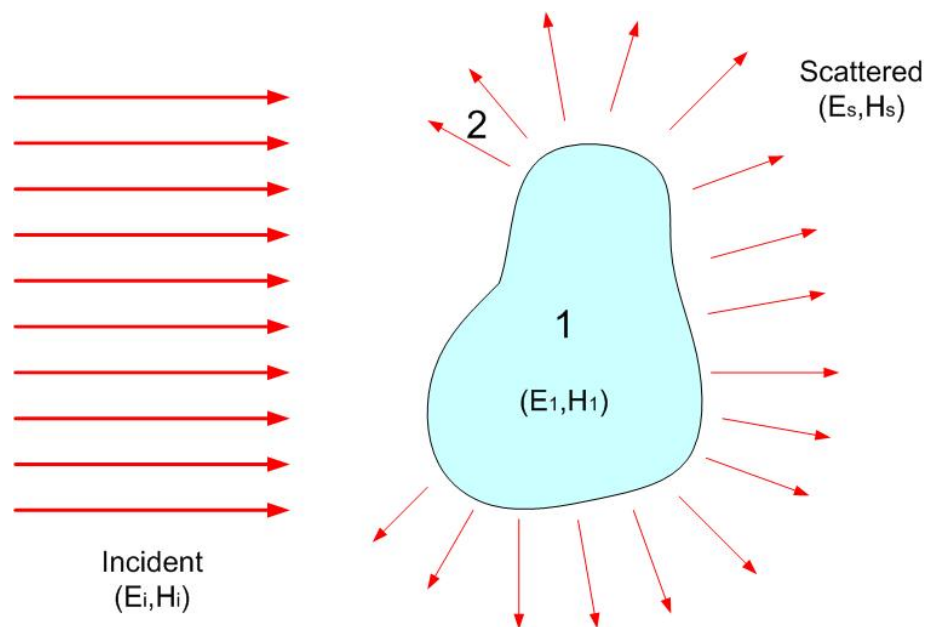


Figure 2-1: Scattering by an obstacle.

In addition to reradiating, the excited dipoles may transform part of the incident electromagnetic energy into other forms of energy, e.g. thermal energy. This process is called absorption.¹ Both scattering and absorption remove energy from a beam of light traversing the medium. This attenuation is called extinction.²

The types of non-uniformities that can cause scattering, known as scatterers or scattering centers, includes particles, bubbles, droplets, defects in crystalline solids, surface roughness, cells in organisms, etc. The effects of such features on the path of light can be described in the framework of light scattering theory.

In physical descriptions of scattering, physicists commonly distinguish between two broad types, elastic and inelastic. Elastic scattering involves negligible loss or gain of energy by the radiation. Inelastic scattering, however, involves some change in the energy of the radiation. When radiation is only scattered by one localized scattering center, this is called single scattering. When the scattering centers are grouped together, the radiation may scatter many times, which is known as multiple scattering. In this dissertation, we will only consider elastic light scattering from single particles.

Scattering theory from single particles can be divided into three size regimes, very small particles can be modeled with Rayleigh approximation, geometrical optics is applicable to large particles, while problems for intermediate-sized particles have to be rigorously solved.

Rayleigh scattering is a process in which electromagnetic radiation (including light) is scattered by a small spherical volume of variant refractive index, such as a

particle. In order for Rayleigh's model to apply, the sphere must be much smaller in diameter than the wavelength λ of the scattered wave; typically the upper limit is taken to be about 1/10 the wavelength. In this size regime, the exact shape of the scattering center is not very significant and can often be treated as a sphere of equivalent volume.³

Scattering by spheres larger than the Rayleigh range is usually known as Mie scattering. In the Mie regime, the shape of the scattering center becomes much more significant and the Generalized Lorentz-Mie theory (GLMT) only applies well to spheres. No general closed-form solution is known for arbitrary shapes.

When the ratio of particle diameter to wavelength is more than about 10, the laws of geometric optics are mostly sufficient to describe the interaction of light with the particle, which makes the modeling of large particle scattering much easier.

For modeling of scattering in cases where the Rayleigh and Mie models do not apply, such as irregularly shaped particles, there are many numerical methods that can be used. The most common are finite-element methods which solve Maxwell's equations to find the distribution of the scattered electromagnetic field. Sophisticated software packages exist which allow for the user to specify the refractive index or indices of the scattering feature in space, creating a 2- or 3-dimensional model of the structure. For relatively large and complex structures, these models usually require substantial execution times on a computer.

2.2. Generalized Lorentz-Mie Theory (GLMT)

Generalized Lorentz-Mie Theory is a rigorous solution for light scattering by an isotropic sphere of arbitrary size in a homogeneous media. A spherical particle with radius a and refractive index n_p is illuminated with a linearly polarized light field ($\mathbf{E}_i, \mathbf{H}_i$) whose vertical and parallel electric field could be defined as $\mathbf{E}_{i\perp} = \sin \phi$, and $\mathbf{E}_{i\parallel} = \cos \phi$ (Figure 2-2), by solving the vector wave equation $\nabla^2 \mathbf{E} + k^2 \mathbf{E} = 0$ and $\nabla^2 \mathbf{H} + k^2 \mathbf{H} = 0$, with appropriate boundary conditions: $(\mathbf{E}_i + \mathbf{E}_s + \mathbf{E}_1) \times \hat{\mathbf{e}}_r = (\mathbf{H}_i + \mathbf{H}_s + \mathbf{H}_1) \times \hat{\mathbf{e}}_r = 0$, where the subscript i stands for incident field, s stands for scattered field, and 1 stands for internal field, the scattered field is expressed by these two equations,

$$E_{\perp} = -\frac{i}{kr} e^{-ikr+i\omega t} \sin \phi \sum_{n=1}^{\infty} \frac{2n+1}{n(n+1)} \{a_n \pi_n(\cos \theta) + b_n \tau_n(\cos \theta)\} \quad (2.1)$$

$$E_{\parallel} = -\frac{i}{kr} e^{-ikr+i\omega t} \cos \phi \sum_{n=1}^{\infty} \frac{2n+1}{n(n+1)} \{b_n \pi_n(\cos \theta) + a_n \tau_n(\cos \theta)\} \quad (2.2)$$

a_n and b_n are scattering coefficients depending on the relative refractive index $n_r = \frac{n_p}{n_m}$

and the particle size parameter $x = ka = \frac{2\pi n_m a}{\lambda}$, where λ is the wavelength in vacuum

and n_m is the refractive index of the medium. π_n and τ_n are angle-dependent functions¹.

For a medium containing N identical spherical particles per unit volume, the intensity scattered in a given direction is simply N times the intensities results form a single particle². At the same time, scattering by a single particle or collection of

identical particles does not decrease the degree of polarization of 100% polarized incident light¹.

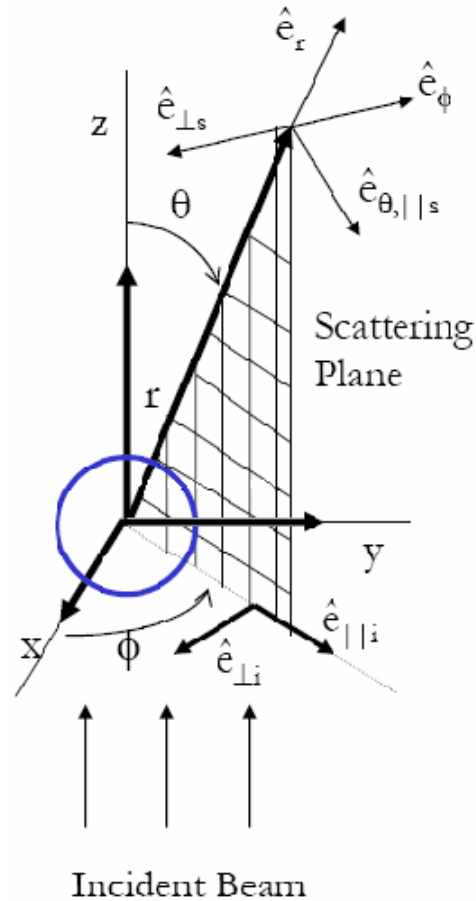


Figure 2-2: Scattering by an arbitrary sphere.

2.3. Extended GLMT for Coated Spheres

GLMT gives exact solutions for scattering of homogeneous spheres. However, for most biological cells, this is not sufficient. To model cells more accurately, GLMT can be extended. For spherical eukaryote cells, a coated sphere model could be used.

The mathematical form of all the scattering functions for a coated sphere have the same form as those for a homogeneous sphere, only the scattering coefficients a_n and b_n are different. For a coated sphere, two size parameters are defined, which are

$$x = ka = \frac{2\pi m_m a}{\lambda} \text{ and } y = kb = \frac{2\pi m_m b}{\lambda}. \text{ The boundary conditions at both the core-shell}$$

interface and the shell-medium interface need to be satisfied (Figure 2-3):

$$(\mathbf{E}_2 - \mathbf{E}_1) \times \hat{\mathbf{e}}_r = (\mathbf{H}_2 - \mathbf{H}_1) \times \hat{\mathbf{e}}_r = 0 \quad (2.3)$$

$$(\mathbf{E}_i + \mathbf{E}_s + \mathbf{E}_2) \times \hat{\mathbf{e}}_r = (\mathbf{H}_i + \mathbf{H}_s + \mathbf{H}_2) \times \hat{\mathbf{e}}_r = 0 \quad (2.4)$$

With a derivation similar to GLMT, the scattering coefficients can be solved.

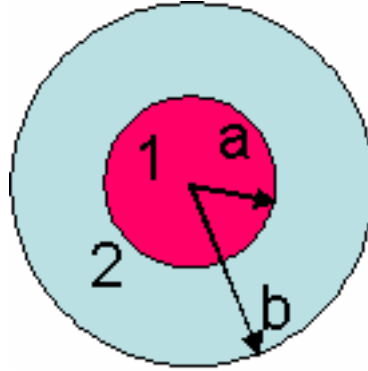


Figure 2-3: Core-shell model for extended GLMT. 1-core, 2-shell, a -radius of the core, b -radius of the entire coated sphere.

2.4. RM-I Method for Solid Spheroid

On the other hand, most non-spherical cells without significant internal organelles can be modeled with homogeneous spheroids. Two approaches to the problem of scattering by spheroids of arbitrary shape and composition are (1)

constructing separable solutions to the scalar wave equation in spheroidal coordinates and expanding the fields in vector spherical harmonics in a manner similar to that for spheres, and (2) using the T-matrix method.¹ Both are exact methods posing high computation complexity. Approximation methods such as Rayleigh-Debye (Rayleigh-Gans) and anomalous diffraction fails to provide results that are reliable enough for some purposes. In 1970s, Paul Latimer proposed several approximation methods for predicting scattering by spheroid that are more accurate and still of sufficient flexibility for most practical applications.⁴ One showing best agreement to the exact methods is the RM-I method, which uses the Rayleigh-Gans-Debye approximation to define an equivalent sphere and the exact Lorenz-Mie relations to determine the scattering by the equivalent sphere. As shown in Figure 2-4, when a spheroid defined by the equation $x^2 / (av)^2 + y^2 / a^2 + z^2 / a^2 = 1$ is placed at a certain orientation (γ, ψ) , for each scattering angle θ , an equivalent sphere of radius ag is defined according to the Rayleigh-Gans-Debye approximation, where g is a function of the spheroid's axial ratio v , orientation (γ, ψ) , and the scattering angle θ . The exact GLMT is then used to determine the scattering by the equivalent sphere. The scattering intensity of the spheroid is obtained by scaling the corresponding scattering phase function of the equivalent sphere by a factor of v^2 / g^6 .⁴⁻⁶

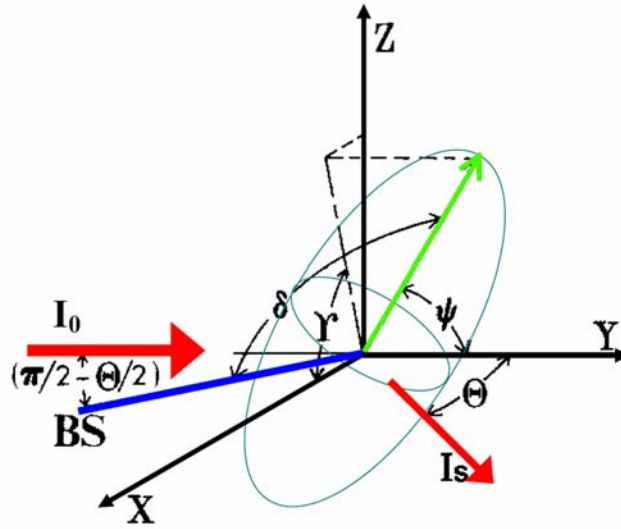


Figure 2-4: Schematic diagrams of RM-I, showing the modified laboratory coordinate system, the incident (I_0) and the scattered (I_s) beams, the orientation of the spheroid particle is determined by γ and ψ . Θ is the scattering angle, and δ is the angle of the spheroid orientation with respect to the bisectrix (BS).

In Figure 2-4, trigonometric relations give rise to:

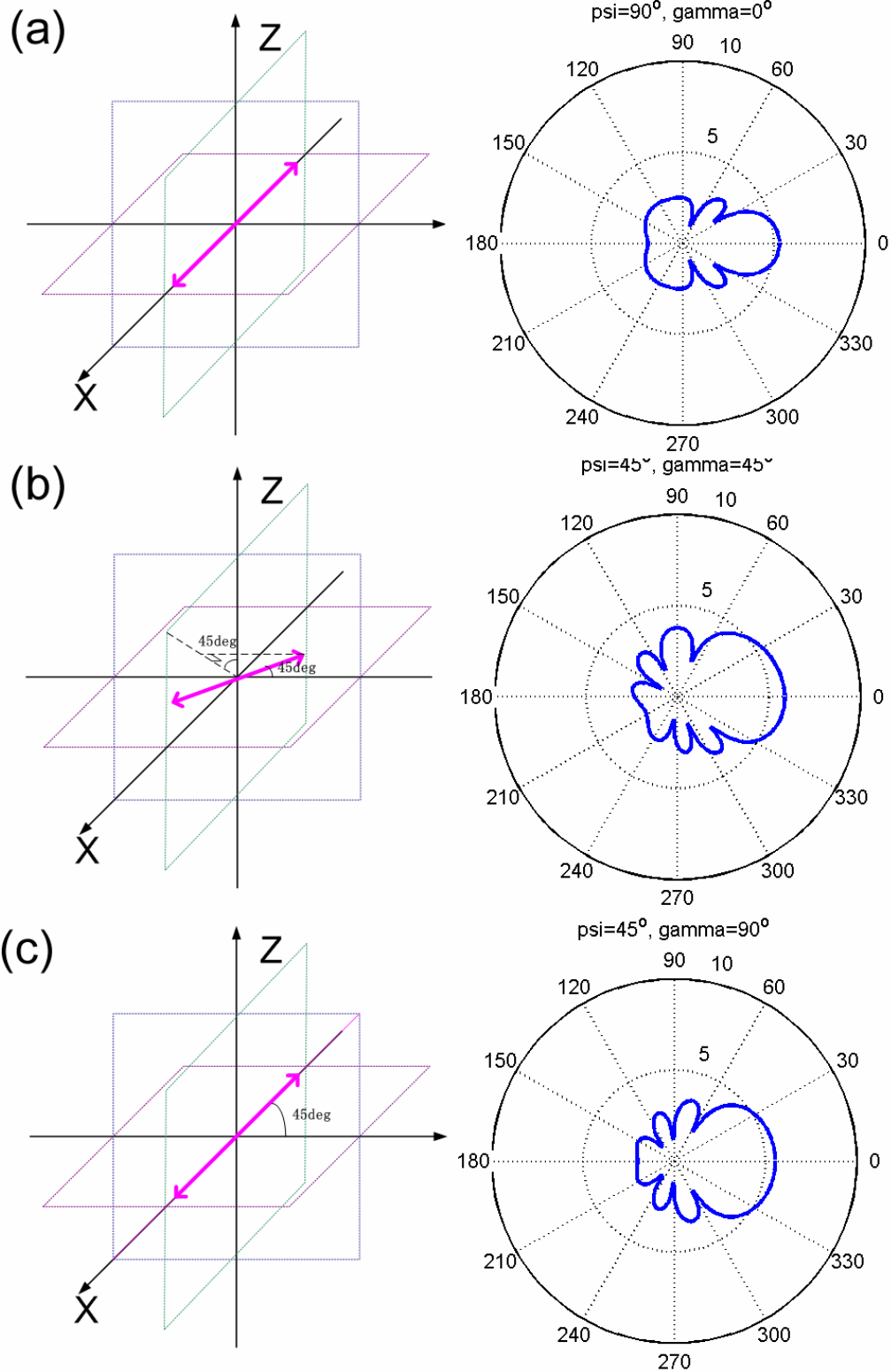
$$\delta = \pi - \arccos \left[\sqrt{(\sin \psi \cos \gamma)^2 + (\cos \psi)^2} \cdot \cos \left[\arctan(\tan \psi \cos \gamma) + \frac{\pi}{2} - \frac{\Theta}{2} \right] \right] \quad (2-5)$$

and g could therefore be calculated accordingly:

$$g = \left(\sin^2 \delta + v^2 \cos^2 \delta \right)^{\frac{1}{2}} \quad (2-6)$$

Figure 2-5 (a)-(g) shows the scattering diagrams calculated with RM-I approximation for a spheroid of $a=0.3\mu\text{m}$, $v=2$, $n_p=1.406$, $n_m=1.339$ at different orientations.

Figure 2-5 (a)-(g): The angular dependent scattering diagram of a spheroid with parameters of $a=0.3 \mu\text{m}$, $\nu=2$, $n_p=1.406$ in a medium of $n_m=1.339$ at different orientation (γ, ψ). Left: orientations of the spheroid, pink lines with arrows represent the long axis of the spheroid. Right: scattering diagrams in polar coordinate.



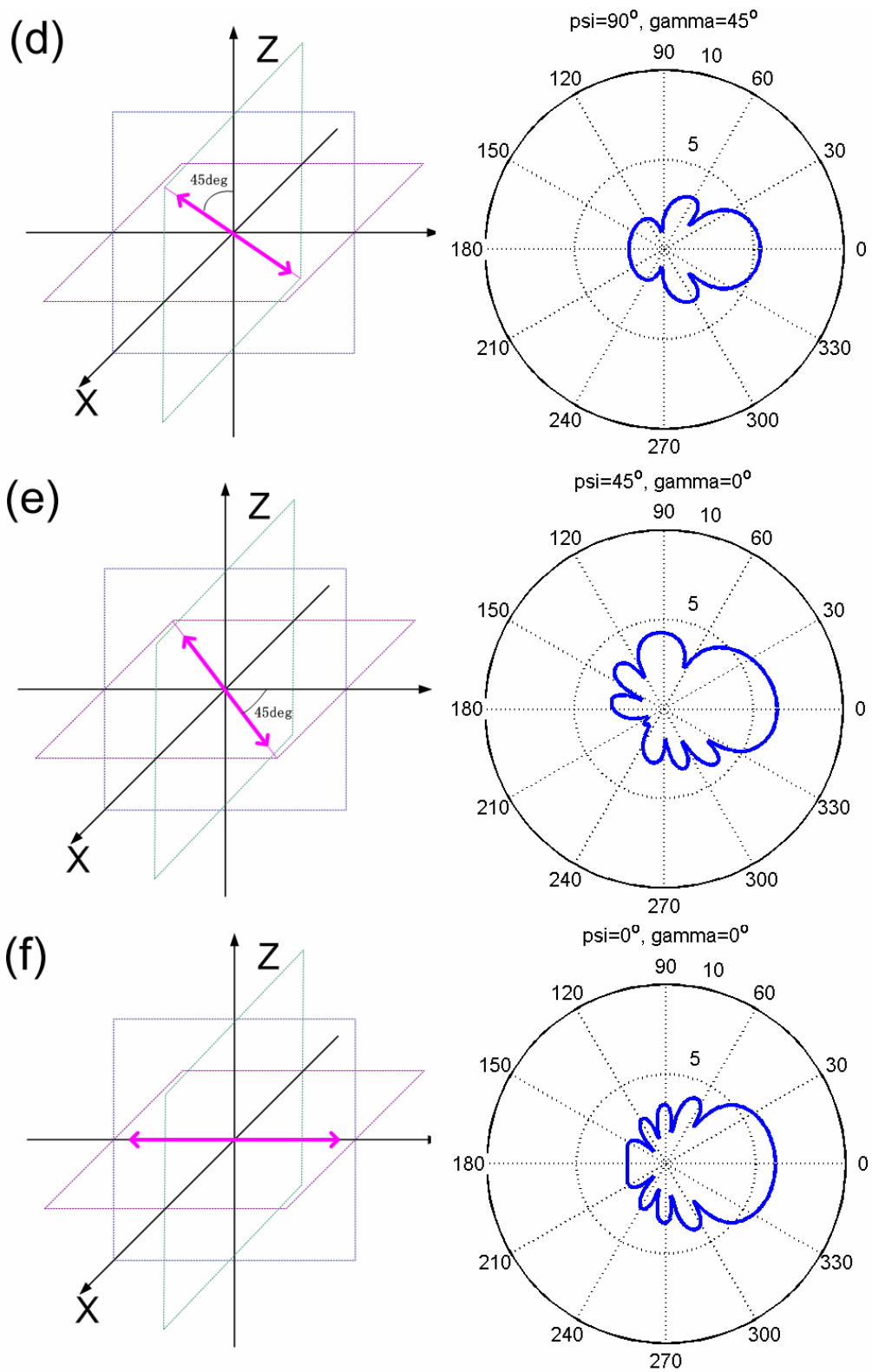


Figure 2-5 continued

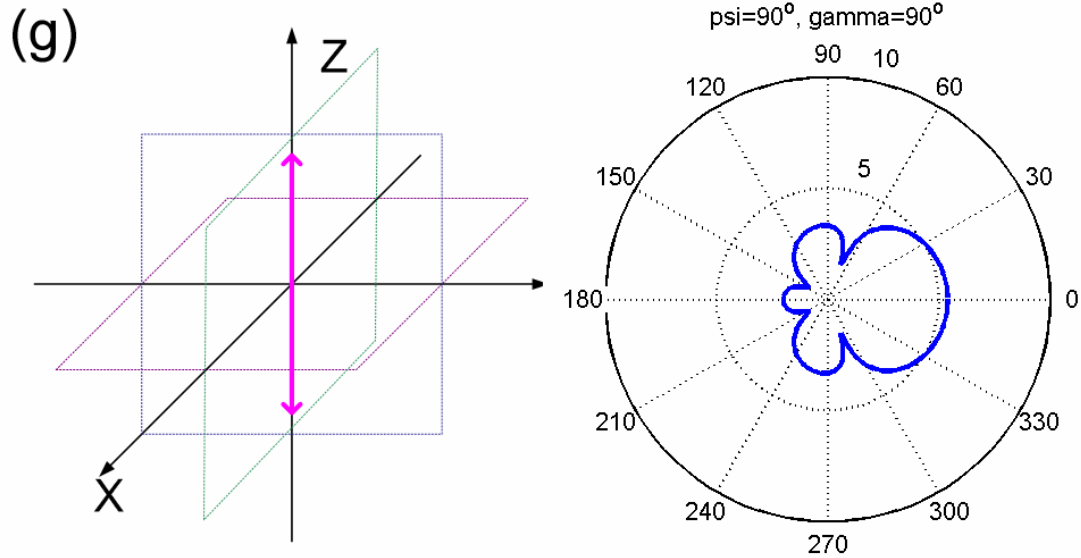


Figure 2-5 continued

When random orientation is assumed, γ and ψ are sampled in such a way that the increment of the solid angle Ω is isotropic on the geodesic dome. In the spherical coordinate,

$$d\Omega = \sin(\psi) \cdot d\psi \cdot d\gamma = d \cos(\psi) \cdot d\gamma \quad (2-7)$$

Therefore $\cos(\psi)$ is selected uniformly in $[-1,1)$, while γ equally is equally spaced in $[0^\circ, 180^\circ)$.

2.5. Introduction to Optical Trapping

In a beam of light, each photon has associated with it a momentum p that is a function of the wavelength λ and over a time period Δt exerts a force F_p described by:

$$p = \hbar k = h/\lambda = F_p \cdot \Delta t \quad (2-8)$$

where $k = 2\pi/\lambda$ is the wave vector and h is Planck's constant ($\hbar = h/(2\pi)$).

When photons are incident upon a dielectric particle there is a transfer of momentum that occurs through scattering. If the beam of light is focused down to a small area, the photons that scatter off of the dielectric particle in many different directions will exert a radiation pressure P_R that results in an optical force F_O . The axial optical force arises from the difference between total momentum carried by scattered light and the forward momentum of scattered light (Figure 2-6):

$$F_z = \frac{r^2}{c} \left[\int I(\theta) d\omega - \int I(\theta) \cos(\theta) d\omega \right] \quad (2-9)$$

where $d\omega = \sin(\theta) d\theta d\varphi$, $I(\theta)$ is the scattered intensity as a function of scattering angle θ , φ is the azimuth angle, and r is the distance from the detector to the particle.

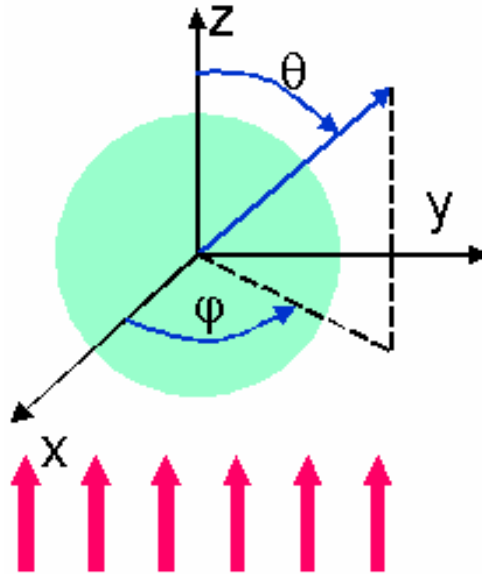


Figure 2-6: Definition of scattering angle θ and azimuthal angle φ .

Now that we have established the relationship between optical force and scattering, in order to provide an analytical description of how the optical force can be used to create an optical trap, one must first consider the size of the dielectric particle. Same as light scattering, the theory of optical trapping could also be divided into three size regimes, Rayleigh regime, intermediate regime and Mie regime.

2.5.1. Rayleigh Regime

For particles much smaller than wavelength (Rayleigh particles), trapping can be described as dipole-electric field interaction. Single dipoles under the presence a uniform electromagnetic beam of light were induced a dipole moment p_d :

$$p_d(r,t) = 4\pi \cdot n_m^2 \varepsilon_0 \frac{n_r^2 - 1}{n_r^2 + 2} a^3 E(r,t) \quad (2-10)$$

where n_m is the refractive index of the medium, $n_r = n_p/n_m$ is the relative refractive index of the particle to the medium, ε_0 is the permittivity of free space.⁷

The optical force on the dipole consists of two components, the gradient and scattering force. The scattering force F_s is determined by the scattering cross-section of the particle $\sigma\langle S \rangle$ and exerted in the direction of the incident power:⁷

$$F_s = n_m \frac{\sigma\langle S \rangle}{c} = \frac{8}{3} \pi \cdot k^4 \frac{n_m^5}{c} a^6 \left(\frac{m^2 - 1}{m^2 + 2} \right)^2 \cdot I \quad (2-11)$$

where I is intensity of the incident light, and c is the velocity of light in vacuum.

The second component of the optical force on the dielectric particle is the gradient force that arises from a Lorentz force on the dipole induced by the electromagnetic field and is given by:⁷

$$F_G = \frac{2\pi \cdot n_m a^3}{c} \left(\frac{m^2 - 1}{m^2 + 2} \right) \nabla I \quad (2-12)$$

As equation (2-11) and (2-12) state, scattering force is proportional to the intensity of the incident light while the gradient force is proportional to the intensity gradient of incident light (Figure 2-7). The necessary condition for a stable optical trap is a ratio of the optical gradient force and the optical scattering force greater than unity:

$$\frac{F_G}{F_S} \geq 1 \quad (2-13)$$

When this condition is met for a Gaussian beam with a focused spot size of ω_0 , the dielectric particle will be trapped at an axial position of $z = \pi\omega_0^2 / \sqrt{3}\lambda$.⁷

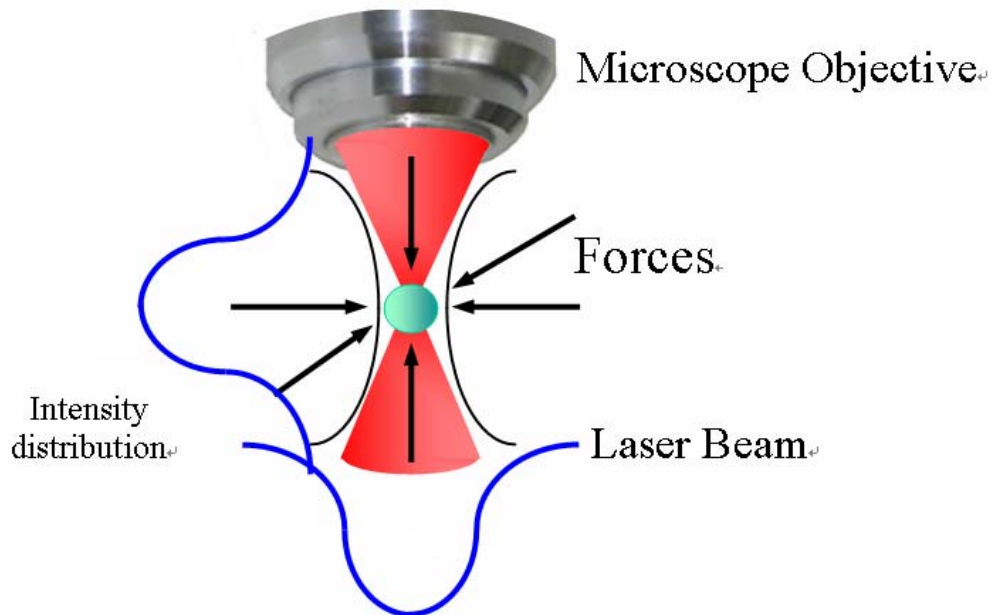


Figure 2-7: Three-dimensional optical trapping of a sphere.

Rayleigh regime analysis begins to break down as particle size grows.⁸ Larger particles enter the intermediate regime, where the most complex and rigorous types of analyses are necessary.

2.5.2. Intermediate Regime

The intermediate regime deals with particles that are both too small to fit in the Mie regime and too large to fit in the Rayleigh regime. Optical trapping in this regime has to be rigorously solved with exact electromagnetic analysis methods which require significant computation.⁹⁻¹³ Intermediate regime models provide accurate descriptions of optical trapping forces when the particle size is near 1 μm .

2.5.3. Mie Regime

For particles much larger than wavelength, ray optics is applicable, and trapping force is a result of photon momentum transfer at particle/medium boundaries due to reflection and refraction. In the ray optics approach, the total focused light beam is separated into individual rays, each with its own intensity, direction, and polarization. The scattering force is attributed to any reflection, refraction, or scattering component of the ray of light that points in an outward propagating direction, while the gradient force corresponds to the components of the light ray that produces a force on the particle toward the direction of maximum light intensity. Figure 2-8 displays a picture of two rays from a focused Gaussian beam entering a dielectric spherical particle that is offset from the optical beam axis in a transverse radial direction. For the ray labeled 'a' in this figure, the directions of the forces due to

refraction (F_D) and reflection (F_R) are shown using an arrow for the ray that is incident (i) on the front surface and outgoing (o) on the rear surface. Though not shown on this figure, because of the symmetry of the sphere, the force arrows from the ray labeled 'b' would be rotated counter-clockwise by 180 degrees for the force due to refraction and 90 degrees for the force due to reflection. Since the ray labeled 'a' is located at a point of higher intensity on the Gaussian envelope than the ray labeled 'b', a net restorative force ($|a| - |b|$) along the radial direction will act to center the spherical particle with the optical axis ($r = 0$). As the sphere moves closer to the center of the laser beam it bends the laser less, which results in a decreased force. When the sphere reaches the center of the laser beam it bends the laser beam symmetrically and the net force on the sphere becomes zero, i.e. the sphere has reached equilibrium at the center of the laser beam. In order to achieve a stable trap along the optical axis, the components of the force due to refraction F_D and reflection F_R along the (-z) direction must be larger than the components of the force due to refraction F_D and reflection F_R along the (+z) direction for each incident and outgoing ray that interacts with the dielectric sphere.

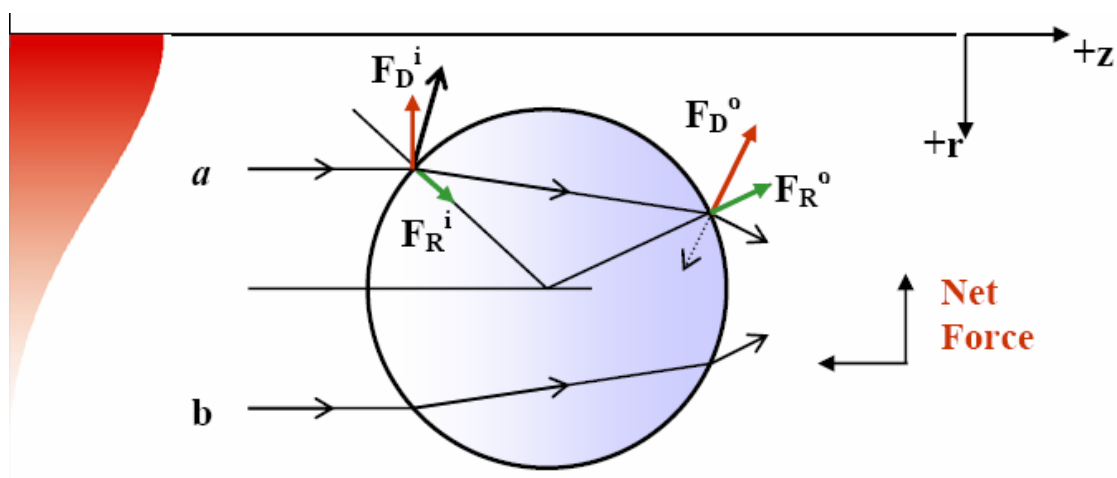


Figure 2-8: Diagram demonstrating the direction of the force due to refraction (F_D) and reflection (F_R) for two rays incident on a dielectric sphere that is offset from the optical axis.

This dissertation is primarily concerned with particles on the edge between the Mie regime and the intermediate regime.

2.6. Biomedical Application of Optical Traps

An optical trap can be easily incorporated into commercial microscopes commonly available in biological laboratories. Since its invention in 1986,¹⁴ the optical trap has been employed for the manipulation of yeast cells, blood cells, protozoa and various algae and plant cells,¹⁵ for trapping of viruses and bacteria,¹⁶ for measuring the compliance of bacterial flagella,¹⁷ for internal cell surgery,¹⁸ for manipulating chromosomes,¹⁹ for trapping and force measurements on sperm cells,²⁰ ²¹ for measuring the forces exerted by the motor molecules kinesin and dynein along microtubules,^{22, 23} and for cell sorting with optical recognition.²⁴ Biological and

medical applications of optical traps include probing the viscoelastic properties of single biopolymers such as DNA, probing cell membranes and aggregated protein fibers such as actin, and characterizing cells with different size and refractive indices.²⁵⁻²⁹

Optical traps proved to be an invaluable tool in exploring weak biological forces that were hitherto shrouded in mystery, and offer promise in manipulating and patterning cells, and even the components inside cells. Further efforts to expand and refine the capabilities of optical traps are therefore of significant worth to biomedical research.

2.7. Summary

This chapter gives a review on the theory of light scattering and optical trapping. The bridge between these two events is optical forces. A particle introduces discontinuity of refractive index in a medium, and deflects light at the interface. The momentum of light exerts a force on the particle that pulls it into and holds it in an equilibrium position. Optical traps are limited to the pico-Newton level, therefore only work on small particles, with radii from tens of micrometers down to individual atoms.

Models of both light scattering and optical traps break into three size regimes: the Mie regime (ray optics), the Rayleigh regime and the intermediate regime. The delineation is based upon particle size relative to optical wavelength. Mie particles have diameter much greater than the wavelength, Rayleigh particles have diameter much smaller than the wavelength, while intermediate particles cover the sizes in-between. Models for each size regime were discussed.

2.8. References

1. C. F. Bohren and D. R. Huffman, *Absorption and Scattering of Light by Small Particles* (John Wiley & Sons, New York, 1983).
2. H. C. V. d. Hulst, *Light Scattering by Small Particles* (John Wiley & Sons, Inc., New York, 1957).
3. Wikipedia, "Scattering" (2006), retrieved <http://en.wikipedia.org/wiki/Scattering>.
4. P. Latimer and P. Barber, "Scattering by ellipsoids of revolution a comparison of theoretical methods," *Journal of Colloid and Interface Science* **63**(2), 310-316 (1978).
5. P. Latimer, "Light scattering by ellipsoids," *Journal of Colloid and Interface Science* **53**(1), 102-109 (1975).
6. P. Latimer, A. Brunsting, B. E. Pyle, and C. Moore, "Effects of asphericity on single particle scattering," *Applied Optics* **17**(19), 3152-3158 (1978).
7. Y. Harada and T. Asakura, "Radiation forces on a dielectric sphere in the Rayleigh scattering regime," *Optics Communications* **124**(5-6), 529-541 (1996).
8. Y. Harada and T. Asakura, "Radiation forces on a dielectric sphere in the Rayleigh scattering regime," *Optics Communications* **124**(5-6), 529-541 (1996).
9. K. F. Ren, G. Grehan, and G. Gouesbet, "Prediction of reverse radiation pressure by generalized Lorenz-Mie theory," *Applied Optics* **35**(15), 2702-2710 (1996).
10. G. Gouesbet, B. Maheu, and G. Grehan, "Light scattering from a sphere arbitrarily located in a Gaussian beam, using a Bromwich formulation," *Journal of the Optical Society of America A-Optics & Image Science* **5**(9), 1427-1443 (1988).
11. K. Visscher and G. J. Brakenhoff, "Theoretical study of optically induced forces on spherical particles in a single beam trap. II. Mie scatterers," *Optik* **90**(2), 57-60 (1992).
12. J. S. Kim and S. S. Lee, "Scattering of laser beams and the optical potential well for a homogeneous sphere," *Journal of the Optical Society of America* **73**(3), 303-312 (1983).

13. D. A. White, "Vector finite element modeling of optical tweezers," *Computer Physics Communications* **128**(3), 558-564 (2000).
14. A. Ashkin, J. M. Dziedzic, J. E. Bjorkholm, and S. Chu, "Observation of a single-beam gradient force optical trap for dielectric particles," *Optics Letters* **11**(5), 288-290 (1986).
15. A. Ashkin, J. M. Dziedzic, and T. Yamane, "Optical trapping and manipulation of single cells using infrared laser beams," *Nature (London)* **330**(6150), 769-771 (1987).
16. A. Ashkin and J. M. Dziedzic, "Optical trapping and manipulation of viruses and bacteria," *Science* **235**(4795), 1517-1520 (1987).
17. S. M. Block, D. F. Blair, and H. C. Berg, "Compliance of bacterial flagella measured with optical tweezers," *Nature (London)* **338**(6215), 514-518 (1989).
18. A. Ashkin and J. M. Dziedzic, "Internal cell manipulation using infrared laser traps," *Proceedings of the National Academy of Sciences* **86**, 7914-7918 (1989).
19. M. W. Berns, W. H. Wright, B. J. Tromberg, G. A. Profeta, J. J. Andrews, and R. J. Walter, "Use of a Laser-Induced Optical Force Trap to Study Chromosome Movement on the Mitotic Spindle
10.1073/pnas.86.12.4539," *PNAS* **86**(12), 4539-4543 (1989).
20. W. H. W. Y. Tadir, O. Vafa, T. Ord, R. H. Asch, M. W. Berns, "Micromanipulation of sperm by laser generated optical trap," *Fertil. Steril.* **52**, 870-873 (1989).
21. W. H. W. Y. Tadir, O. Vafa, T. Ord, R. H. Asch, M. W. Berns, "Force generated by human sperm correlated to velocity and determined using a laser generated optical trap," *Fertil. Steril.* **53**, 944-947 (1990).
22. A. Ashkin, K. Schutze, J. M. Dziedzic, U. Euteneuer, and M. Schliwa, "Force generation of organelle transport measured in vivo by an infrared laser trap," *Nature (London)* **348**(6299), 346-348 (1990).
23. S. M. Block, L. S. Goldstein, and B. J. Schnapp, "Bead movement by single kinesin molecules studied with optical tweezers," *Nature (London)* **348**(6299), 348-352 (1990).
24. T. N. Buican, M. J. Smyth, H. A. Crissman, G. C. Salzman, C. C. Stewart, and J. C. Martin, "Automated single-cell manipulation and sorting by light trapping," *Applied Optics* **26**(24), 5311-5316 (1987).

25. A. Ashkin, "History of optical trapping and manipulation of small-neutral particle, atoms, and molecules," *IEEE Journal of Selected Topics in Quantum Electronics* **6**(6), 841-856 (2000).
26. K. Svoboda, P. P. Mitra, and S. M. Block, "Fluctuation analysis of motor protein movement and single enzyme-kinetics," *Proceedings of the National Academy of Sciences* **91**, 11782-11786 (1994).
27. C. Bustamante, Z. Bryant, and S. B. Smith, "Ten years of tension: single-molecule DNA mechanics," *Nature (London)* **421**(6921), 423-427 (2003).
28. R. A. Flynn, B. Shao, M. Chachisvilis, M. Ozkan, and S. C. Esener, "Two-beam Optical Traps: Refractive Index and Size Measurements of Microscale Objects," *Biomedical Microdevices* **7**(2), 93-97 (2005).
29. R. A. Flynn, B. Shao, M. Chachisvilis, M. Ozkan, and S. C. Esener, "Counter-propagating optical trapping system for size and refractive index measurement of microparticles," *Biosensors and Bioelectronics* **21**(7), 1029-1036 (2006).

3. Angularly Dependent Light Scattering for Marine Microbe Characterization

In this chapter we demonstrate the use of angularly dependent light scattering from random-oriented suspension for characterizing marine picoplankton which are around 1 micron in size. The intensity of the scattered light is collected over an angular range of $0.5\text{-}179.5^\circ$ with a resolution of 0.5° using an optical setup based on an elliptical mirror, a rotating aperture and a photomultiplier (PMT). The system is calibrated with liposomes extracted from 30 nm membrane which have a nearly constant scattering distribution for vertically polarized light (azimuthal angle= 90°). The cells are modeled as prolate spheroids with dimensions independently measured via standard microscopy. Prokaryotes are approximated as homogeneous spheroids and simulated using the hybrid of the Generalized Lorentz-Mie Theory and Rayleigh-Debye method (RM-I). On the other hand, an extended RM-I method is developed for the simulation of coated spheroid with different shell thickness distributions and picoeukaryote cells are modeled as a coated spheroid with a spherical core. Good overall agreements were obtained between theoretical predictions and experimental measurements. To be specific, the signal to noise ratio of the scattering pattern in the middle angular range ($40\text{-}140^\circ$) is high enough to allow for cell characterization. The distinctive scattering patterns of different species can potentially serve as finger print information for marine microbe identification.

The main contributions of the research addressed in this chapter include the modeling of non-spherical eukaryote cells with a coated spheroid, and the development of a new approximation algorithm with high accuracy and low computation complexity --- the Extended RM-I method for coated spheroid with different core shape and shell thickness distributions, and the Matlab simulations for scattering diagram from microparticles (beads, cells, vesicles, etc.) with various morphologies

3.1. Introduction on Light Scattering Measurement of Biological Cells

When a cell is illuminated, it scatters light in all directions. The spatial distribution of the scattered light intensity is not random, but a complex spatial pattern that is dependent on a cell's size, shape, refraction index, density, and morphology. Because of the emission coherence from the different scattering centers in a cell, elastic light scattering may offer more information on the morphology of the cell compared to incoherent techniques such as, e.g., fluorescence spectroscopy; this is especially true when a label-free approach is sought. Studying the scattered light in appropriate angular ranges enables the determination of morphological information from the cell which can be used to discriminate between different cell types, and more importantly between different cell states. Among many important applications in biomedical science for cell analysis and sorting,^{1, 2} a large body of work uses flow cytometry systems that detect forward and side-scattered light, primarily for cell size detection. More complex biological applications such as label-free detection of small,

drug-induced morphological changes inside the cell, have been limited, some of these limitations being due to the experimental difficulties in measuring of the angular distribution of the scattered light intensity, which typically spans 5-8 orders of magnitude. There have been only a few attempts to detect the full 180° or 360° phase function from single biological cells,³⁻⁷ however, they either used discrete angles with relatively low angular resolution, or the measured cells were in the size range of larger than $5 \mu\text{m}$.

There have been numerous studies that suggest how the nature of a cell affects the angular intensity distribution in the scattering phase function. Forward scattered light in the small angle region ($\theta \lesssim 2^\circ$ where $\theta = 0^\circ$ corresponds to the direction of incident light) is primarily dependent on the cell's size and refractive index,⁸ however, other factors such as cell shape and morphology contribute as well.⁹ Forward scattered light at larger angles (5° - 30°) has been suggested to be largely dependent on the nucleus/whole cell volume ratio of a cell. Experiments on suspensions of isolated nuclei have yielded similar results to whole cell scattering in this angular region, implying minimal dependence on the cell's smaller internal structures.⁹⁻¹¹ On the other hand, light scattered at larger angles ($\sim 50^\circ$ - 130°) is highly dependent on the amount of a cell's internal structure.^{9, 12, 13} Organelles such as the mitochondria, peroxisomes, lysosomes, microtubules, etc. serve as scattering sites amid the relatively isotropic refractive index medium of the cytoplasm, contributing to light scattering at large scattering angles.¹⁴⁻¹⁸ As an example, the high spatial frequency of refractive index variations of a granulocyte cell causes higher intensity of light scattering at these large

angles than does the relatively more isotropic index of a lymphocyte cell. This presents an extremely useful means to discriminate between cells that appear to be similar, yet have different internal structures. Experiments on suspensions of isolated proteins and mitochondria, as well as FDTD (Finite Difference Time Domain) models including small internal structures, have validated the claim that cell organelles are primarily responsible for the amount of large angle scattering.¹⁵ Lastly, cell membrane is mainly responsible for the scattered light in the backscatter region ($160^\circ < \theta < 180^\circ$).¹⁹ A cell with a damaged membrane scatters much less light in the backward direction than a healthy cell. This property could be used to discriminate dead cells from live ones.

3.2. Background and Motivation of Marine Picoplankton Characterization

With progressively global warming and growing sea pollution and exploitation, it has become increasingly important to monitor and understand marine microbes,²⁰ which are not only the key players in the marine food web, fix over 70% of nitrogen and carbon in the oceans,²¹ but also responsible for over half of the global primary productivity²² and over 50% of the atmosphere oxygen supply.²³ In the big family of microbes, picoplankton with diameter smaller than 2 μm are least understood, nevertheless most important for organic productivity. Their small sizes ensure very high sunlight capture and nutrient taking up efficiency due to the large surface area to internal volume ratio.

The cells of which picoplankton consist are of two main types: prokaryotic cells (cells with no nucleus) and eukaryotic cells (cells with a nucleus). Prokaryotic cells are represented by the small unicellular cyanobacteria, *Synechococcus*²⁴ and *Prochlorococcus*,²⁵ which are the most abundant and smallest photosynthetic microorganisms in the world's oceans, and are responsible for an estimated 20–40% of chlorophyll biomass and carbon fixation in the oceans.²⁶ Another major group of prokaryote is heterotrophic bacteria which generally dominates the picoplankton fraction in terms of cell number and biomass.²⁷ As the smallest free living eukaryotes on the earth, picoeukaryotes are numerically less abundant. In part because of their lower abundance, as well as their complexity and diversity as a group, they have been less well studied than the marine cyanobacteria. New classes of the former are still being discovered.

An important problem in oceanic microbial ecology is the characterization of the constituents of the sea, especially the distribution of these picoplankton in different parts of the open ocean and at different times. Towards this goal, the availability of a rapid, simple, and inexpensive way to classify ocean picoplankton would be of great use.

Currently, the most popular optical technique for identifying marine microbes is flow cytometry, which detects the forward and side-scattered light and fluorescence signal from cells. Using this technology, subgroups within the autotrophic picoplankton fraction (*Synechococcus*, *Prochlorococcus*, and picoeukaryote) have been identified by differences in the fluorescence properties of their photosynthetic

pigments,²⁷ which requests blue or UV excitation that induces cell damage. What is more, absence of pigments in heterotrophic picobacteria rendered them more difficult to classify. As one solution, bacterial DNA can be stained with fluorescence dyes.²⁷


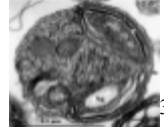

Scattering measurement of either microbes or the bulk properties of seawater have been undertaken by other researchers. Such systems have typically relied on either a finite set of PMTs²⁸ or the use of a pivoting transmitter and detector.²⁹ A more recent design³⁰ uses a rotating periscopic prism which allows measurement of the Volume Scattering Function from 0.6^\pm to 177.3^\pm with an angular resolution of 0.3^\pm . Here, a complete measurement takes at least 1.5 minutes. Besides free space optics, a wide-angle, semi-circular array of 175 optical fibers and a scanning disk were used for fast collection of multi-angle scattering to a single PMT,³¹ which allows scattering measurement from 3^\pm to 177^\pm with 1^\pm angular resolution and 1 set of measurement in as short as 10 ms.

The work presented in this chapter shows that the label-free, non-invasive elastic scattering measurements on low-concentration cell suspensions could also be used for differentiation subgroups in picoplankton, which has very similar sizes and shapes. With the scattering signature of these picoplankton available, the final goal is to design an instrument for *in situ* measurement.

The scattering diagrams of three representative species within the picoplankton (Table 3-1), one type of cyanobacteria --- *Synechococcus sp.* strain CC9311, one type of picoeukaryote --- *Ostreococcus sp.* strain CCE9901 and one type of picobacteria --- *Flavobacterium sp.* strain ALC1 are measured in the angular range of $0-180^\circ$. All

three species have two dimensions not larger than $1 \mu\text{m}$, one dimension of about 2-3 μm , and resemble ellipsoids in shapes.

Table 3-1: Three types of marine picoplankton to be studied, their scientific names, microscopy images, brief descriptions, and corresponding models for simulation.

Picoplankton Genus	Picture	Description	Model ($n_m = n_{\text{seawater}} = 1.339$)
<i>Synechococcus</i> sp. CC9311 (cyanobacteria)	 32	One of the most abundant, smallest photosynthetic organisms	Homogeneous spheroid $0.8\mu\text{m} \times 0.8\mu\text{m} \times 2.0 \mu\text{m}$ $n_p = n_{\text{cell}} = 1.4060$. ³³
<i>Ostreococcus</i> sp. CCE9901 (picoeukaryote)	 34	Smallest eukaryotic cells, no cell wall	Coated spheroid with a concentric spherical core $1.0\mu\text{m} \times 1.0\mu\text{m} \times 2.0 \mu\text{m}$ $n_1 = n_{\text{cytoplasm}} = 1.37$. ³⁵ $n_2 = n_{\text{nucleus}} = 1.40$. ³⁵
<i>Flavobacterium</i> sp. ALC1 (picobacteria)	 36	Small rods	Homogeneous spheroid $1.0\mu\text{m} \times 1.0\mu\text{m} \times 3.5 \mu\text{m}$ $n_p = n_{\text{cell}} = 1.4060$. ³³

3.3. Theoretical Modeling of Scattering from Microbes Based on RM-I and Its Extension

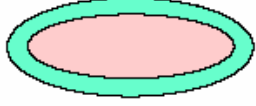
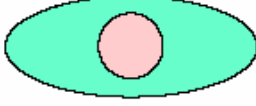
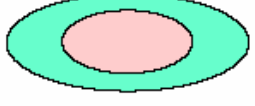
As introduced in section 2.2, Generalized Lorentz-Mie Theory (GLMT) provides a rigorous solution for light scattering by an isotropic sphere of arbitrary size in a homogeneous medium. However, for most biological cells, this is not sufficient. For eukaryote cells with a nearly spherical shape, the extended GLMT for coated spheres discussed in section 2.3 is more appropriate. On the other hand, most non-

spherical cells can be approximated with spheroids. Among various approaches that can predict the scattering cross-section of a spheroid, one approximation showing best accuracy yet not cumbersome in computation is the RM-I based on a hybrid of the Rayleigh- Gans-Debye approximation and the exact GLMT for sphere (section 2.4).

According to microscopy observations, an average, non-dividing cell of *Synechococcus sp.* strain CC9311 has a spheroid shape with outer dimensions of around $0.8\mu\text{m} \times 0.8\mu\text{m} \times 2.0\mu\text{m}$; whereas a $1.0\mu\text{m} \times 1.0\mu\text{m} \times 3.5\mu\text{m}$ spheroid could be used to approximate a cell of *Flavobacterium sp.* strain ALC1. Despite the internal structure of these prokaryote cells, they are all modeled as homogeneous spheroids with an index of refraction $n_p=1.406$,³³ whereas the refractive index of sea water is $n_m=1.339$.

However, most eukaryote cells are not necessary spherical. For the eukaryote cell of *Ostreococcus sp.* strain CCE9901, both the homogeneous spheroid and the coated sphere turn out to be approximations not accurate enough. Scattering from non-homogeneous spheroids have mostly been simulated with exact numerical approaches that require high computation volume. Here, we developed a new approximation based on the RM-I method (section 2.4). By replacing the GLMT for solid spheres with the extended GLMT for coated sphere, the RM-I could be extended to simulate the scattering from a coated spheroid with a concentric core. The shape of the core is flexible, which could be a spheroid, a sphere or anything that could be represented by a mathematical function. This provides a way to better model the scattering from eukaryote cells with a simple approximation. Table 3-2 shows three typical models, and the corresponding definition of the equivalent coated sphere.

Table 3-2: Extended RM-I for coated spheroids with three typical core geometries

	Uniform Thickness	Spherical Core	Spheroidal Core
Model Scheme			
Equation of the outer spheroid	$\frac{x^2}{(av)^2} + \frac{y^2}{a^2} + \frac{z^2}{a^2} = 1$	$\frac{x^2}{(av)^2} + \frac{y^2}{a^2} + \frac{z^2}{a^2} = 1$	$\frac{x^2}{(av)^2} + \frac{y^2}{a^2} + \frac{z^2}{a^2} = 1$
Equation of the core	$\frac{x^2}{(av-t)^2} + \frac{y^2}{(a-t)^2} + \frac{z^2}{(a-t)^2} = 1$	$x^2 + y^2 + z^2 = r^2$	$\frac{x^2}{(a_1v_1)^2} + \frac{y^2}{(a_1)^2} + \frac{z^2}{(a_1)^2} = 1$
Size parameters of the equivalent coated sphere	$x = 2\pi n_m (a \cdot g - t) / \lambda_0$ $y = 2\pi n_m (a \cdot g) / \lambda_0$ $t = \text{constant}$	$x = 2\pi n_m r / \lambda_0$ $y = 2\pi n_m (a \cdot g) / \lambda_0$	$y = 2\pi n_m (a_1 \cdot g_1) / \lambda_0$ $y = 2\pi n_m (a \cdot g) / \lambda_0$

As shown in Table 3-2, analogous to RM-I for homogeneous spheroid, at each (γ, ψ, θ) , an equivalent coated sphere is defined. Because the outer radius is still $a\check{g}$ for the equivalent coated sphere, the inner radius could be expressed as $a\check{g}-t(\gamma, \psi, \theta)$ for different thickness distribution $t(\gamma, \psi, \theta)$. If $t(\gamma, \psi, \theta)$ is constant, the coated spheroid has a uniformly thick shell, while for $a\check{g}-t(\gamma, \psi, \theta)=r=\text{constant}$, the core is a sphere whose radius equals to r . The scattering from the equivalent coated sphere could then be obtained using the extended GLMT for coated spheres.³⁵ As a result, the scattering from a coated spheroid could be calculated by scaling the scattering from the equivalent coated sphere at each (γ, ψ, θ) . The scaling factor is the same with that from the homogeneous spheroid, which is v^2 / g^6 (section 2.4).

Microscopy observation shows that the cell of *Ostreococcus sp.* strain CCE9901 is ellipsoid, while the nucleus is relatively round. Accordingly, the cell of *Ostreococcus sp.* strain CCE9901 is approximated by a spheroid of $1.0\mu\text{m} \times 1.0\mu\text{m} \times 2.0\mu\text{m}$ with a concentric spherical core of radius $0.25\mu\text{m}$. The refractive index is 1.37 for cytoplasm and 1.40 for nucleus.³⁵

3.4. Experimental Setup

The experimental setup is shown in Figure 3-1. Based on an elliptical mirror³⁸,³⁹, the system is designed to record 360° light scattering. A cylindrical, polished glass cuvette (outer diameter of 10 mm, height 16 mm, Hellma Cells, Inc., Plainview, NY) is held at the focal point of the ellipsoidal reflector, the orientation of the cuvette inside the elliptical mirror was such that the scattering laser enters and exits normal to the cuvette surface. The beam of a red laser (40 mW, 658 nm, Crystal Laser, Reno, NV) incident horizontally to the cuvette gets scattered by particles inside and reflected by the elliptical mirror toward its second focal point where the PMT (R3896, Hamamatsu, Bridgewater, NJ) is located. A rotating aperture is used, whose height and radial position determines the azimuthal angle at which the scattered light is detected, which is 0° in our case. The direction of scattered light to be detected is selected by the position of the rotating aperture. For spherical symmetrical particles and particles with random orientation, only 0 - 180° detected is necessary. It is not possible to detect light scattered at very small angles and in the vicinity of 180° due to the finite divergence of the excitation laser beam. In our experiments, light scattering

is recorded in the range of $0.5\text{-}179.5^\circ$. The significant contribution from internal reflections inside the cylindrical cuvette limits the accuracy of our data for weakly scattering (small particles) in the angular range of $0\text{-}40^\circ$ and $140\text{-}180^\circ$. Due to the large dynamic range of the scattered light, a circularly graded intensity filter is placed after the rotating aperture such that the back-scattered light is attenuated the least whereas forward-scattered light is attenuated the most. An interference filter (646-666nm) and a condensing lens are placed before the PMT to increase the SNR of the measurement.

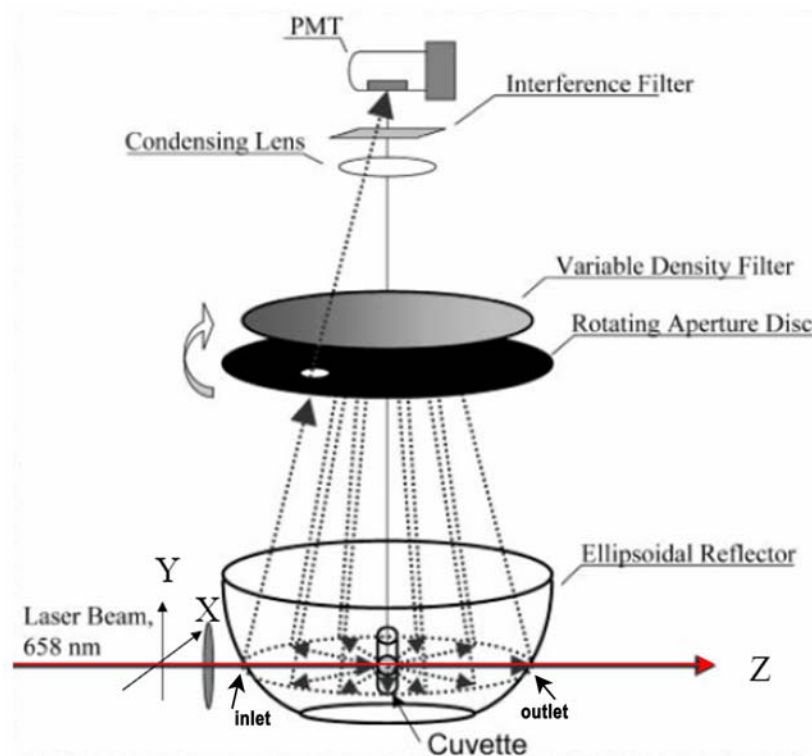


Figure 3-1: Schematics of optical setup used to record scattering diagrams from particles suspended in the cuvette.

The excitation beam is linearly polarized and focused into the center of the cuvette to induce scattering. The intensity variation of the red laser is $<0.5\%$. The diameter of the laser beam is 0.9 mm, the beam diameter in the center of the cuvette is 116 μm for focusing lens with 125 μm focal length, because it is much larger than the particles to be measured, a uniform beam profile can be assumed. The data acquisition system enables PMT sampling frequencies of up to 200 kHz and the rotation velocity of the aperture can be varied from 60 RPM to 2000 RPM, corresponding to a maximum time resolution of 30 ms (defined as the time interval between the start of one measurement and the start of the next one). The upper limit of the angular resolution is determined by the aperture size, while the actual angular step is determined by sampling frequency and rotation velocity. The azimuthal angle α is defined as the angle between the laser polarization and the detection plane, which is 0° for horizontal polarization (*p*-polarization), and 90° for vertical polarization (*s*-polarization). The diameter of the rotating aperture was 1 mm, yielding an angular resolution of 0.36° (distance between the center of the cuvette and the rotating aperture was 163 mm). The complete apparatus is put in a dark environment to minimize any source of background noise during experiments.

3.5. Sample Preparation

3.5.1. Marine Microbes

Isolates of *Synechococcus sp.* strain CC9311, and *Ostreococcus sp.* strain CCE9901 were grown in standard media (SN, F/4 media, respectively) at 20-22°C and

constant light conditions ($28 \mu\text{mol quanta m}^{-2}\text{s}^{-1}$). The isolate of *Flavobacterium sp.* strain ALC1 were collected at Scripps pier ($32\pm 53'$ N, $117\pm 5'$ W), followed by plating in Zobell agar, and then grown in Zobell medium (seawater with 5 g peptone and 0.5 g yeast extract per liter, autoclaved) at $25\pm 1^\circ\text{C}$ in a shaker for two days after inoculation.

Seawater for filtration (to be used for dilution) was collected from the top of the sea surface, gravity filtered through a 0.2- μm sterile acid-rinsed Gelman Supor filter capsule, and distributed to acid-cleaned 1-liter polycarbonate bottles.

3.5.2. Liposome

0.2 mL DOPC chloroform solution was put into a small beaker, and dried with nitrogen gun in a fume hood. After overnight evaporation in a vacuum desiccator, the lipid film was rehydrated with 1 ml PBS (Phosphate Buffered Saline) 1μ solution, and agitated for full mixing. 30 minutes later, the hydrated lipid suspension was pored into a round bottom tube, and subjected to 3-5 freeze/thaw cycles by being alternately placed in a dry ice-acetone bath and warm water bath. This is to increase the efficiency of entrapment of water-soluble compounds. At the same time, the mini-extruder (Avanti polar lipids, Inc., Alabaster, AL) was assembled with prewetted membrane supports. The extruder was then prewetted by passing a full syringe of buffer (PBS 1μ solution) through the membrane. Once fully hydrated, the sample was loaded into one of the gas-tight syringes and carefully placed into one end of the mini-extruder. After placing an empty gas-tight syringe into the other end of the mini-extruder, the plunger of the filled syringe was pushed gently until the lipid solution was completely transferred to the alternate syringe. After repeating pushing back and

forth for more than 4 times (total of 10 passes through membrane), the final extrusion filled the alternate syringe so that the chances of contamination with larger particles or foreign materials were reduced. Finally, the lipid solution was removed from the filled syringe and injected into a clean sample vial.

During extrusion, the environmental temperature should be kept above the lipid phase transition temperature. Because DOPC has a transition temperature of $-20\pm\text{C}$, it is not necessary to heat the extruder. For liposome with 30 nm nominal diameter, the extrusion procedure is performed twice, first with a 100 nm membrane, then a 30 nm membrane.

The vesicle preparation was stored at $4\pm\text{C}$ for less than 3-4 days before experiments.

3.6. System Calibration and Validation

Before experimenting with microbes, system calibration is necessary so that any intrinsic intensity modulation would be taken into consideration. Liposome, to be more specific, Large Uni-lamellar Vesicles prepared by Extrusion Techniques (LUVET)⁴⁰ was chosen as the tool for calibration. As vesicles formed with lipid bilayer, liposome assembles cell membrane in chemistry, and its size and refractive index could be easily adjusted. Small liposomes with tens of nanometer diameter yields very flat scattering curve for the vertical polarization that can be used for system calibration. The lipid used was DOPC (1, 2-Dioleoyl-*sn*-Glycero-3-Phosphocholine).

Small liposomes can be regarded as a dipole in a uniform light field. According to electromagnetic theory, the scattered field is constant for vertical polarization ($\alpha=90^\circ$), and is a cosine function of the scattering angle for horizontal polarization ($\alpha=0^\circ$). As a result, a small liposome yields a very flat scattering curve for vertical polarization that can be used for system calibration (Figure 3-2(a)). For comparison, Figure 3-2 (b)-(d) list simulated scattering diagram from liposomes with larger diameters, 200 nm, 250 nm, and 400 nm, respectively. The extended GLMT for coated sphere is used for simulation (Figure 3-3), parameters are consistent with those in the real case, i.e. PBS (Phosphate Buffered Saline) 1 μ solution is used as both the inclusion and the surrounding buffer, refractive index is $n_m=1.33$. For liposomes, $n_p=1.46$, and the thickness of lipid bilayer is 5nm. As the liposome becomes larger, it can no longer be regarded as a single dipole, and the scattering curves get complicated.

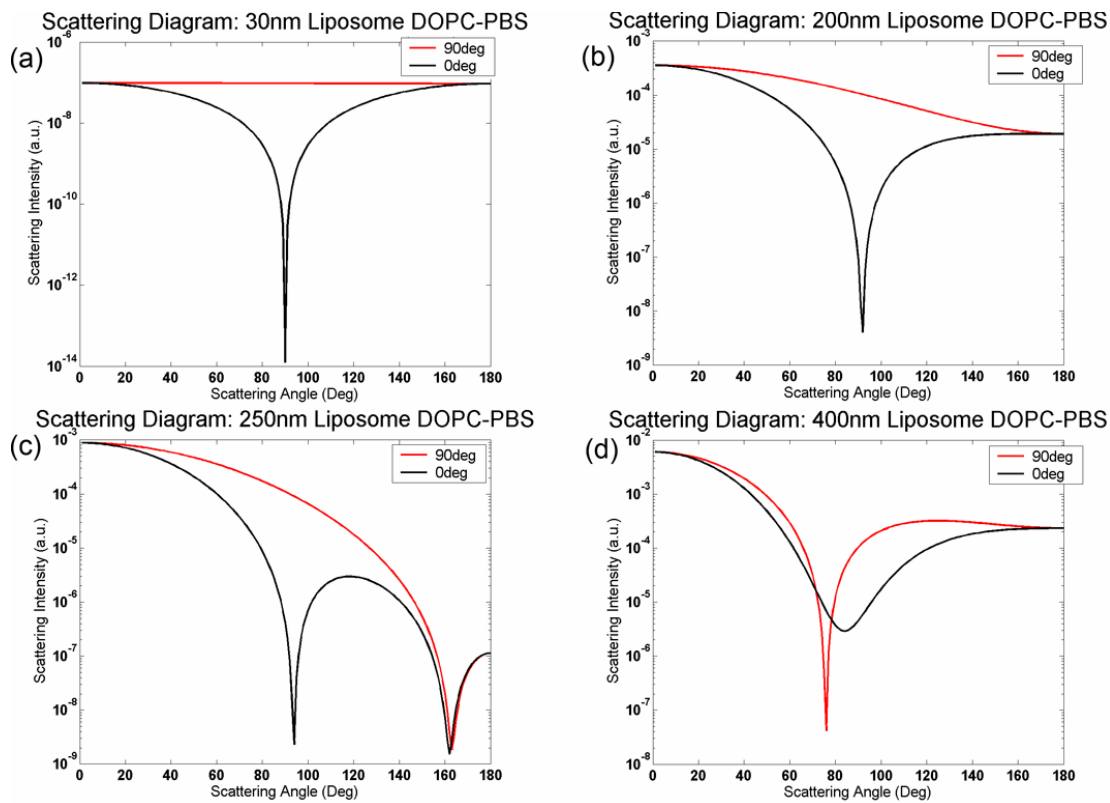


Figure 3-2: Simulated scattering diagram from liposome with diameters of (a) 30 nm, (b) 200 nm, (c) 250 nm, and (d) 400 nm. All the four simulations use the coated sphere model as presented in Figure 3-3.

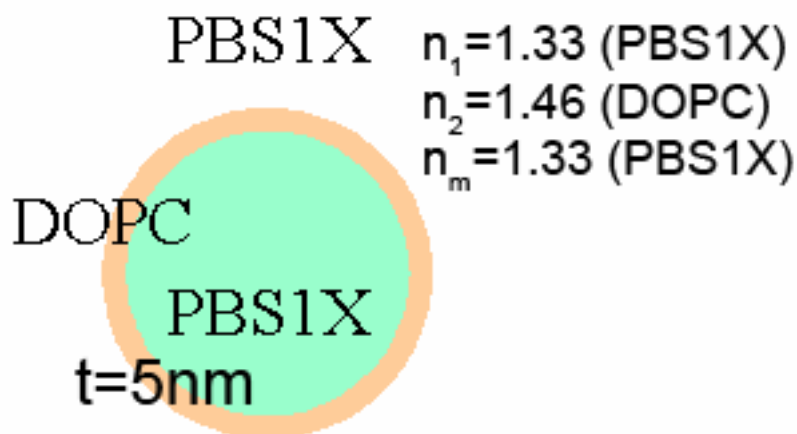


Figure 3-3: Coated sphere model for liposome scattering simulation, t ---the thickness of the lipid bilayer.

In practice, the size of the extruded liposome obeys log normal distribution³⁵ instead of being uniform. Extended GLMT for coated spheres with size polydispersity is used to simulate the angularly resolved scattering from 30nm liposome suspension in PBS (Phosphate Buffered Saline) 1 μ solution (Figure 3-4(a)). Experimental curves measured from low-concentration (~ 1 particle per scattering volume defined, where the scattering volume is calculated as $V=\pi\omega_0^2\mathcal{V}_i$, $\omega_0=58\ \mu\text{m}$ is the beam waist at the center of the cuvette, and $D_i=8\ \text{mm}$ is the inner diameter of the cuvette) suspensions agree with the theoretical results, especially in the 40-140 \pm range where the scattering curve for $\alpha=90\pm$ is considerably flat. The ratio between the experimental $\alpha=90\pm$ data (the red curve in Figure 3-4(b)) and the theoretical $\alpha=90\pm$ data (the red curve in Figure 3-4(a)) is then used for calibrating experimental data on microspheres and microbes.

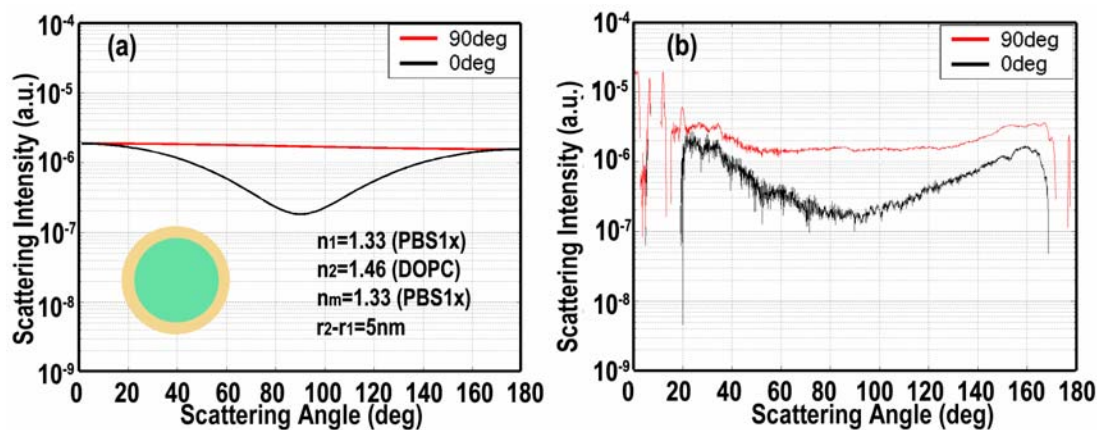


Figure 3-4: Scattering diagram of the log-normal-diameter-polydispersed liposome suspension with 30 nm nominal diameter in PBS1x solution. (a) Simulation based on extended GLMT of coated sphere. (b) Experimental curve

After calibration, scattering measurements on polystyrene microspheres with diameters of 0.6 μm , 0.8 μm and 1.0 μm (PPS06, PPS08 and PPS10, Kisker, Germany) are performed in deionized water to validate the experimental apparatus. The experimental data (Figure 3-5(b)) matches GLMT simulation (Figure 3-5(a)) very well between 40° and 140°. This proves the system's ability to distinguish micron and submicron-sized particles. The deviations at small and large angles are mostly caused by the extraneous light from the red laser beam reflected by the cylindrical cuvette, however, the shape and size variations of the microspheres could also introduce mismatch to the simulation which is based on an ideal spherical particle.

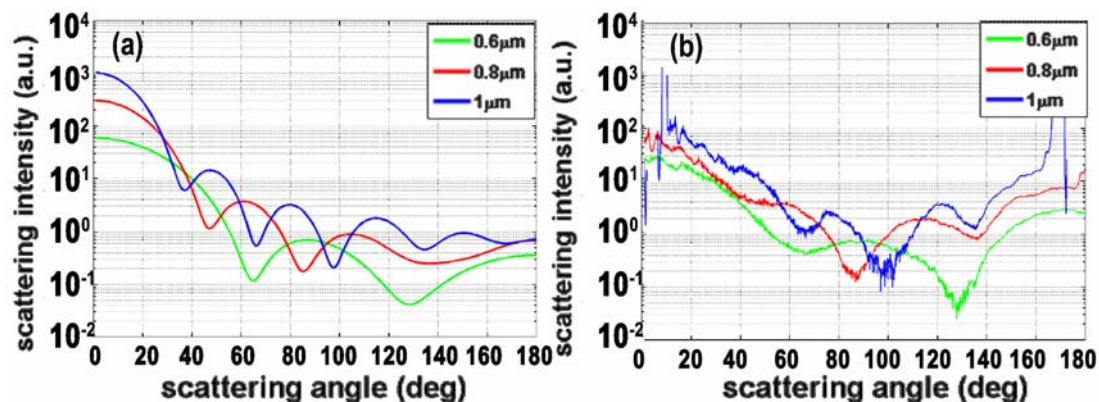


Figure 3-5: Scattering diagrams of polystyrene microspheres with diameter of 0.6 μm , 0.8 μm and 1.0 μm , respectively. (a) Simulation with GLMT on intermediate-sized sphere. (b) Experimental measurements on low-concentration suspensions.

3.7. Experimental Results

Angularly dependent scattering diagrams are measured from low-concentration (~ 1 cell per scattering volume defined) suspensions of *Synechococcus sp.* strain CC9311, *Ostreococcus sp.* strain CCE9901 and *Flavobacterium sp.* strain ALC1, respectively. In each suspension, random orientation of the cells is assumed. When the aperture is rotating at 1000 RPM, 333 sets of scattering diagrams are taken in 10 seconds, averaged and calibrated.

For prokaryote *Synechococcus sp.* strain CC9311 and *Flavobacterium sp.* strain ALC1, simulated scattering diagrams based on RM-I method (section 2.4) for homogeneous spheroid are shown in Figure 3-6(a) and Figure 3-7(a), and the experimental results in Figure 3-6(b) and Figure 3-7(b) show good agreements on the

absolute positions of the scattering maxima and minima in $40\text{-}140^\circ$ range (marked with colored lines).

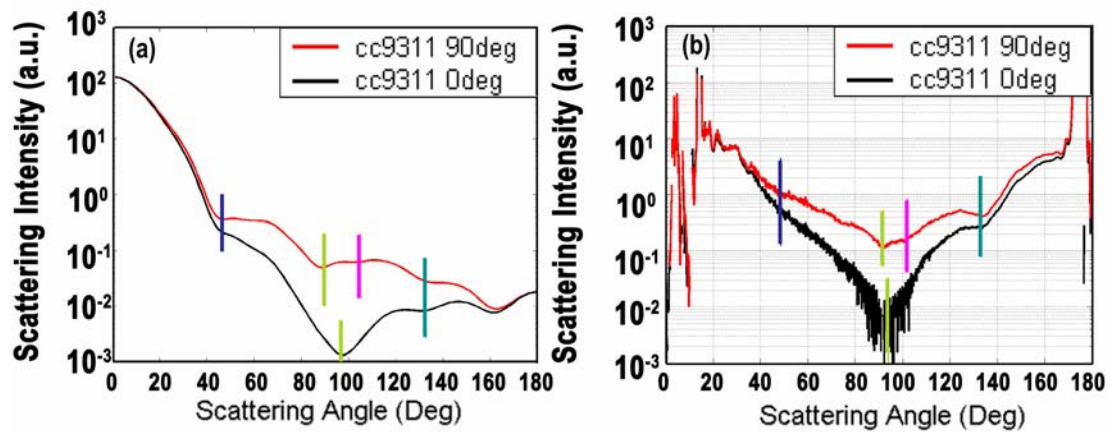


Figure 3-6. Scattering diagrams of *Synechococcus sp.* strain CC9311. (a) Simulation with RM-I method on a homogenous spheroid with $0.8\text{ }\mu\text{m} \times 0.8\text{ }\mu\text{m} \times 2.0\text{ }\mu\text{m}$ outer dimensions ($a = 0.4\text{ }\mu\text{m}$, $\nu = 2.5$ as in the spheroid equation) and $n_p = 1.406$ in seawater ($n_m = 1.339$). (b) Experimental measurements on low-concentration suspensions of *Synechococcus sp.* strain CC9311.

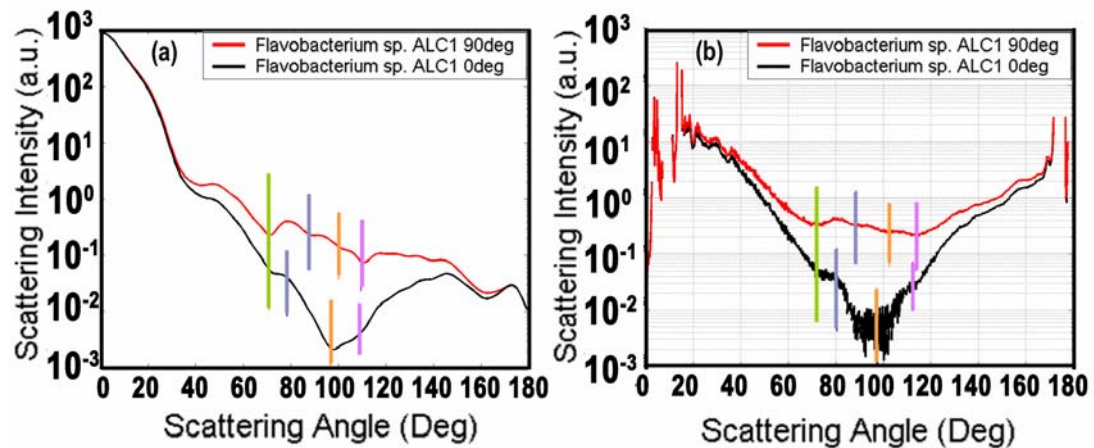


Figure 3-7: Scattering diagram of *Flavobacterium sp.* strain ALC1. (a) Simulation with RM-I on a homogenous spheroid with $1.0 \times 1.0 \times 3.5 \mu\text{m}$ outer dimensions ($a=0.5 \mu\text{m}$, $v=3.5$ as in the spheroid equation), and $n_p=1.406$ in seawater ($n_m=1.339$). (b) Experimental measurements on low-concentration suspensions of *Flavobacterium sp.* strain ALC1.

As described in section 3.3, the eukaryote *Ostreococcus sp.* strain CCE9901 is modeled as a coated spheroid ($a=0.5 \mu\text{m}$, $v=2$) with a concentric spherical core ($r=0.25 \mu\text{m}$) as the nucleus. In Figure 3-8(a), maxima and minima on the simulated scattering curves are marked with colored lines, and their matches are found at about the same angular positions in Figure 3-8(b) obtained from the average of 333 sets of experimental measurements.

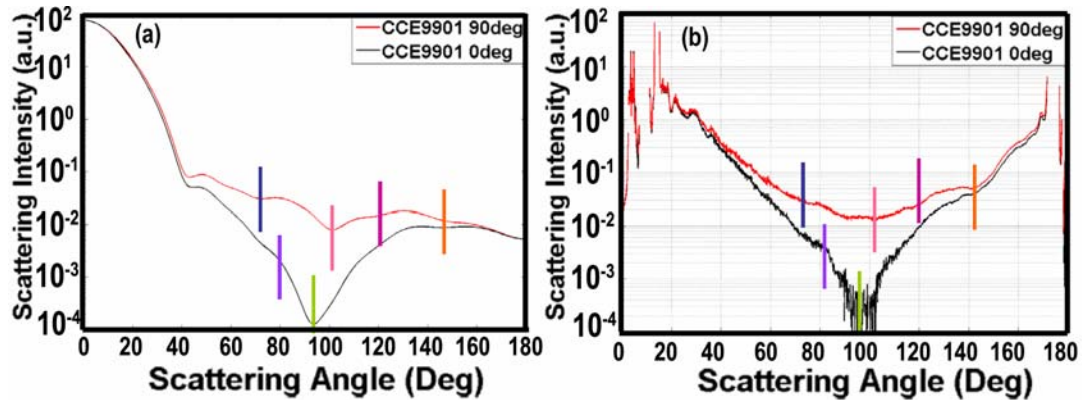


Figure 3-8: Scattering diagram of *Ostreococcus sp.* strain CCE9901. (a) Simulation with extended RM-I on a coated spheroid with $1.0 \leq 1.0 \leq 2.0 \mu\text{m}$ outer dimensions ($a = 0.5 \mu\text{m}$, $v=2$ as in the spheroid equation) and a concentric spherical core of radius $0.25 \mu\text{m}$. ($n_1=1.40$ for the spherical core, $n_2=1.37$ for the shell) in seawater ($n_m=1.339$). (b) Experimental measurements on low-concentration suspensions of *Ostreococcus sp.* strain CCE9901.

Apart from the strong signal in $0-40^\circ$ and $140-180^\circ$ range due to the reflection of light from the cuvette, main sources of mismatch between simulation and experiment are the size and shape distributions in the real sample and the inhomogeneity of the cells due to their internal morphologies. The assumption of a concentric and perfectly round nucleus in the simulation also introduces deviation from the real morphology of a cell of *Ostreococcus sp.* strain CCE9901. In spite of these errors and approximations, the selected model (coated spheroid with a concentric spherical core) yields the best agreement with experiments when compared to homogeneous spheroid and coated spheroid with uniform thickness.

3.8. Discussion

As discussed in the previous sections, the experimental data has a much higher intensity in the angular ranges of 0-40° and 140-180° than theoretical expectation due to the reflection of the laser beam at the air-glass interface. Immersing the cuvette into a medium with a similar refractive index could be an effective solution to this problem. However, the current design of the elliptical mirror has an inlet and an outlet on the ellipsoidal surface, which makes it not possible to accommodate the index matching liquid without any leakage. Accordingly, a new elliptical mirror with flat exterior surfaces at the 0° and 180° positions is designed. By this means, the inlet and outlet for the laser beam could be sealed with standard optical windows which are commercially available. Index matching liquid could therefore be loaded into the mirror and surround the cuvette. This design (Figure 3-9) also enables direct mounting to a standard optical bench and allows the cuvette to be self-aligned to the center of the mirror. An *in situ* system is being developed based on this design, which promises considerable improvement in the measurement accuracy in small and large angle ranges.

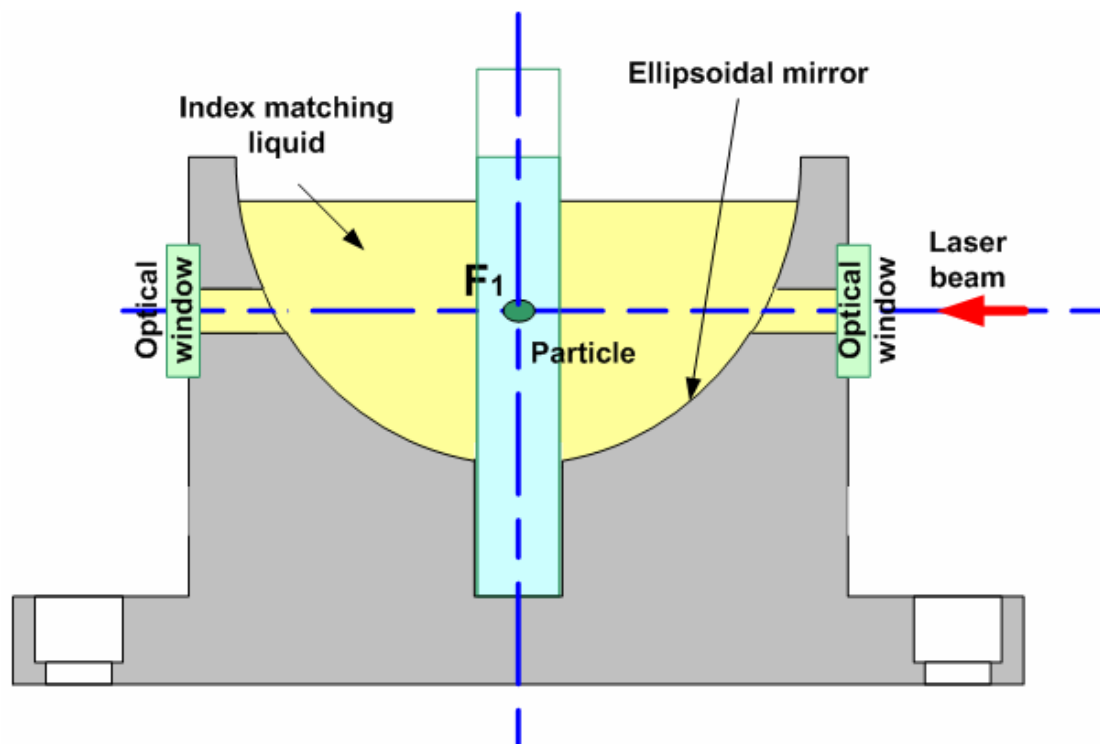


Figure 3-9: Improved elliptical mirror design that is compatible with index matching liquid and self-aligned to the cuvette.

3.9. Conclusions

Work in this chapter shows that angularly dependent scattering from suspension can be used for submicron and micron-sized cell characterization and could play an important role in understanding the distribution of marine picoplankton in different parts of the open ocean and at different times. Scattering diagrams from three main types of marine picoplankton (two prokaryotes and one eukaryote) are measured in the angular range of $0.5\text{-}179.5^\circ$ with a high angular resolution of 0.5° . Although the strong reflection of the laser beam at the air-glass interface limits the

accuracy of measurement in the angular range of $0-40^\circ$ and $140-180^\circ$, the signal to noise ratio of the scattering pattern in the middle angular range ($40-140^\circ$) is high enough to allow for characterization of submicron and micron-sized cells with very similar morphology. Good agreements between simulations and measurement are obtained, especially for the absolute positions of the scattering maxima and minima between 40° and 140° . Homogeneous spheroids are used to approximate prokaryote cells, and RM-I was used to simulate the scattering diagrams. For improved accuracy, the picoeukaryote cell is modeled as a coated spheroid with a spherical core and simulated using an extended RM-I. Further improvement on the system with index-matching liquid embedded in the elliptical mirror is discussed, which is expected to effectively reduce the reflection in small and large angle ranges.

3.10. Acknowledgements

Dr. Mirianas Chachisvilis, Dr. Jules Jaffe, and Dr. Sadik Esener are acknowledged for their expertise, supervision and innovative ideas concerning this research.

Fan Chang is acknowledged for his assistance in Matlab and Labview programming.

Dakota Watson is acknowledged for his discussion on the scattering setup.

Dr. Brian Palenik, Dr. Bianca Brahamsha is acknowledged for providing *Synechococcus sp.* strain CC9311, WH8102, and *Ostreococcus sp.* strain CCE9901 samples.

We would like to thank Xavier Mayali from Professor Farooq Azam's lab for providing the culture of *Flavobacterium sp.* strain ALC1.

Lastly, we would like to acknowledge the Scripps Institute of Oceanography for funding this research.

3.11. References

1. H. M. Shapiro, *Practical Flow Cytometry* (Wiley-LISS, New York, 1995).
2. H. C. V. d. Hulst, *Light Scattering by Small Particles* (John Wiley & Sons, Inc., New York, 1957).
3. G. C. Salzman, J. M. Crowel, J. C. Martin, T. T. Trujillo, A. Romero, P. F. Mullaney, and P. M. LaBauve, "Cell identification by laser light scattering: identification and separation of unstained leukocytes.," *Acta. Cytol.* **19**, 374-377 (1975).
4. M. R. Loken, R. G. Sweet, and L. A. Herzenberg., "Cell discrimination by multiangle light scattering," *J. Histochem. Cytochem.* **24**, 284-291 (1976).
5. M. Bartholdi, G. C. Salzman, R. D. Hiebert, and M. Kerker., "Differential light scattering photometer for rapid analysis of single particles in flow," *Applied Optics* **19**, 1573-1581 (1980).
6. T. R. Marshall, C. S. Parmenter, and M. Seaver., "Characterization of polymer latex aerosols by rapid measurement of 360° light scattering patterns from individual particles," *J. Colloid Interface Sci.* **55**, 624-636 (1976).
7. R. M. P. Doornbos, M. Schaeffer, A. G. Hoekstra, P. Slood, B. d. Grooth, and J. Greve., "Elastic light-scattering measurements of single biological cells in an optical trap," *Applied Optics* **35**, 729-734 (1996).
8. P. R. Mullaney, M. A. V. Dilla, J. R. Coulter, and P. N. Dean, "Cell Sizing: A Light Scattering Photometer for Rapid Volume Determination," *The Review of Scientific Instruments* **40**(8), 1029-1032 (1969).
9. M. Kerker, H. Chew, P. J. McNulty, J. P. Kratochvil, D. D. Cooke, M. Sculley, and M. P. Lee., "Light scattering and fluorescence by small particles having internal structure," *J. Histochem. Cytochem.* **27**, 250-263 (1979).
10. A. Brunsting and P. F. Mullaney, "Differential light scattering from spherical mammalian cells," *Biophys. J.* **14**, 439-453 (1974).

11. H. B. Steen and T. Lindmo., "Differential of light-scattering detection in an arc-lamp-based epi-illumination flow cytometer," *Cytometry* **6**, 281-285 (1985).
12. M. Kerker, "Elastic and inelastic light scattering in flow cytometry," *Cytometry* **4**, 1-10 (1983).
13. J. R. Mourant, J. P. Freyer, A. H. Hielscher, A. A. Eick, D. Shen, and T. M. Johnson, "Mechanisms of light scattering from biological cells relevant to noninvasive optical-tissue diagnostics," *Applied Optics* **37**, 3586-3593 (1998).
14. G. B. J. Dubelaar, J. W. M. Visser, and M. Donze., "Anomalous behaviour of forward and perpendicular light scattering of a cyanobacterium owing to intracellular gas vacuoles," *Cytometry* **8**, 405-412 (1987).
15. A. Dunn and R. Richards-Kortum., "Three-dimensional computation of light scattering from cells," *IEEE J. Quantum Electron.* **2**, 898-905 (1996).
16. J. Beuthan, O. Minet, J. Helfman, M. Herrig, and G. Muller, "The spatial variation of the refractive index in biological cells," *Phys. Med. Biol.* **41**, 369-382 (1996).
17. R. Barer, "Refractometry and interferometry of living cells," *J. Opt. Soc. Am.* **47**, 545-556 (1957).
18. R. Barer and S. Joseph, "Refractometry of living cells," *Quart. J. Microsc. Sci.* **95**, 399-423 (1954).
19. R. A. Meyer, "Light scattering from biological cells: dependence of backscatter radiation on membrane thickness and refractive index," *Applied Optics* **18**, 585-590 (1979).
20. J. F. Kasting and J. L. Siefert, "Life and the Evolution of Earth's Atmosphere," *Science* **296**(5570), 1066-1068 (2002).
21. C. Osolin, "Genomes of Tiny Microbes Yield Clues to Global Climate Change" (The office of science, US Department of Energy), retrieved August 13, 2003, http://www.er.doe.gov/News_Information/News_Room/2003/Genomes%20of%20Tiny%20Microbes.htm.
22. J. M. Garcia-Fernandez, N. T. de Marsac, and J. Diez, "Streamlined Regulation and Gene Loss as Adaptive Mechanisms in *Prochlorococcus* for Optimized Nitrogen Utilization in Oligotrophic Environments," *Microbiol. Mol. Biol. Rev.* **68**(4), 630-638 (2004).
23. N. Touchette, "How the Other Half Lives: Marine Microbes Capture the Limelight" (Genome News Network, 2003), retrieved September 5, 2003, 2003, http://www.genomenewsnetwork.org/articles/09_03/ocean.shtml.

24. J. B. Waterbury, S. W. Watson, R. R. L. Guillard, and L. E. Brand, "Widespread occurrence of a unicellular, marine, planktonic, cyanobacterium," *Nature (London)* **277**, 293-294 (1979).
25. S. W. Chisholm, R. J. Olson, E. R. Zettler, R. Goericke, J. B. Waterbury, and N. A. Welschmeyer, "A novel freeliving prochlorophyte abundant in the oceanic euphotic zone," *Nature (London)* **334**, 340-343 (1988).
26. B. Palenik, B. Brahamsha, F. W. Larimer, M. Land, L. Hauser, P. Chain, J. Lamerdin, W. Regala, E. E. Allen, J. McCarren, I. Paulsen, A. Dufresne, F. Partensky, E. A. Webb, and J. Waterbury, "The genome of a motile marine *Synechococcus*," *Nature (London)* **424**(6952), 1037-1042 (2003).
27. D. Marie, F. Partensky, S. Jacquet, and D. Vaultot, "Enumeration and Cell Cycle Analysis of Natural Populations of Marine Picoplankton by Flow Cytometry Using the Nucleic Acid Stain SYBR Green I," *Appl. Environ. Microbiol.* **63**(1), 186-193 (1997).
28. P. J. Wyatt and C. Jackson, "Discrimination of Phytoplankton Via Light-Scattering Properties," *Limnology and Oceanography* **34**, 96-112 (1989).
29. A. Messmer, T. J. Kane, J. Prentice, B. Concannon, A. Laux, and L. Mullen are preparing a manuscript to be called "Volume Scattering Function Measurement and Comparison of Phytoplankton Species."
30. M. E. Lee and M. R. Lewis, "A New Method for the Measurement of the Optical Volume Scattering Function in the Upper Ocean," *Journal of Atmospheric and Oceanic Technology* **20**, 563-571 (2003).
31. Z. Ulanowski, R. S. Greenaway, P. H. Kaye, and I. K. Ludlow, "Laser diffractometer for single-particle scattering measurements," *Measurement Science and Technology* **13**, 292-296 (2002).
32. Retrieved <http://www.internal.eawag.ch/~steiner/teich/mooralgen/bilder/8.jpg>.
33. Retrieved http://scrippsnews.ucsd.edu/article_detail.cfm?article_num=586.
34. A. Z. Worden, J. K. Nolan, and B. Palenik, "Assessing the dynamics and ecology of marine picophytoplankton: The importance of the eukaryotic component," *Limnology and Oceanography* **49**(1), 168-179 (2004).
35. R. Drezek, A. Dunn, and R. Richards-Kortum, "A Pulsed Finite-Difference Time-Domain (FDTD) Method for Calculating Light Scattering from Biological Cells Over Broad Wavelength Ranges," *Optics Express* **6**(7), 147-157 (2000).

36. X. Mayali, (personal communication, 2006).
37. C. F. Bohren and D. R. Huffman, *Absorption and Scattering of Light by Small Particles* (John Wiley & Sons, New York, 1983).
38. F. T. Gucker, J. Tuma, H. M. Lin, H. C. M., S. C. Ems, and T. R. Marshall, "Rapid measurement of light-scattering diagrams from single particles in an aerosol stream and determination of latex particle size," *Aerosol Sci.* **4**, 389-404 (1973).
39. D. Watson, N. Hagen, J. Diver, P. Marchand, and M. Chachisvilis, "Elastic Light Scattering from Single Cells: Orientational Dynamics in Optical Trap," *Biophys. J.* **87**(2), 1298-1306 (2004).
40. R. C. MacDonald, R. I. MacDonald, B. P. M. Menco, K. Takeshita, N. K. Subbarao, and L.-r. Hu, "Small-volume extrusion apparatus for preparation of large, unilamellar vesicles," *Biochimica et Biophysica Acta (BBA) - Biomembranes* **1061**(2), 297-303 (1991).

4. Axicon-Based Dynamically Resizable Three-Dimensional Annular Laser Trapping for Self-Propelled Cell Analysis

In this chapter, a continuous ring-shaped laser trap is presented which could be used for multi-level and high-throughput (tens to hundred sperm per ring) sperm sorting based on their motility and chemotaxis. Based on axicons, the annular laser trap can confine microparticles in three dimensions, and the diameter of the ring can be dynamically adjusted. Under a laser power of only tens of milliWatts, human sperm with low to medium velocity could be stopped or forced to change their trajectories to swim along the ring due to the optical gradient force in the radial direction. As a result, the effect of radiation and optical force on sperm energetics could be investigated in a more gentle and quantitative way. The application of this method could be extended to motility and bio-tropism studies of other self-propelled cells, such as algae and bacteria.

The main contributions of the research reported in this chapter include utilizing the special optical properties of axicons to generate a continuous ring focus with optical gradient force only exist in the radial direction, analyzing the effect of laser illumination, optical force or external obstacles on sperm swimming behavior by confining them along the ring with low laser power, and provide potential for multi-level sorting of self-propelled cells based on motility and chemotaxis response.

4.1. Background and Motivation

Laser trapping in the near infrared regime is a noninvasive and microfluidic-compatible biomedical tool which has been widely applied for manipulation and physiological study of biological cells¹⁻⁴ and organelles.⁵

As a technology aimed at high throughput laser trapping, Optophoresis provides the ability to analyze multiple cells in parallel and evaluate cellular responses to a drug treatment without any need for labeling or cell processing (Figure 4-1) by moving cells with an optical gradient field.

Cells suspended in an aqueous medium are subject to forces other than optical (Figure 4-1), principally viscous drag, surface interactions, and gravity. The strengths of the transverse and axial optical forces depend on the refractive indices of the cell and the medium, the cell's size and morphology, and the intensity, shape, and wavelength of the optical gradient. Gravity, corrected by the buoyancy of the medium, is related to the cell's volume and the respective densities of the cell and the medium. Viscous drag is determined by the viscosity of the medium and the cell's size, morphology, and velocity. Surface interaction is a function of substrate surface properties and the cell's size, morphology, and membrane composition. Under the influence of gravity, the cells settle on the bottom of the sample well. When it is exposed to a moving optical gradient, the optical force drives the motion of the cell. The axial component typically opposes the gravitational force while the transverse component pulls the cell toward the maximum of the optical intensity. Viscous drag and surface interactions produce dissipative forces that prevent the motion of the cell.

The sum of the optical force and the dissipative forces determines is a reflection of the cell's properties.

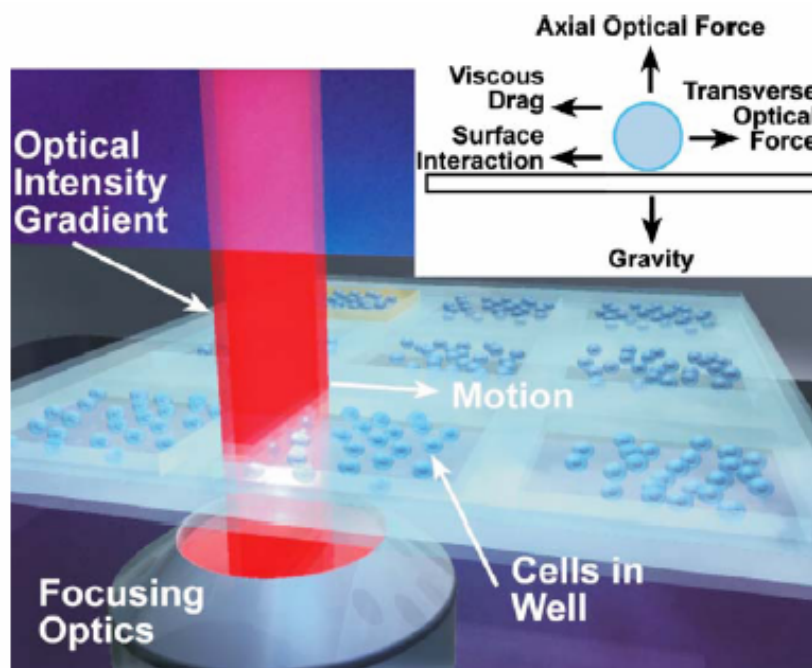


Figure 4-1: Optophoresis, schematic diagram. An optical gradient is imaged into the sample well. The well is translated at constant velocity past the stationary gradient to produce a moving optical gradient with respect to the cells. A cell experiences forces induced by the moving optical gradient, dissipative forces due to its relative motion with respect to the aqueous medium in which it is suspended and the surface of the well, and buoyancy-corrected gravity, as shown in the inset.⁶

Biological differences between two cell populations can be assayed with the moving optical gradient by various methods. For example, the speed of translation of the optical gradient at which the dissipative forces overcome the transverse optical force, the escape velocity, can be measured for each cell and accumulated for a given population to provide a signature for that population. Movie frames in Figure 4-2

demonstrates the separation of cancer cells from red blood cells using Optophoresis. When the sample well is moved with respect to the static scanning laser line, cells are attracted to the optical gradient. The cancer cells see a stronger potential well compared to the normal red blood cells. When the laser line is moved with a higher speed, the cancer cells stay trapped while normal cells escape. As a result, two cell populations are separated.

Optophoresis has been used for leukemia diagnosis, however, it has limitations in analysis of self-propelled cells, which are the focuses of the research presented in this chapter.

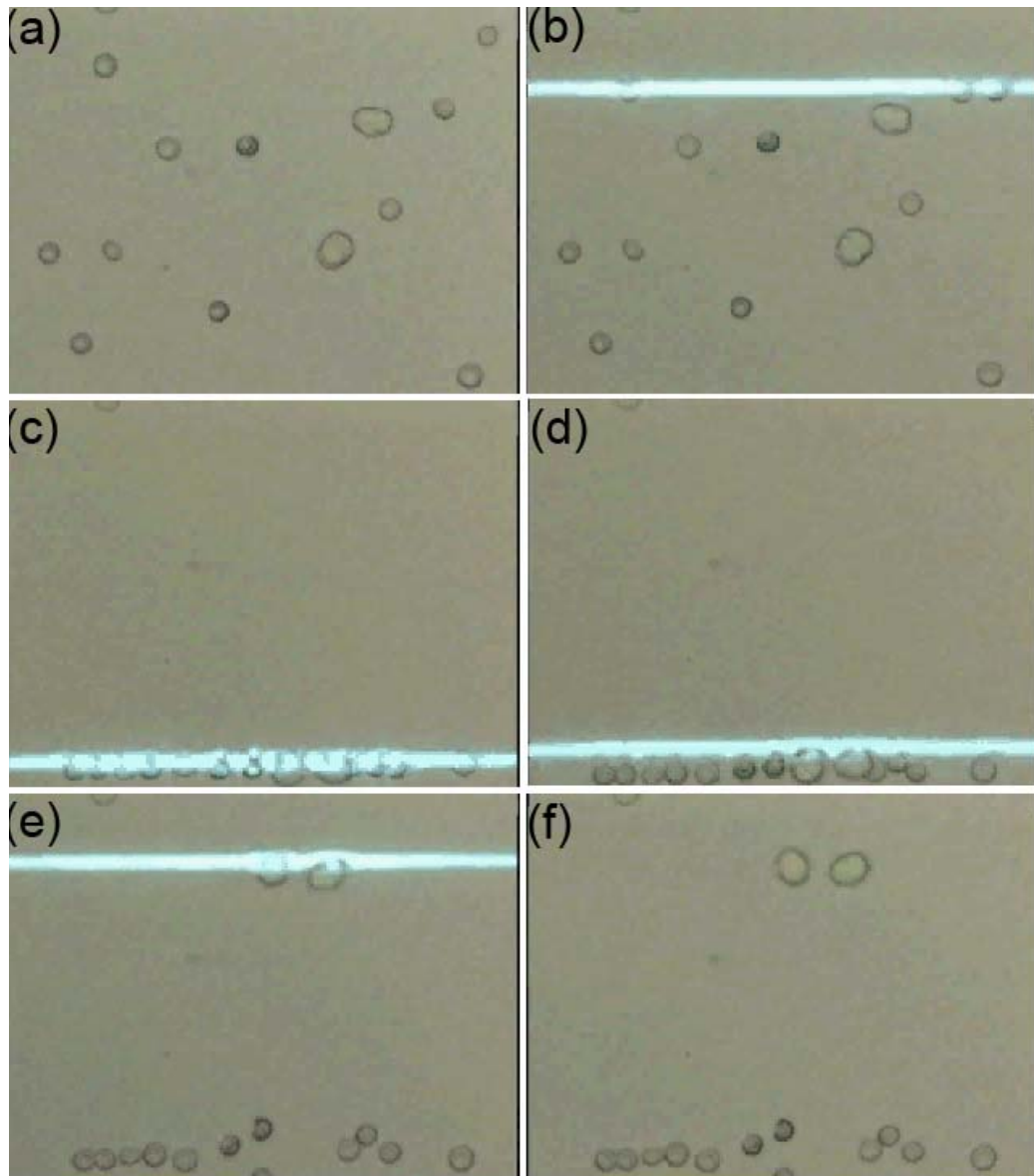


Figure 4-2: Optophoresis of blood cells. (a) Sample well containing cancer cells and normal red blood cells. (b) A scanning laser line is introduced to the sample well and three red blood cells are attracted to the optical gradient field. (c) All cells are trapped by the scanning laser line and move with it to the bottom of the field of view. (d) As the scanning laser line move faster, trapped cells significantly displace from the center of the gradient field. (e) Normal red blood cells all fall out of the trap and stay near the bottom of the field of view, while cancer cells stay in the trap. (f) Cancer cells are moved to the top of the field of view by the scanning laser line. (Courtesy of Genoptix, Inc.)

With the deterioration of the environment and an increasing economic interest on animal husbandry, artificial insemination (AI) has become indispensable. It brings enormous profit to various animal farms including fish farms, as well as helps zoological societies to save endangered species. To make artificial insemination more effective, fertility experts grade sperm according to their overall quality before cryopreserving them for future use. Among many factors involved in the expression of sperm quality grading, initial motility score (IMS) (i.e., the product of initial motility (MOT%) and the square of speed of progression (SOP) score),⁷ and hyperactivity (i.e., a distinctive motility pattern of sperm characterized by vigorous flagellar movements essential for fertilization),⁸ play the two most important roles. Noninvasive and high throughput analysis of sperm motility and hyperactivity is of great significance for artificial insemination and genetic improvement programs. Conventional techniques evaluate one sperm at a time subjectively and qualitatively, which is labor intensive and short of a universal standard. These considerations give rise to a strong need for an automated, quantitative, and objective assessment tool for sperm quality. In the last decade, computer aided sperm analysis (CASA) has been developed to offer objective assessment of sperm motility for large population. However, the thin chambers (30 μm) used in CASA may affect the behavior of sperm that swim with large transverse amplitudes (e.g. monkey sperm),⁹ and the errors encountered by CASA when dealing with phase contrast images often lead to errors in the actual sperm number detected in the field. Finally, while CASA can measure the motility of sperm, it can not provide

information on swimming force that is potentially useful in assessment of sperm viability.

4.2. Single Point Optical Trapping for Sperm Motility Study

Since the late 1980s, researchers have been using single spot laser tweezers to trap individual sperm and quantitatively evaluate the motile force generated by a sperm while it is swimming.¹⁰⁻¹⁵ These studies determined that the minimal laser power needed to hold a sperm in the trap (threshold escape power) is directly proportional to the sperm's swimming force ($F = Q \sqrt{P} / c$, where F is the swimming force, P is the laser power, c is the speed of light in the medium, and Q is the geometrically determined trapping efficiency parameter).¹⁰ Sperm swimming force measurements have been used to evaluate sperm viability by characterizing the effects of sperm cryopreservation,¹² comparing the motility of epididymal sperm to ejaculated sperm,¹¹ and investigating the medical aspects of sperm activity.^{12, 13} In addition, a relationship between sperm motility and swimming pattern was found for human and dog sperm.^{15, 16} They found that sperm with zigzag swimming pattern have stronger power than those swimming in straight lines, and as swimming speed increased, so did average escape power.

Single spot laser tweezers provides a quantitative analysis of individual sperm motility, nevertheless it has some drawbacks. One example is the interference from untrapped sperm. When a sperm of interest is caught by the single spot laser tweezers, it needs to be held for a time sufficiently long for motility analysis (Figure 4-3 (a)-(b)). However, frequently, another sperm swims through the trapping spot, and invalidates

the measurement (Figure 4-3 (c)-(d)). Additionally, a single spot laser trap still analyzes one sperm at a time, therefore is limited in throughput, lacks the ability of *in-situ* sorting based on motility, and has difficulty in assessing the role of chemotaxis — a critical feature of sperm in response to the diffusion gradient of chemicals released by the egg and surrounding cells of the cumulus oophorus, which may help to explain infertility and provide new approaches to contraception.¹⁷ Finally, single spot laser tweezers measure sperm by stopping it completely, thus can not be used to dynamically monitor the change in swimming behavior of a sperm under the influence of a laser beam.

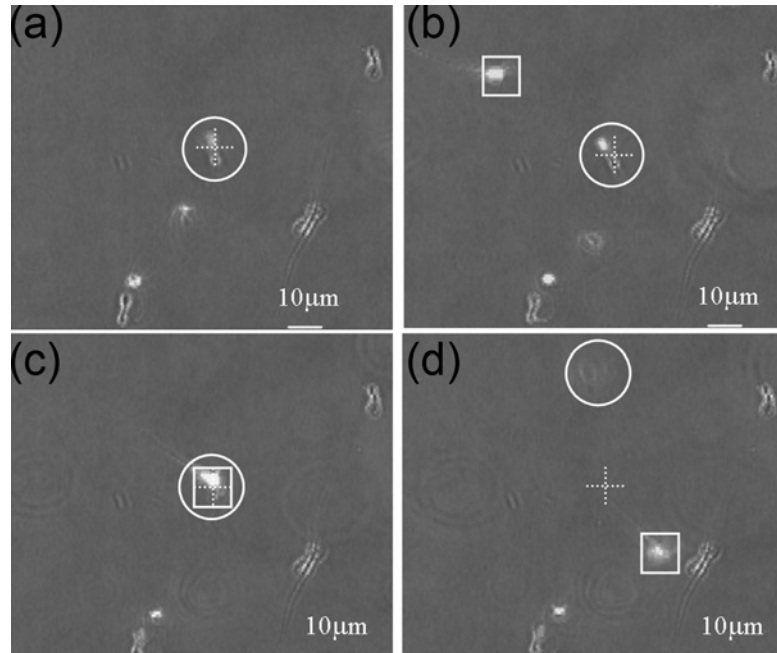


Figure 4-3: Interference to single trap sperm analysis introduced by non-targeted sperm. (a) A sperm (inside the white circle) is trapped by a single spot laser trap (indicated by the white dotted cross hair) for analysis. (b) A second sperm (inside the white square) swims towards the trapping spot. (c) The second sperm swims into the trapping spot, and interferes with the analysis of the first trapped sperm. (d) Both sperm swim out of the trap.

4.3. Axicon and Its Applications

An axicon, as defined by McLeod in 1954,^{18, 19} is an optical element that produces a long, narrow focal line along the optical axis instead of the usual point focus. Among many different kinds of axicon (rings, cylinders, etc.), the single refracting cone lens is the most common form (Figure 4-4).²⁰ Because of its unusual properties, this device has been found to be quite useful in many applications. In laser machining²¹, the axicon is used as an optical element producing a circle with a Fourier

transform lens because of its ability to deliver a large amount of confined energy inside a ring pattern. More recently, this advantage has been employed in corneal surgery.²² The narrower central spot that is available over long axial distances was used in aligning and trapping atoms,^{23, 24} along the axis with the use of laser-trapping technology.

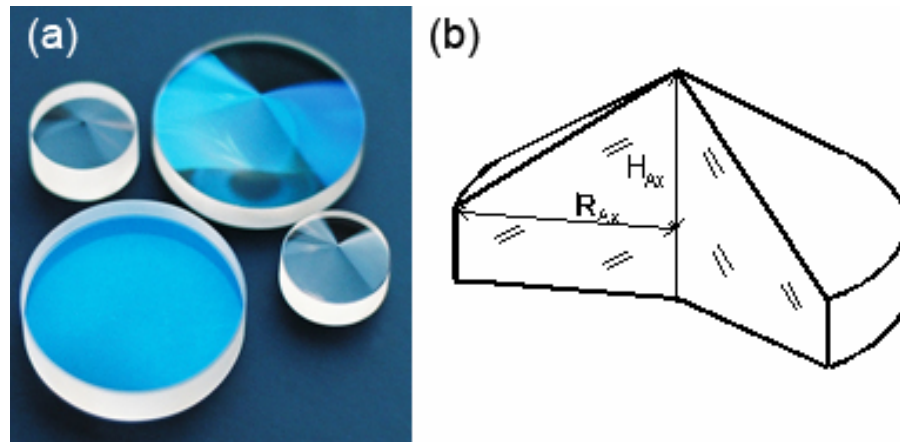


Figure 4-4: The axicons, also known as conical lenses or rotational symmetrical prisms. (a) photo (courtesy to Del Mar Photonics, Inc.), (b) schematic diagrams showing the cross-section of an axicon. R_{Ax} is the radius of the axicon, and H_{Ax} is the height of the conic surface.²⁵

The ability of an axicon to transform a Gaussian beam into a “non-diffracting” Bessel beam also leads to a new type of optical trap which is capable of axial aligning, guiding and stacking of microparticles.²⁶

4.4. Annular Laser Trap Based on Axicons

Based on the above information, a new type of optical trapping based on axicons is proposed, designed and demonstrated, which can not only serve as a force

shield to protect the analytical field from other sperm (Figure 4-5 (a)), but also enable high-throughput manipulation and multi-level sorting of sperm according to their motility and chemotaxis responses (Figure 4-5 (b)-(c)). One advantage of a “ring trap” over a “line trap” is the ability to provide an equal-distance (from the center) condition which is important for biological tropism study. When an attractant is fixed in the center of the ring, laser power or ring diameter can be adjusted so that only cells swimming with sufficient energy and sensitivity to the attractant’s local concentration gradient will have enough energy to overcome the trap and reach the attractant. In addition, a “ring trap” provides a way to confine a swimming cell in the field of view for an extended period of time without having to deal with sharp turns and changes in swimming curvature.

There are several different ways to create an annular trap. With mechanical scanning, a ring could be generated with a fast scanning focus spot. However, this reduces the average exposure time and introduces a tangential drag force that might affect the swimming behavior of a sperm. Diffractive optics and holography generally have low power efficiency, which is an important consideration in sperm trapping, because a single sperm trap requires 100~200 mW at the specimen plane.²⁷ A computer generated hologram (CGH) capable of flexibly changing the ring size and trapping depths requires a high resolution spatial light modulator. In contrast, an axicon has low cost, negligible energy loss, and high flexibility. Based on these advantages, the annular laser trap is built with axicons.

Different from the single spot laser trap which focuses hundreds of milliwatts to immobilize a sperm, the ring-shaped trap distributes only tens of milliwatts on a sperm, and because of the optical properties of an axicon, the gradient force of the annular laser trap exists only in the radial direction, allowing the sperm to swim along the ring without having to come to a complete stop. Consequently, the effect of optical force, radiation and even external obstacles on sperm swimming pattern and membrane potential (with the aid of the specific fluorescence probe) can be investigated in greater detail.

This new form of optical trapping is expected to benefit a variety of cell motility and biotropism (phototaxis, geotaxis, galvanotaxis, etc.) related studies.

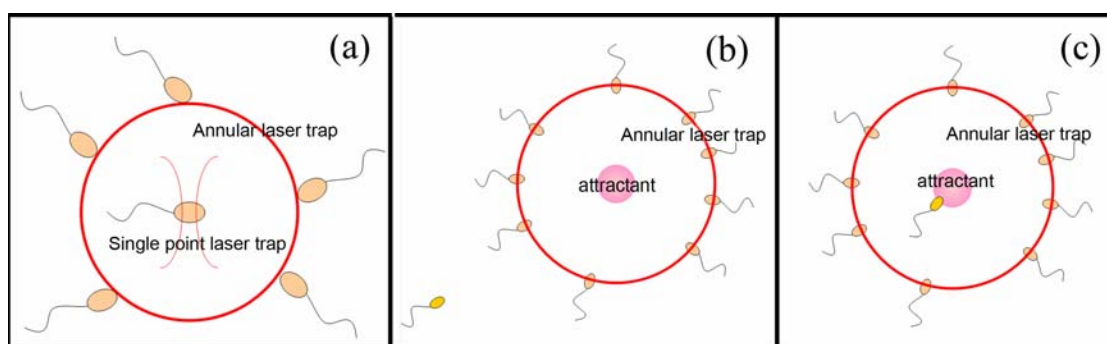


Figure 4-5: Applying a ring-shaped laser trap to facilitate sperm analysis. (a) A ring trap works as a force shield to protect sperm held by single point laser trap from interference introduced by other untrapped sperm. (b) In sperm motility and chemotaxis research, weak sperm with low swimming power and low response to central attractant are held back by the optical gradient field of the ring trap. (c) A sperm with strong response to the central attractant develops an above-threshold swimming force to pass through the ring trap and reach the attractant in the center of the ring.

4.5. Optical Design of the Annular Laser Trapping System

According to earlier research², the deviation of the trapping spot from the optical axis is almost linearly proportional to the inclination angle θ of the input collimated beam. A uniform annular trap requires that incident light be composed of collimated beams from all directions (0~360° azimuthal angle) with the same angle to the optical axis, i.e. the input light is a cone of collimated beam intersecting the back aperture of objective. The thickness of the cone should be equal to the diameter of the back aperture so that the numerical aperture of the objective is fully utilized, and the beams are focused tightly enough to guarantee high gradient force.

The above considerations of the annular trapping system are summarized in Figure 4-6 as the schematic diagram of the annular trapping system. The laser beam is collimated, expanded by a telescope lens pair and directed normally to the flat surface of an axicon. As a lens composed of a flat surface and a conical surface, an axicon bends normal-incident light toward its tip without affecting its degree of collimation. The beam emerging from the conical surface of the axicon is bent toward the optical axis at an angle $\beta = \arcsin(n \sin \gamma) - \gamma$, where γ is the base angle of the axicon and n is the refractive index of the lens material. A focusing lens converts the cone of collimated beams into a ring, which is then imaged in the specimen plane via the tube lens-objective combination.

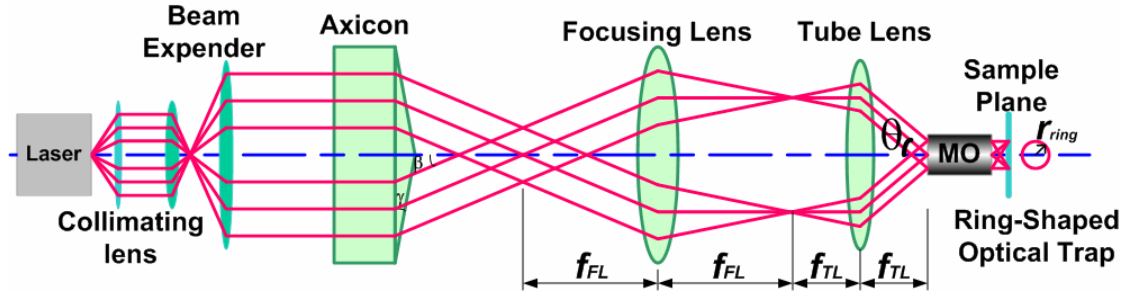


Figure 4-6: Schematic diagram of the optics designed for annular laser trapping (not to scale), MO---Microscope Objective.

Since the focusing lens and the tube lens are working together as a telescope, the inclination angle of the light beams incident on the objective is $\theta = \beta f_{FL} / f_{TL}$, where f_{FL} and f_{TL} are the focal lengths of the focusing lens and the tube lens, respectively.

Accordingly, the radius of the ring trap can be calculated as

$$r_{ring} = \delta = f_{EFL} \cdot \tan(\theta) = f_{EFL} \cdot \tan\left(\frac{f_{FL}}{f_{TL}} \beta\right) = f_{EFL} \cdot \tan\left[\frac{f_{FL}}{f_{TL}} (\arcsin(n \sin \gamma) - \gamma)\right] \quad (4.1)$$

where f_{EFL} is the effective focal length of the microscope objective.

The wavelength used for trapping is 1070 nm. To obtain as high power throughput as possible, a specially-designed dichroic mirror is employed which could reflect incident light from the left side of the microscope (Axiovert 200M, Zeiss, Germany) upwards the objective. In this way, the microscope-embedded tube lens that is anti-reflection (AR) coated for visible light is avoided, and a 1070 nm AR-coated plan-convex singlet lens ($f_{TL}=175\text{mm}$, KPX196AR.18, Newport, Irvine, CA) is used as a substitute. A 1" BK7 ($n=1.506$) axicon lens with broad-band AR coating and base

angle $\gamma=10^\circ$ (Del Mar Photonics, San Diego, CA) is chosen so that together with the focusing lens ($f_{FL}=50\text{mm}$, CPX010AR.18, Newport, Irvine, CA), the tube lens and the microscope objective (Plan-Apochromat, DIC, 63μ NA=1.4, oil immersion, Zeiss, Germany), a ring trap with a diameter of hundreds of micrometers could be formed.

Ray tracing simulations (ZEMAX, Bellevue, WA) with a plane wave input show a sharp and uniform ring focus on the specimen plane (in Figure 4-7(b)-(d)). Although some rays fail to focus due to the off-axis aberration---coma, both the spot diagram (Figure 4-7(b)) and the cross-section (Figure 4-7(d)) show that they only occupy a negligible percentage of the light. The Huygens PSF cross-section in transverse plane Figure 4-7(c) shows two intensity peaks with high gradient, indicating a strong gradient force on the specimen plane.

The radius of the ring obtained from the spot diagram simulation (Fig 4-7(b)) is about $125\ \mu\text{m}$, which agrees well with the calculation according to equation (4.1).

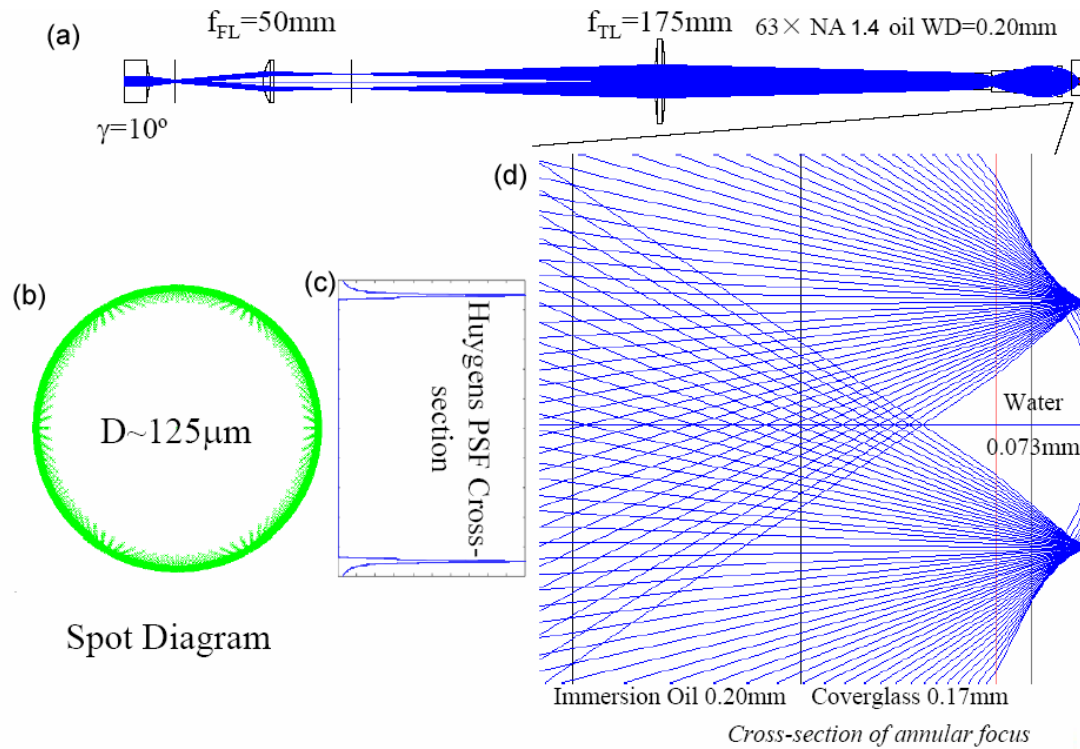


Figure 4-7: ZEMAX simulations of axicon-based ring trap system. (a) System layout. (b) Spot diagram at the specimen plane shows the size and quality of the ring focus. (c) Huygens PSF cross-section shows a strong gradient of light intensity on the specimen plane. (d) Close-up of the system layout near the specimen plane gives a cross-section view of the ring focus formation, only negligible amount of rays failed to focus due to coma.

4.6. Dynamically Resizable Annular Laser Trap

The faster a sperm swims, the higher the laser power is needed for trapping. With the total input power fixed, diameter changes of the annular trap lead to a variation of trapping powers per spot. As a result, sperm with different motility will escape the trap at different time (Figure 4-8). Thus, multi-level sorting is allowed. Additionally, since the size of sperm may vary between species, resizability of the

system makes it possible to study different species without redesign of the optics. Finally, a resizable ring can be used to study the diffusion length of an attractant, and monitor sperm swimming behavior under radial confinement (optical gradient force in the radial direction) with various curvatures.

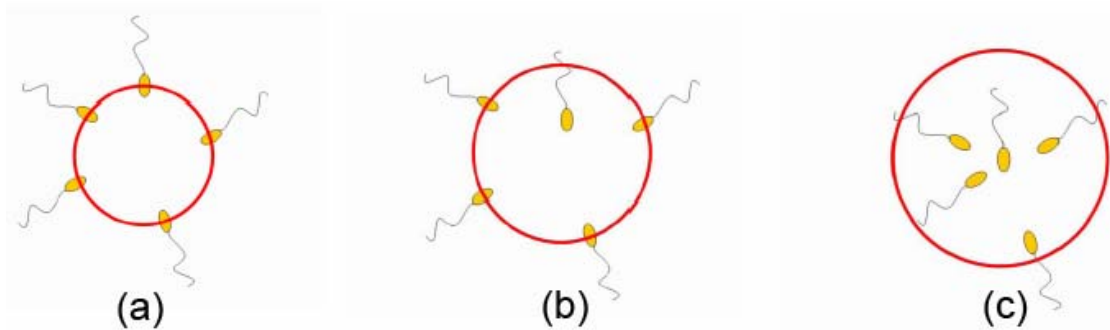


Figure 4-8: Under a fixed total laser power, with increased ring size (from (a) to (c)), the average trapping power per sperm is reduced, thus more sperm can escape the annular trap and reach the center (assuming there is an attractant at the center of the ring).

The size of the ring focus is determined by the apex angle of the input light cone (θ in Figure 4-6). To change this angle dynamically without changing the thickness of the cone which corresponds to the filling degree of the objective back aperture, Axicon 2 and Axicon 3 (2", $\gamma=20^\circ$, Del Mar Photonics, San Diego, CA) are added (Figure 4-9). The ability of an axicon to bend incoming light without changing its collimation degree makes an axicon-pair a better choice than a normal telescope-lens-pair. When a normal telescope lens pair is used, the changing of θ is accompanied by a change of the beam size, which will result in an over-filling or under-filling of

the objective back aperture. ZEMAX Simulations show that with all other elements fixed, axial translating axicon 3 for 38 mm corresponds to a ring diameter change from 346 μm (Figure 4-10(a)) to 69 μm (Figure 4-10(b)).

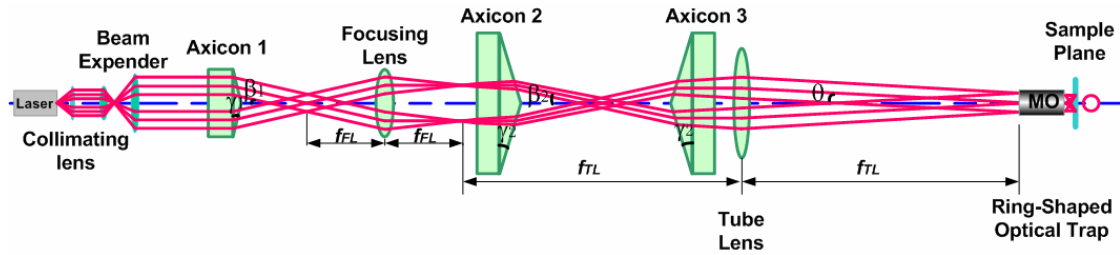


Figure 4-9: Schematic diagram of the optics designed for resizable annular laser trapping (not to scale), MO---Microscope Objective.

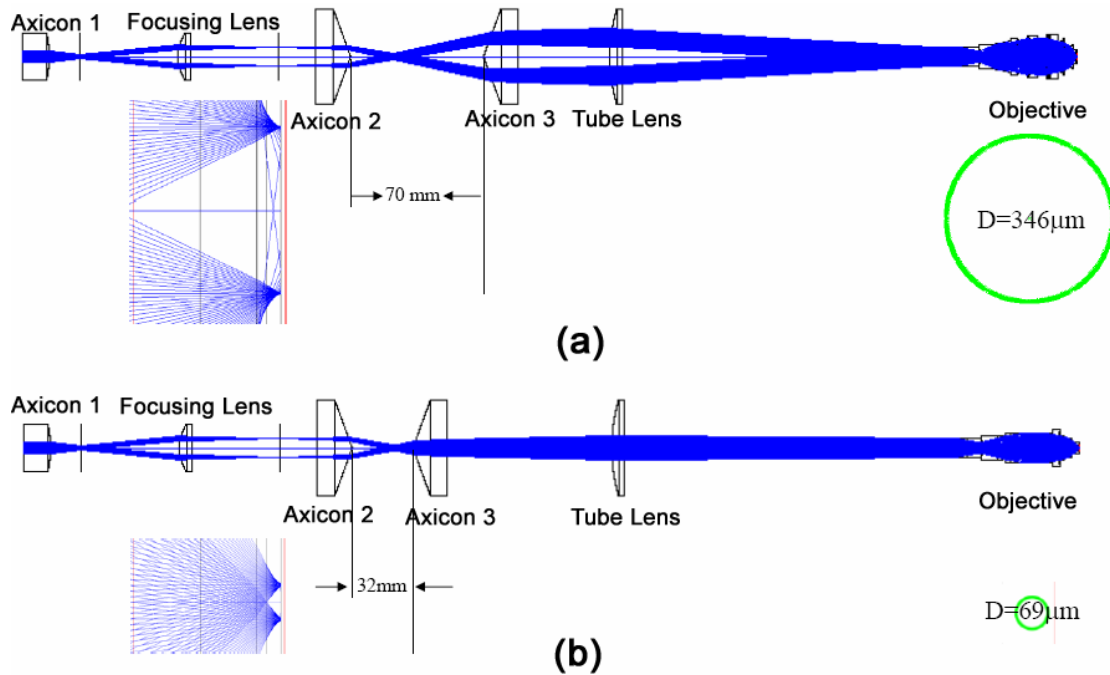


Figure 4-10: ZEMAX simulations of adjustable annular laser trap with $63\times$ NA1.40 oil immersion objective. (a) Layout, focus close-up, and sample plane spot diagram for maximal ring size, (b) Layout, focus close-up, and sample plane spot diagram for minimal ring size.

4.7. Effect of Beam Profile on Trapping Performance

Since the axicon divides all the incoming beams with respect to the optical axis and bends them towards its apex angle, the light emerging from it will enter the objective lens from every direction (all azimuthal angles). In ZEMAX simulation, a plane wave with uniform intensity distribution was used, therefore, after the axicon, all the beams incident to the objective for trapping still have uniform intensity patterns. However, the beam profile from most commercially available laser is a Gaussian distribution, which, when incident on the axicon, will result in an asymmetrical

intensity pattern (half-Gaussian) from each azimuthal angle (Figure 4-11(a)). According to Fourier transform, this input beam with an asymmetrical intensity distribution leads to a tilted phase front at the specimen plane, which indicates that the direction of total photon momentum transfer is not perpendicular to the specimen plane, and the stability of the trap is significantly degraded. By modifying the input beam profile to a top-hat, the asymmetrical intensity distribution after the axicon can be eliminated, and the stability of the trap can be improved (Figure 4-11(b)).

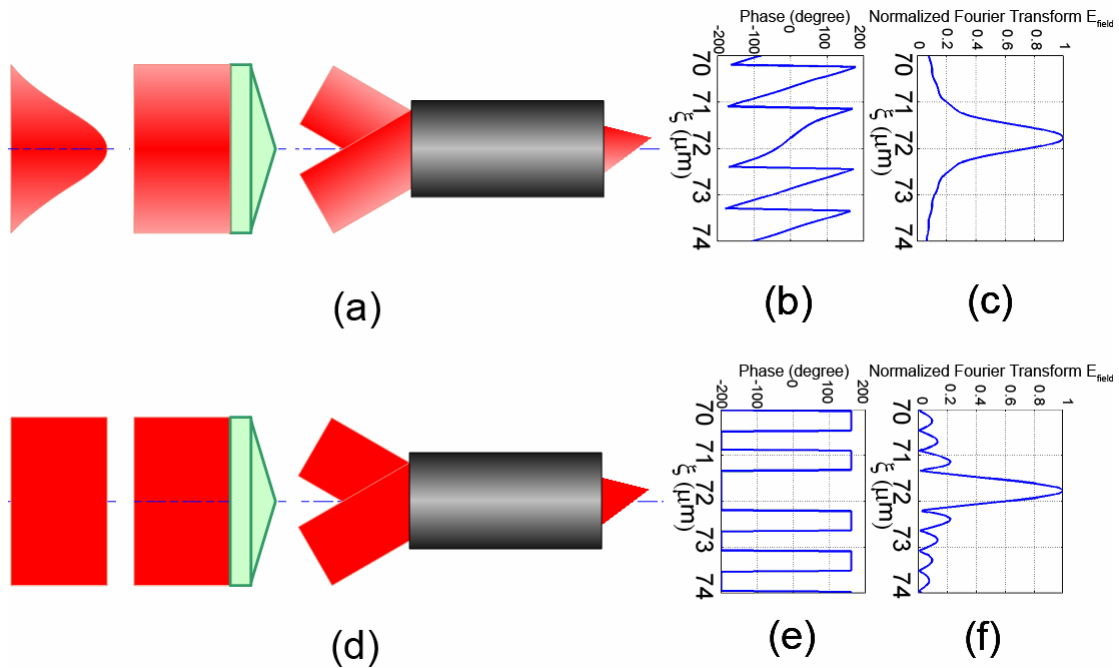


Figure 4-11: Effect of input beam intensity distribution on trapping performance of the ring. (a) For a Gaussian input, whose intensity decreases from the center, the beams after the axicon have a non-uniform and non-symmetrical intensity patterns. (b) The phase distribution on the specimen plane after the objective is not symmetrical. (c) The intensity distribution on the back focal plane of the objective (specimen plane). (d) For a top-hat incident with uniform intensity, each beam emerging from the axicon in one azimuthal angle incident the objective lens with a uniform intensity. (e) The phase distribution on the specimen plane after the objective is symmetrical. (f) The intensity distribution on the specimen plane after the objective.

4.8. Experiments with Annular Laser Trap Based on One Axicon

4.8.1. Experimental Setup

The experimental setup is depicted in Figure 4-12, and Figure 4-13 is the corresponding photo of the single Axicon system. The light beam from a CW Ytterbium fiber laser with 1070 nm wavelength (PYL-20M, IPG Photonics, Oxford,

MA) is collimated and expanded via a 3μ beam expander (T81-3X, Newport Corp., Irvine, CA). According to section 4.7, a refractive beam shaper (GBS-AR14, Newport Corp., Irvine, CA) is used to convert a Gaussian laser beam into a collimated flat top beam such that a better performance of the ring-shaped trap could be obtained. A telescope lens pair shrinks the beam so that the thickness of the light cone input to the objective becomes equal to the diameter of the back aperture, and the numerical aperture of the trapping beam is maximized.² Upon Axicon1 (1", $\gamma=10^\circ$, Del Mar Photonics, San Diego, CA), the input beam is divided with respect to the optical axis and bent towards the axis at an angle $\beta=\arcsin(ns\sin\gamma)-\gamma=5.16^\circ$, where γ is the base angle and n is the refractive index of the axicon. At the back focal plane of the focusing lens (FL), a ring image is formed that is conjugated to the ring focus at the specimen plane. After the tube lens (TL), the laser light is sent into an inverted microscope (Axiovert 200M, Zeiss, Germany) and directed to the objective (63μ oil immersion, NA=1.4, Zeiss, Germany) by the dichroic mirror.

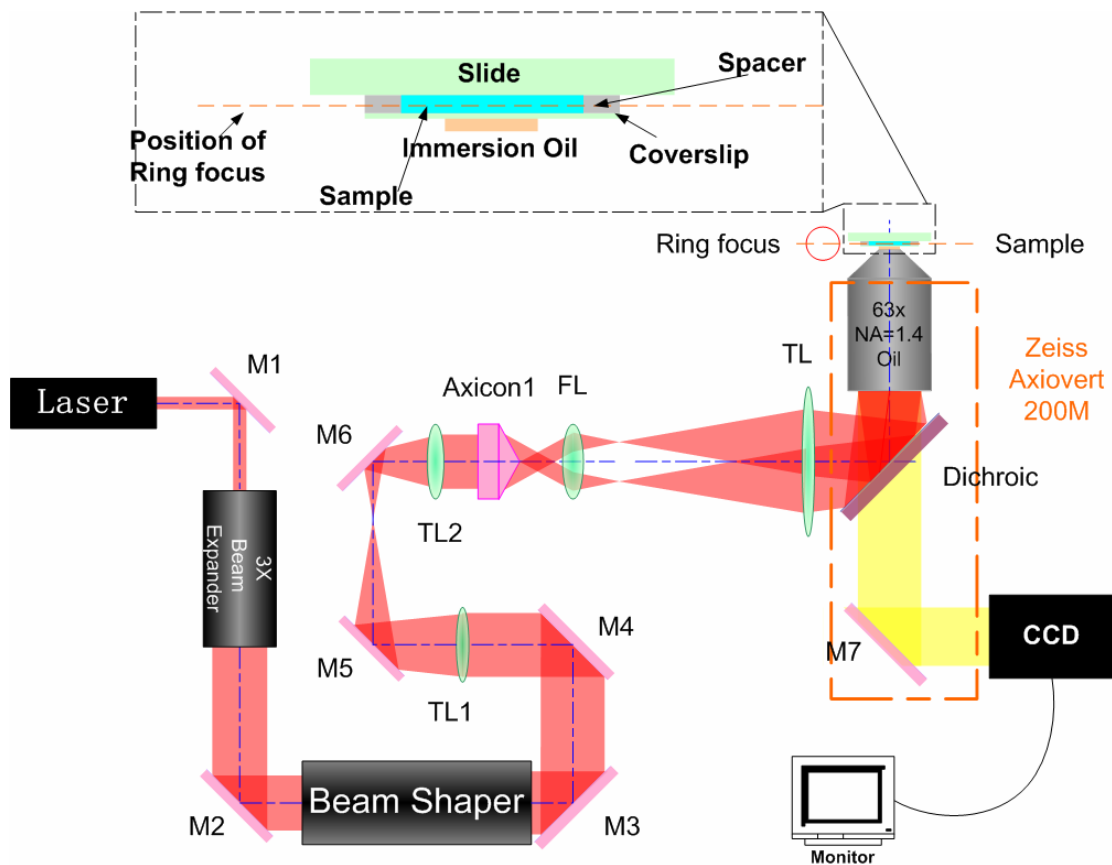


Figure 4-12: The schematic diagram of the annular laser trapping system. M1-M7---Mirrors, TL1---Telescope lens 1, TL2---Telescope lens 2, FL---focusing lens, TL---Tube lens.

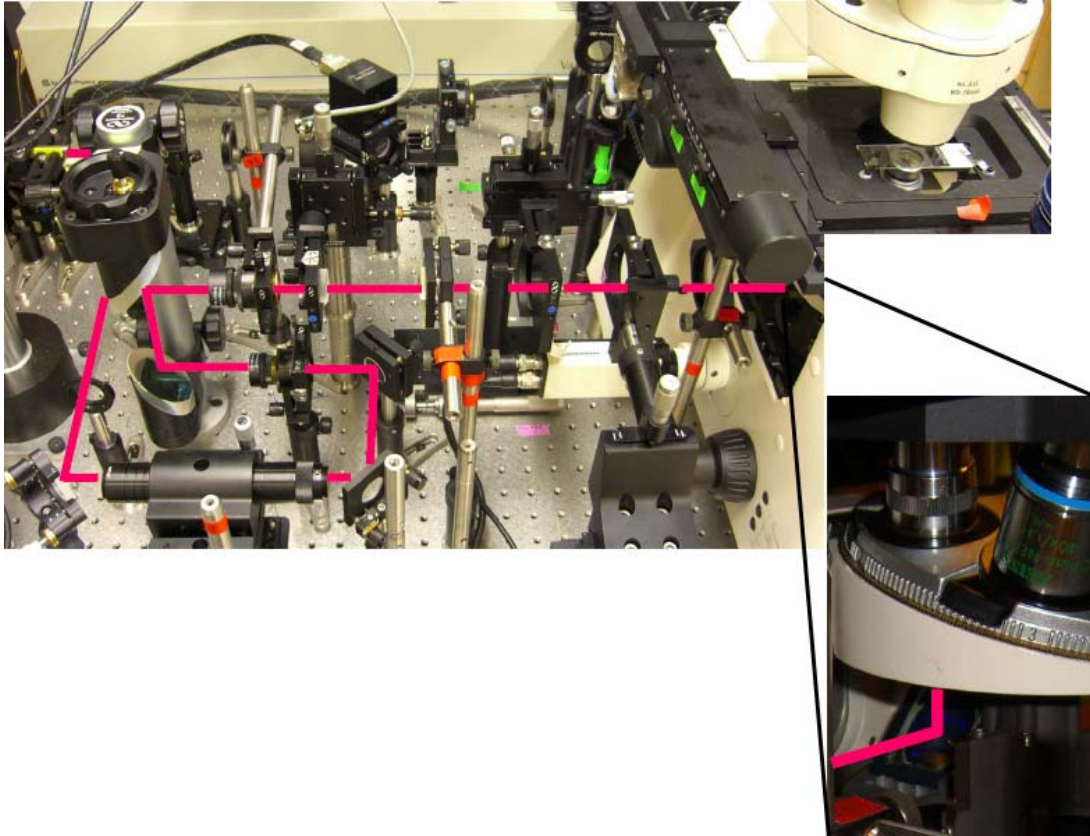


Figure 4-13: Photo of the single axicon annular trapping system. Inset: close up of the specially mounted dichroic.

The ring-shaped trap obtained at the specimen plane has a diameter of $120\ \mu\text{m}$, which could accommodate up to 70 human sperm, whose head diameter is approximately $5\ \mu\text{m}$. This experimentally obtained ring diameter is in good agreement with the calculated and simulated values.

4.8.2. Three-dimensional Annular Trapping of Microspheres and Biological Cells

Silica microspheres with 5 μm diameter (SS06N, Bangs Laboratories Inc., Fishers, IN) are used to evaluate the performance of the annular trap. A microsphere-water suspension is put into a 120- μm -thick chamber with a glass slide as the top and a No.1 cover-slip as the bottom. Sample container deeper than 200 mm is subject to convection flow due to laser heating, therefore the axial trapping stability of the annular trap is significantly reduced. The 120- μm -thick spacer is pre-punched with a 20-mm diameter hole in the center and adhesive on both sides (S-24736, Secure-Seal™ spacer, Invitrogen, Carlsbad, CA). The lateral trapping force is determined by moving the sample stage and measuring the stage's velocity once the trapped bead escapes, whereas the measurement of axial trapping force is carried out by adjusting the height of the microscope objective. Assuming spherical object symmetry and laminar fluid flow, the fluidic drag on an object is determined from the Navier-Stokes equation. At the escape velocity, v_e , the optical trapping force is equal to the fluidic drag force such that $F_{opt} = F_{drag} = 6\pi\eta r v_e$ ^{28,29}, where $\eta = 1 \times 10^{-3} \text{ N s m}^{-2}$ for water and r is the radius of the particle.

With an estimated average trapping power of 23 mW per micro-sphere, a lateral trapping force of 8.14 pN could be obtained, while the axial trapping force is at least 0.76 pN (higher trapping force is possible with a motor controlled smooth lifting of the objective). Figure 4-14 shows the 3-D trapping of 5 μm silica microspheres with 63 μ oil immersion objective (Plan-Apochromat, DIC, 63 μ NA=1.4, oil immersion,

Zeiss, Germany). Figure 4-14(a)-(b) corresponds to two different x-positions of the stage, demonstrating the confinement of particles along the circumference of the ring. Figure 4-14(c)-(d) depicts the lifting of the trapped particles while adjusting the z-position of the microscope objective.

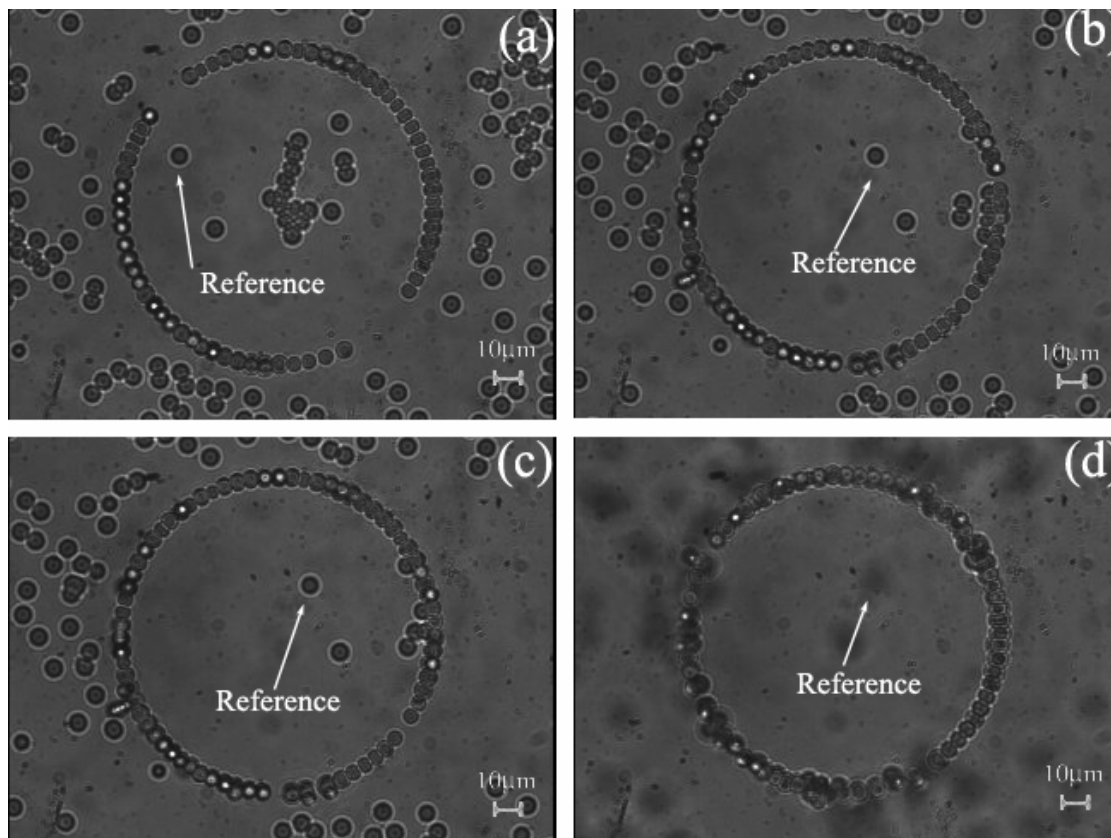


Figure 4-14: Sequences of video frames showing (a), (b) a ring of trapped 5 μm silica beads being moved in the transverse direction, and then (c), (d) being lifted 100 μm in the axial direction.

The geometrical structure of the ring trap can be experimentally shown by moving the objective in the axial direction. As shown in Figure 4-15(a), when the

image plane of the objective is $46\ \mu\text{m}$ above the center of the chamber, the ring focus is closer to the top of the chamber and particles in the center of the chamber are arranged into concentric rings due to the deviation from the ring focus. As the objective is lowered (Figure 4-15(b)), the ring focus is closer to the center of the chamber, and the concentric rings of particles have a smaller radial spacing. When the ring focus arrives at the center of the chamber, most of the particles are attracted to a single sharp ring (Figure 4-15(c)). Further reduction of the objective height makes concentric rings of particles appear again in the center of the chamber. The lower the objective, the larger the spacing becomes between the rings (Figure 4-15(d) and (e)). These observations agree with the simulation (ZEMAX, Bellevue, WA). In Figure 4-15(f) both the cross-section and the spot diagrams shows the localization of the sharp ring focus.

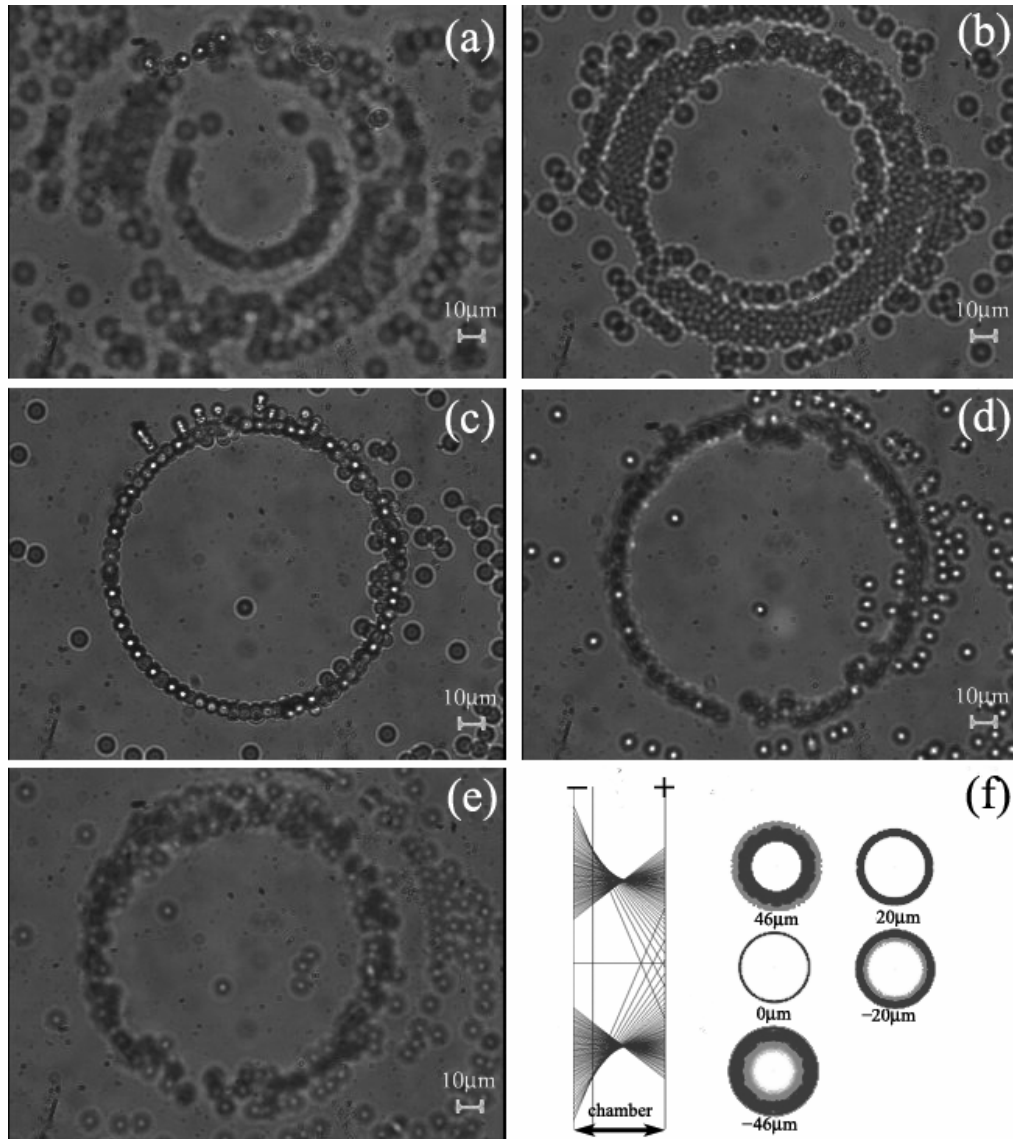


Figure 4-15: Geometrical structure of the annular trap: experiment and simulation. (a) objective height $z=46\ \mu\text{m}$, (b) $20\ \mu\text{m}$, (c) $0\ \mu\text{m}$, (d) $-20\ \mu\text{m}$, and (e) $-46\ \mu\text{m}$. (f) ZEMAX simulation. Left: the cross-section of light rays in the chamber when $z=0\ \mu\text{m}$; right: the spot diagrams at the center of the chamber when the objective is at different heights corresponding to (a)-(e).

Besides microspheres, biological cells can also be trapped in three dimensions.

Figure 4-16 shows a human sperm first swimming clockwise along the ring while the

stage is moved leftwards and then being lifted in the axial direction (the estimated average laser power is 25 mW).

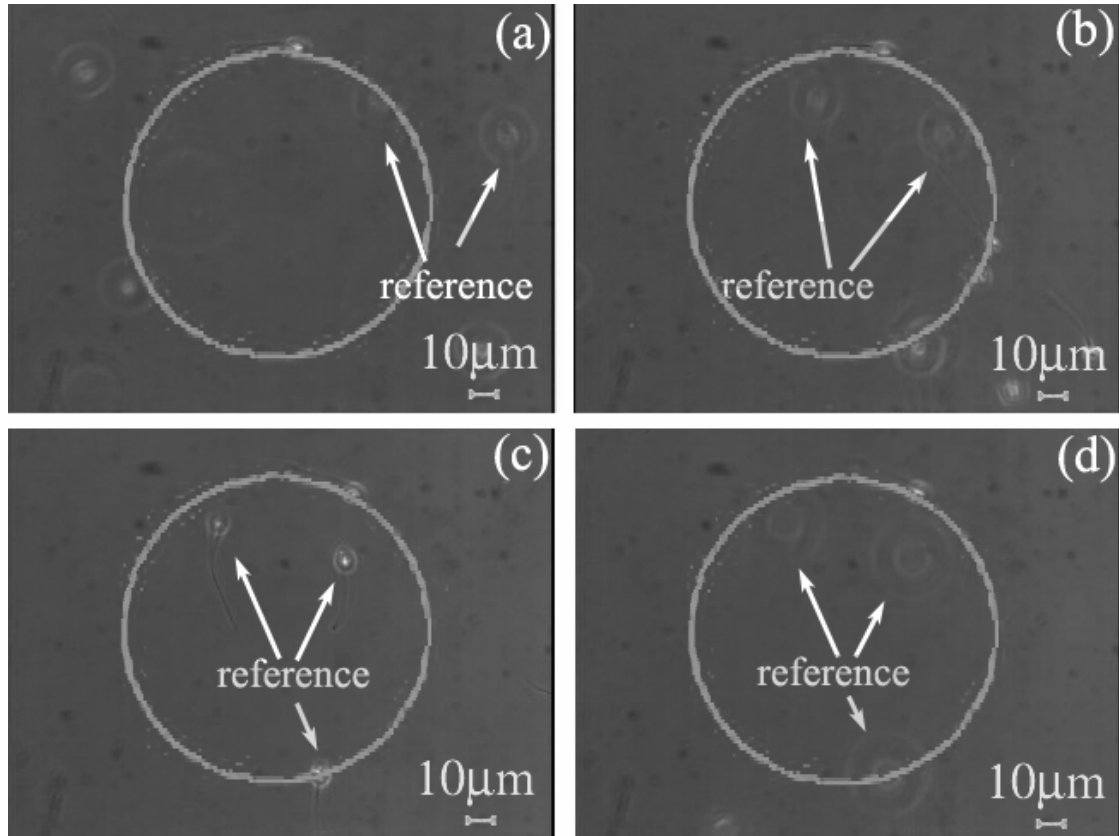


Figure 4-16: 3-D trapping of a human sperm. (a), (b) The trapped sperm near the top of the ring is moved in the transverse direction, and (c), (d) lifted in the axial direction.

4.9. Sperm Sorting and Analysis with the Annular Laser Trap

4.9.1. Specimen Preparation

Human sperm (IGO medical group, San Diego, CA) were collected from donors and cryopreserved (stored in liquid N₂ (77K)) according to a published protocol³⁰⁻³² until needed for experimentation. After being thawed in a pre-warmed water bath (37°C) for approximately 10 minutes, sperm are transferred to an Eppendorf centrifuge tube. A twice wash protocol was used to isolate the sperm^{33, 34}. The sample is centrifuged at 2000 rpm for 10 minutes (centrifuge tip radius is 8.23 cm). The supernatant is removed and the remaining sperm pellet is re-suspended in 1 milliliter of pre-warmed HTF (HEPES Buffered Human Tubal Fluid) with 5% SSS (Serum Substitute Supplement, Irvine Scientific, Santa Ana, CA). The process is repeated for a second time.

The specimen is loaded into a 120- μm -thick chamber with a glass slide as the top and a No.1 cover-slip as the bottom. The chamber is then mounted into a microscope stage holder and kept at room temperature during the experiment.

4.9.2. Sperm Sorting

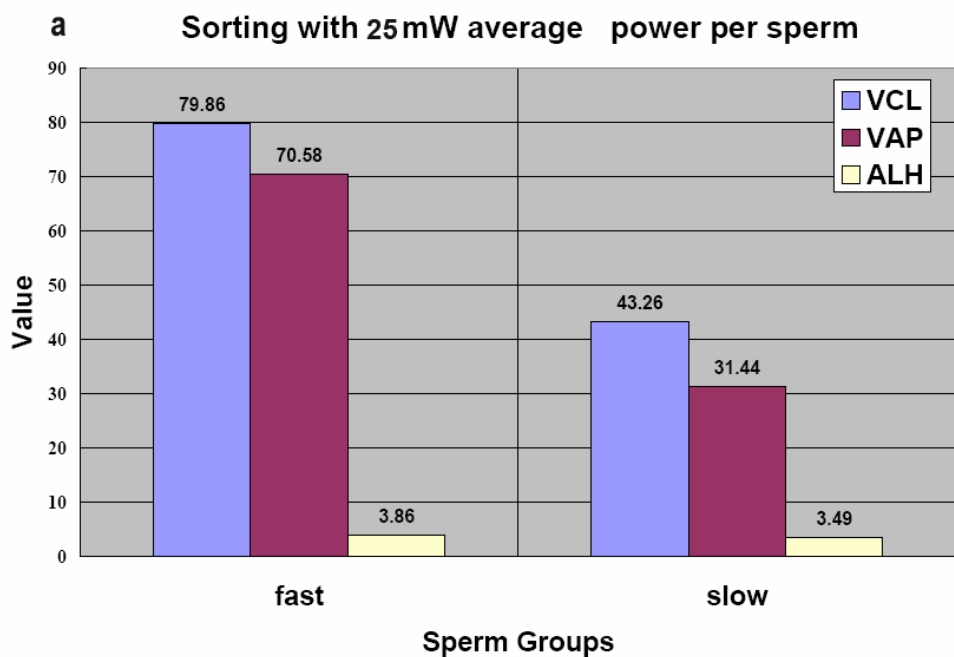
Sperm sorting with the annular trap according to their motility parameters (Table 4-1) is demonstrated. Curvilinear velocity (VCL, $\mu\text{m/s}$), smooth path velocity (VAP, $\mu\text{m/s}$)³⁵ and amplitude of lateral head displacement (ALH, μm) are measured using custom software that tracks the sperm³⁶.

Table 4-1: Motility parameters measured by sperm tracking program.

Parameter	Curvilinear velocity	Smooth path velocity	Amplitude of lateral head displacement
Abbreviation	VCL	VAP	ALH
Unit	$\mu\text{m/s}$	$\mu\text{m/s}$	μm
Definition	the total distance between adjacent points divided by the time elapsed	a smoothed path constructed by averaging several neighboring positions on the track and joining the averaged positions, which reduced the effect of lateral head displacement	the sperm head's lateral displacement from the mean path for every cycle of the cell's track

With an estimated laser power of 25 mW per sperm (total power in the specimen plane divided by the maximal number of sperm the ring could accommodate), the tested sperm could be classified into two groups according to their responses to the ring-shaped trap. The first group, or the “fast” group, is defined as sperm that swim through the ring with no detectable speed reduction. The second group, or the “slow” group, represents sperm whose swimming pattern is considerably affected by the ring, i.e., those that are slowed down, those that experience a temporary or permanent loss of motility, or those that change their swimming trajectory. As seen from Figure 4-17, the “fast” group has a much higher VCL and

VAP than the “slow” one, while their ALH are very close. The unpaired student T-test shows a p-value of $1.2\mu 10^{-15}$ for VCL, $1.2\mu 10^{-16}$ for VAP, and 0.3 for ALH, which means the “fast” group could be significantly differentiated from the “slow” group with a very high (>99.99%) confidence according to VAP or VCL, whereas ALH is a much less reliable way for discriminating between the two groups. Figure 4-18 is a video frame showing multiple sperm stopped by the ring.



b **Sorting Statistics at 25 mW average power per sperm**

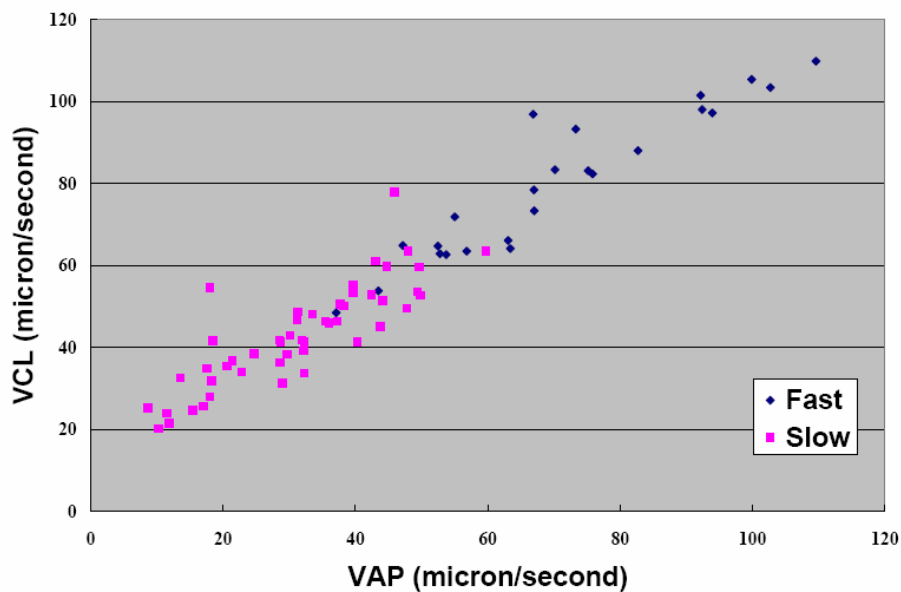


Figure 4-17: Parallel sperm sorting with annular laser trap when the estimated average laser power is 25 mW per sperm. (a) The mean value of VCL, VAP and ALH for “fast” and “slow” sperm from a population of 83 sperm. (b) The statistics VCL and VAP distribution of all the 83 sperm.

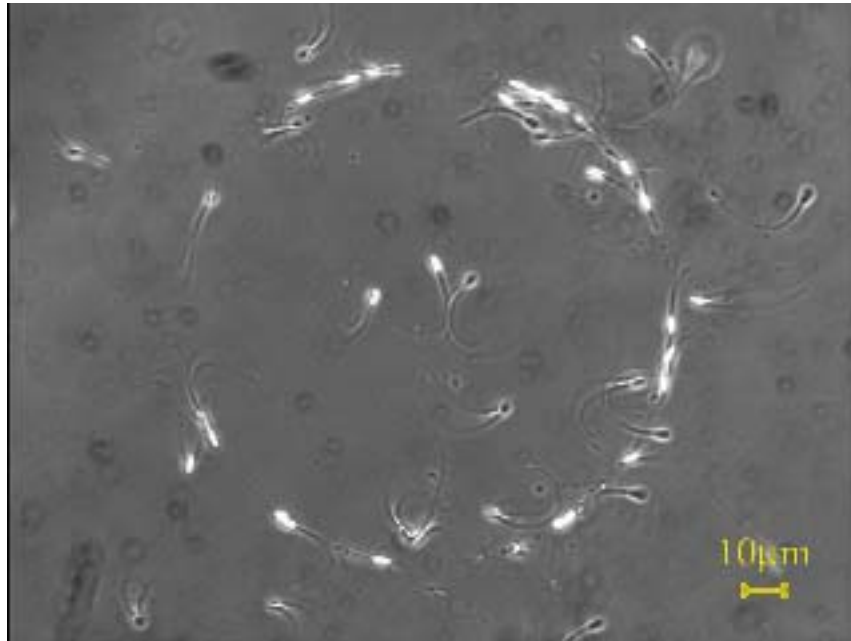


Figure 4-18: Tens of sperm are stopped along the ring focus.

4.9.3. Dynamic Monitoring of Sperm Swimming Behavior Change under Laser Trap

The effect of the annular laser trap on sperm motility is studied by making sperm swim along the curvature of the ring (Figure 4-19). Because of the optical properties of an axicon, the gradient force of the annular laser trap only exists in the radial direction. Trapped particles or self-propelled cells whose tangential movement is decoupled from their action in the radial direction are free to move along the circumference. However, for flagellated cells like sperm, their forward movement is induced by the viscous interactions of flagellum with the medium³⁷, a portion of which is along the lateral direction. Therefore, the radial confinement to a sperm that swims

along the ring should reduce its motility. To test this hypothesis, laser power is adjusted so that the swimming pattern of a sperm under different amounts of optical force and illumination is examined.

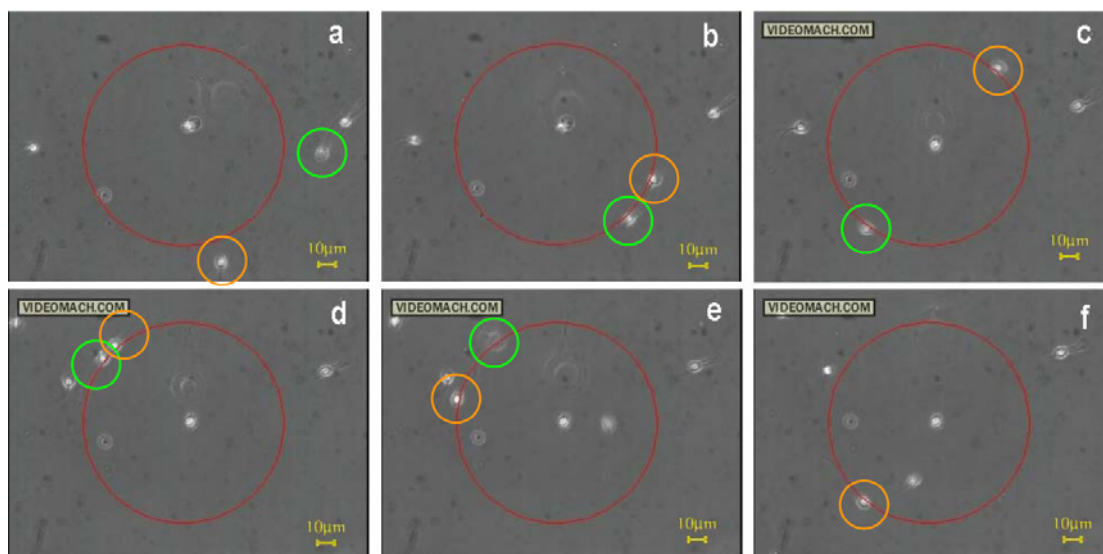


Figure 4-19: Guiding two sperm along the ring under an estimated average laser power of 25 mW per sperm. (a) Two sperm are freely swimming in opposite directions close to the ring (big red circle). (b) Affected by the optical gradient force from the ring trap, the two sperm start swimming along the curvature of the ring, one clockwise (green circle), the other counterclockwise (orange circle). (c) The two sperm continue swimming in opposite direction. (d) After swimming along the ring for about 180°, the two sperm are about to collide with each other. (e), (f) After collision, one sperm (green circle) is knocked out of the focus, while the other (orange circle) keep swimming along the ring.

Five types of observations are made, which are identified as “power binary”, “power gradient”, “fatigue”, “load” and “block”, respectively. In “power binary”, the laser is switched on and off so that the swimming parameters are measured for a sperm while it is propelling along the ring and after it is released from the trap. “Power

gradient” measures the change of sperm swimming pattern as a result of the decay of the laser power. “Fatigue” examines the slowing down of a sperm after it is guided along the ring under a fixed trapping power for an extended period of time. “Load” means a sperm is swimming along the ring while pushing an exterior object, such as a dead sperm or cell debris. Finally, “block” studies the behavior of a sperm while its forward movement is interrupted by an external obstacle.

A total of 93 sperm are measured, and for each sperm one or more types of observations are made. For the 64 observations of “power binary”, the percentages of sperm exhibiting a higher motility parameter while freely swimming are 79.33% for VAP, 75.69% for VCL, but only 42.66% for ALH. For the 92 occurrences of “power gradient”, most sperm experience increased VAP (76.03%) or VCL (73.97%) with decreased trapping power, while only 44.61% show an ALH increase with power decay. Among 9 observations of “fatigue”, with increased time (typically after 15~20 s along the ring), 80.95% have a reduced VAP, 76.19% have a reduced ALH, and 100% have a reduced VCL. Under the category of “load”, 100% of a total of 4 sperm exhibit a reduction of VAP and VCL, and 75% have a reduction of ALH. For the 2 sperm “blocked”, 100% show a decrease in VAP, VAL and ALH.

As one example of “power binary”, Figure 4-20 shows a repeatable reduction and recovery of VAP, VCL, and ALH as the sperm was swimming along and released from the ring trap. The average trapping power per sperm is switched between 25 mW and 0 mW. The amount of reduction and recovery are almost constant for VAP and VCL, while are less predictable for ALH.

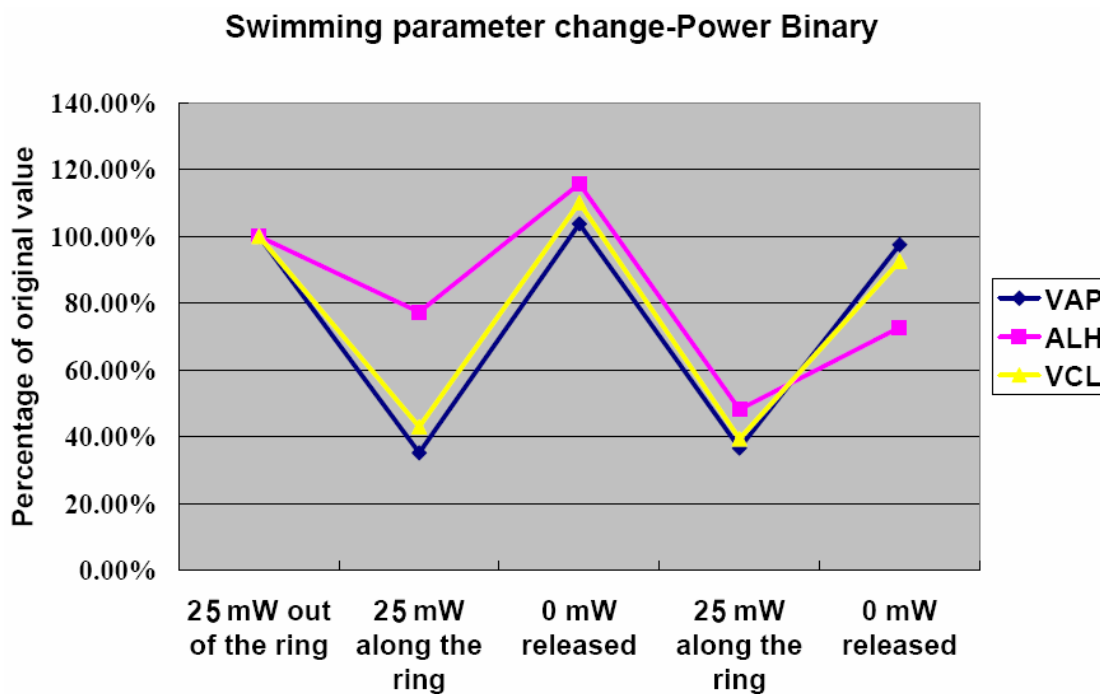


Figure 4-20: Swimming parameter change in an example of “power binary”, where a repeatable reduction/recovery of VAP, VCL, and ALH is observed as the sperm is swimming along/released from the ring trap.

Figure 4-21 presents the result from a “power gradient” experiment. For the tested sperm, VAP and VCL increases as a result of power decay, however, ALH fails to increase after the power was reduced to 11 mW.

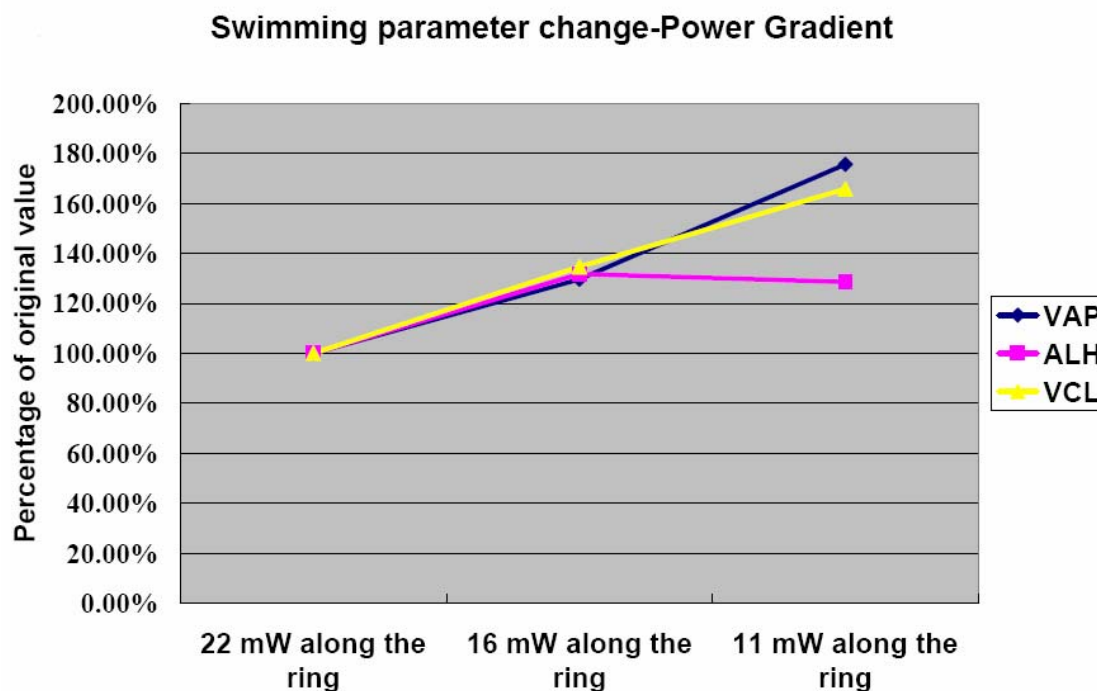


Figure 4-21: Swimming parameter change in an example of “power gradient”, where an increase of VAP and VCL is observed with a decrease of the trapping power.

As an example of “fatigue”, the sperm in Figure 4-22 experiences a decrease of VAP and VCL after swimming along the ring under an average laser power of 25 mW for more than 20 seconds. Nevertheless, when the laser is turned off, both VAP and VCL show a significant amount of recovery. Interestingly, the measured ALH shows an almost opposite trend with respect to the VAP and VCL.

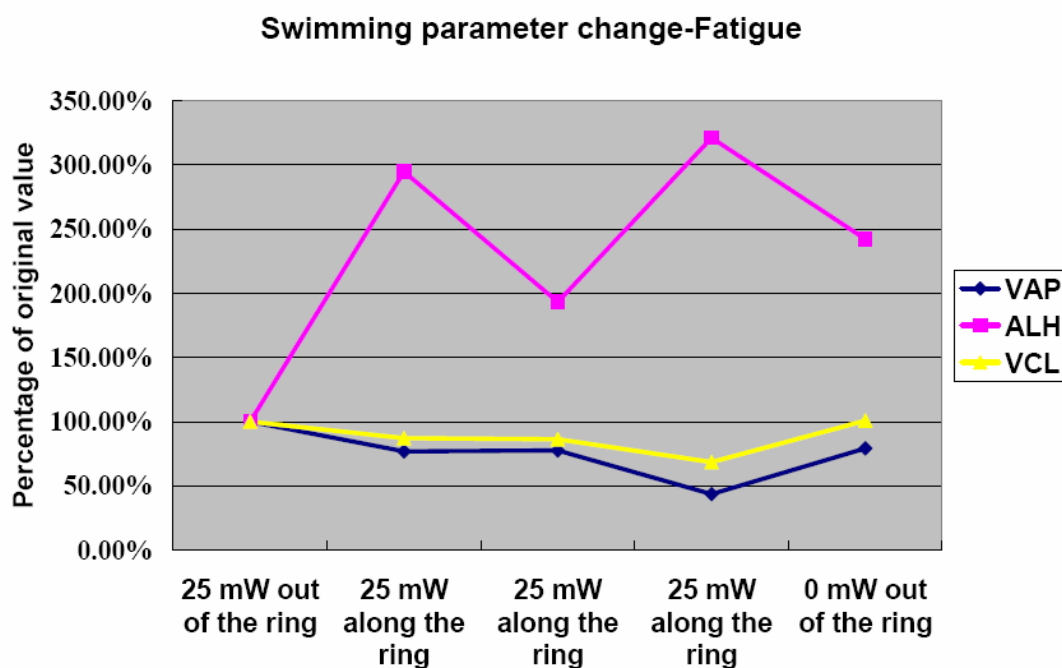


Figure 4-22: Swimming parameter change in an example of “fatigue”, where a decrease of VAP and VCL is observed after the sperm is swimming along the ring for more than 20 seconds. Both VAP and VCL increase after the sperm is released.

Figure 4-23 and Figure 4-24 illustrate the response of a sperm to an obstacle when its swimming path is confined by the ring trap. In each case, a sperm is swimming along the ring before encountering an obstacle (cell debris or dead sperm) trapped by the ring. Due to the radial confinement introduced by the ring trap, the sperm does not have enough energy to escape the ring and detour the obstacle. As a result, it tries to proceed by pushing the obstacle. For the case shown in Figure 4-23, the obstacle is light so that the sperm can push it and continue swimming along the ring with a lower VAP, VCL and ALH. When the trapping power is reduced from 25

mW to 20 mW per sperm, all three parameters increase. In Figure 4-24, the obstacle is heavy enough to stop the sperm from proceeding. The sperm is struggling with reduced VAP, VCL and ALH. As soon as the laser is turned off, the sperm picks up its velocity and lateral head displacement, bypasses the obstacle, and swims away. In Figure 4-25 and Figure 4-26, the video frames from experiments corresponding to the data in Figure 4-23 and Figure 4-24 are shown respectively.

Table 4-2 summarizes the measured motility parameter change corresponding to the five types of observations.

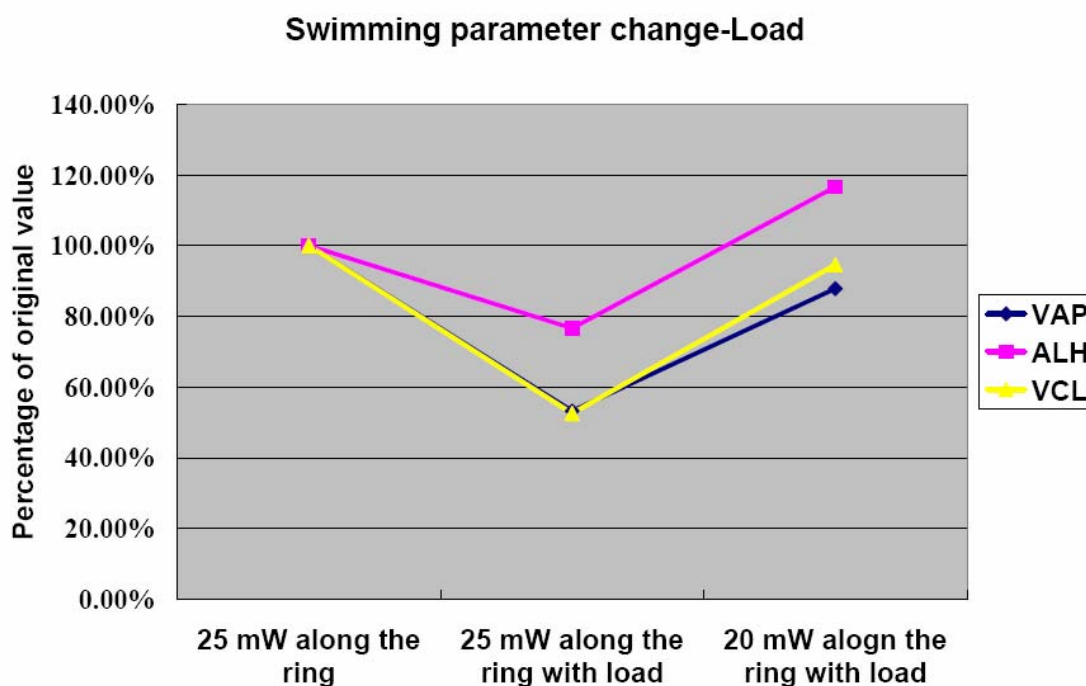


Figure 4-23: Swimming parameter change in an example of “load”, where a decrease of VAP, VCL and ALH is observed after the sperm starts pushing cell debris while swimming along the ring. All three parameters increase when the trapping power is decreased.

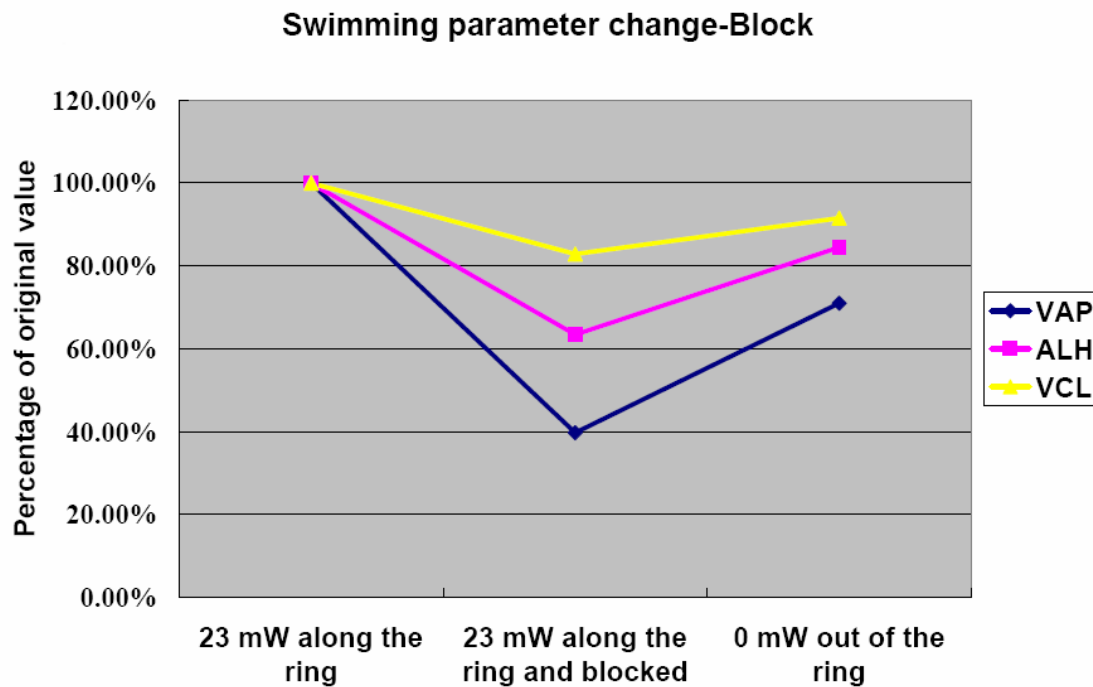


Figure 4-24: Swimming parameter change in an example of “block”, where a decrease of VAP, VCL and ALH is observed after the sperm’s forward movement along the ring is stopped by a dead sperm. All three parameters increase when the sperm is released.

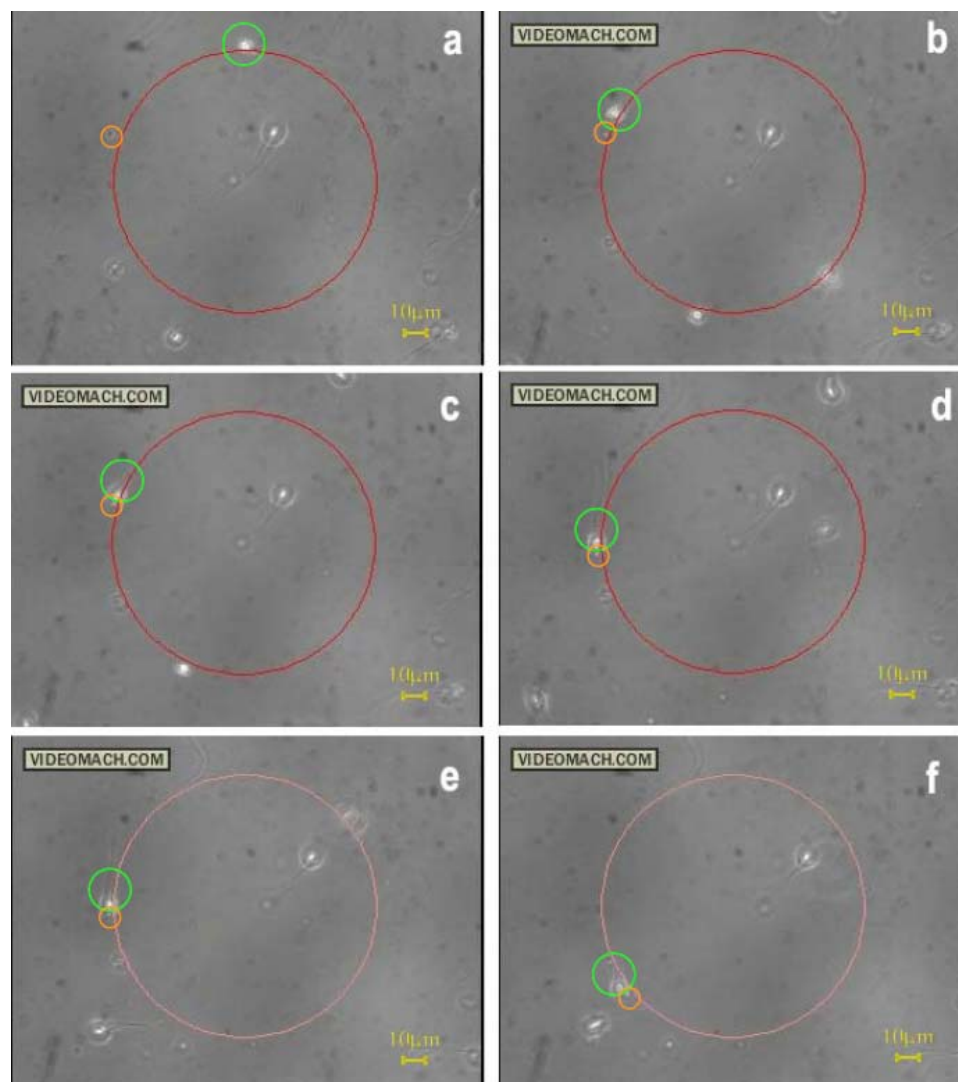


Figure 4-25: Sequences of images showing a sperm pushing cell debris while it is swimming along the ring trap. (a) Frame #8, under a laser power of 25 mW per sperm, a sperm (green circle) is swimming along the ring (big red circle) counterclockwise, while a cell debris is trapped by the ring (orange circle). (b) Frame #92, right before the sperm touches the debris. (c), (d) Frame #115 and #199, the sperm keep swimming along the ring by pushing the debris forward. (e), (f) Frame #385 and #469, the laser power is reduced to 20 mW per sperm, the sperm keep swimming along the ring with the load. The time interval between (a) and (b), (c) and (d), (e) and (f) are same, therefore the change of sperm swimming velocity could be clearly seen by examine the difference of circumferential displacement of the sperm, which is in agreement with Figure 4-22.

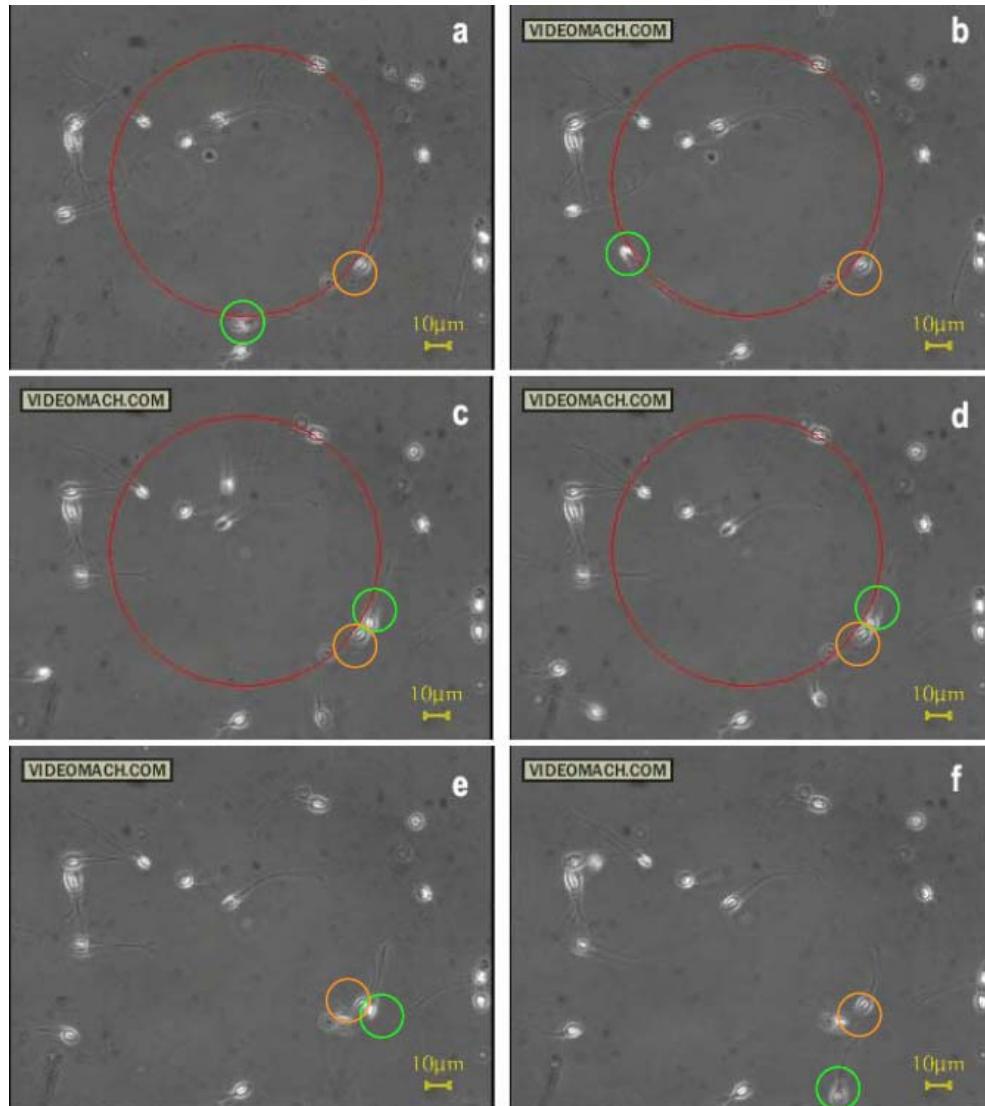


Figure 4-26: Sequences of images showing a sperm blocked by a dead sperm while it is swimming along the ring trap. (a), (b) Frame #1 and #51, under a laser power of 23 mW per sperm, a sperm (green circle) is swimming along the ring (big red circle) clockwise. A dead sperm stuck to the glass is on the ring (orange circle). (c), (d) Frame #325 and #375, the sperm encounters the dead sperm and could not keep moving forward. (e), (f) Frame #425 and #475, after the laser is turned off, the sperm changes its head orientation, bypasses the dead sperm and swims away. The time interval between (a) and (b), (c) and (d), (e) and (f) are same, therefore the change of sperm swimming velocity could be clearly seen by examine the difference of circumferential displacement of the sperm, which is in agreement with Figure 4-23.

Table 4-2: Percentage of tested sperm showing responses consistent with expectation (decreased motility when being trapped at a higher laser power, for a longer period, or affected by an external object).

	Power Binary	Power Gradient	Fatigue	Load	Block
VAP	79.33%	76.03%	80.95%	100.00%	100.00%
ALH	42.66%	44.61%	76.19%	75.00%	100.00%
VCL	75.69%	73.97%	100.00%	100.00%	100.00%

4.10. Experiments with Resizable Annular Laser Trap

4.10.1. Experimental Setup

As discussed in section 4.6, by adding two additional axicons in between the focusing lens and the tube lens, and translating one of the axicons along the optical axis, the diameter of the ring-shaped trap could be dynamically adjusted. The scheme and the photo of the dynamically resizable annular trapping system are shown in Figure 4-27 and Figure 4-28, respectively.

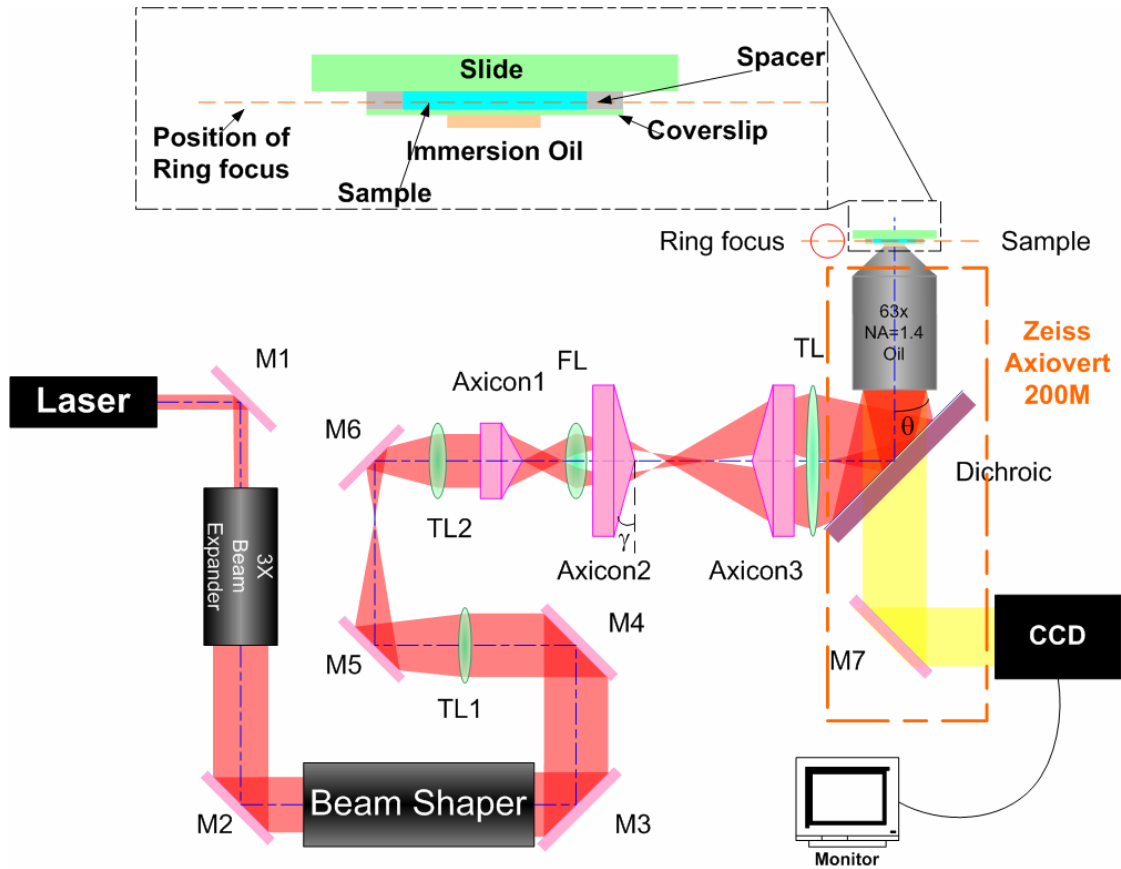


Figure 4-27: Experimental setup of the dynamically adjustable annular laser trap. M1-M7---Mirrors, TL1---Telescope lens 1, TL2---Telescope lens 2, FL---focusing lens, TL---Tube lens.

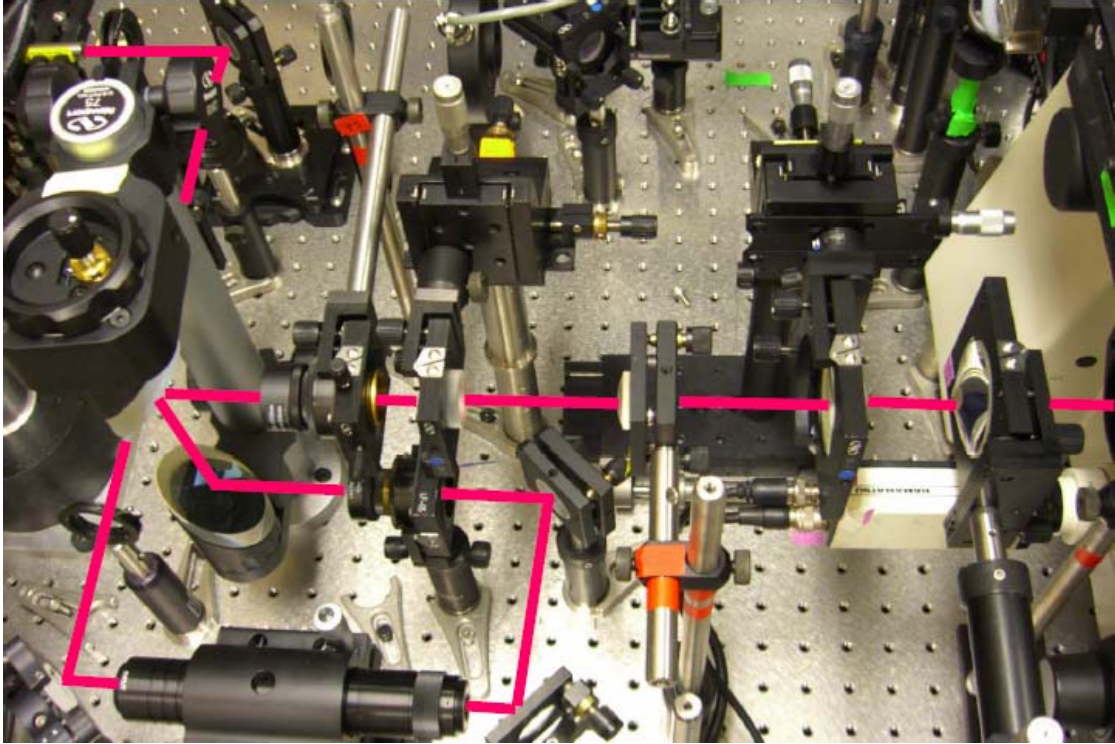


Figure 4-28: Photo of the dynamically adjustable annular laser trapping system.

4.10.2. Experimental Result

The size tunability of the annular trap is demonstrated with $5\ \mu\text{m}$ microspheres. Figure 4-29 shows that by moving Axicon 2 an additional 10mm away from Axicon 3, the diameter of the ring trap increased from $70\ \mu\text{m}$ (Figure 4-29(a), (c)) to $140\ \mu\text{m}$ (Figure 4-29(b), (d)). This endures the system the flexibility on trapping a wide variety of particles, with different sizes and makes it easy to adjust the throughput.

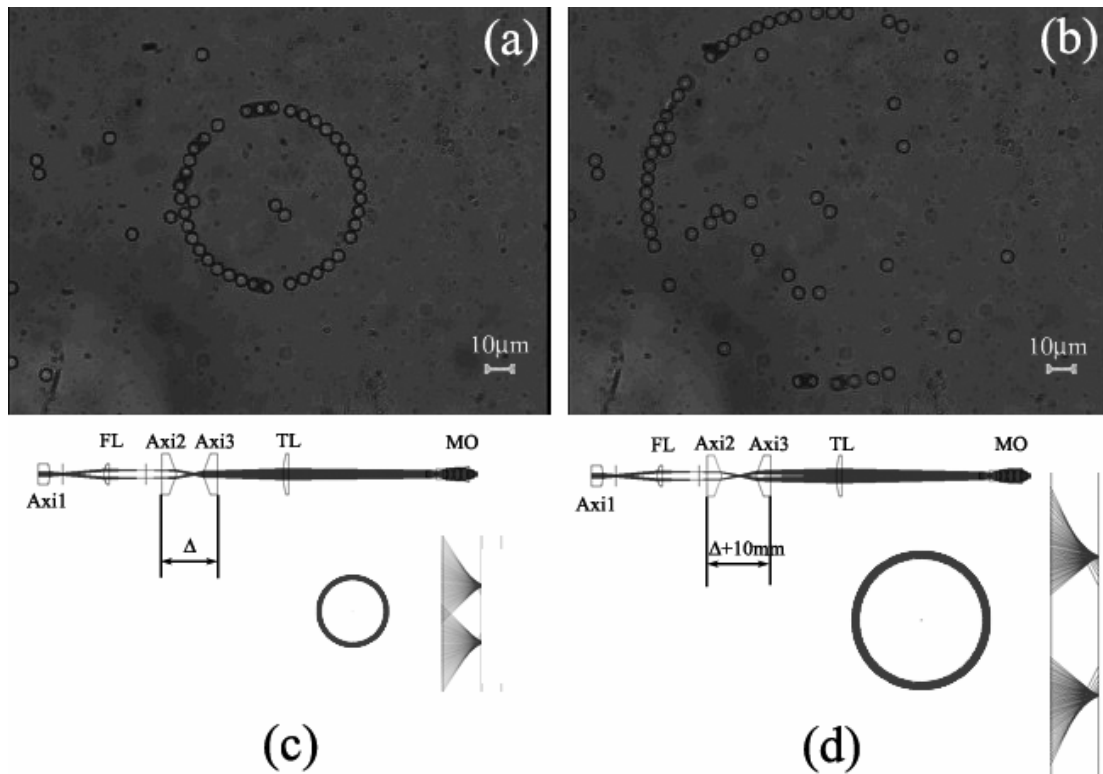


Figure 4-29: Size tunability. (a) At original axial position of Axicon 2, the diameter of the ring trap is 70 μm . (b) When Axicon 2 is shifted to the left for 10 mm, the ring diameter increases to 140 μm . (c), (d) ZEMAX simulated layout, focus close-up, and sample plane spot diagram for (a) and (b). Axi1---Axicon 1; Axi2---Axicon 2; Axi3---Axicon 3; FL---Focusing Lens; TL---Tube Lens; MO---Microscope Objective.

4.11. Discussion

According to the almost linear relationship between laser trapping power and sperm motility,^{15, 16} with the demonstrated sorting ability of the annular laser trap under a specific power, and the resizability of the annular laser trap (section 4.10), it is possible to adjust the average trapping power per sperm under a fixed total input power so that different thresholds are used for multi-level sorting.

In the current study, the sperm in the chamber swim in random directions. This condition could be changed by introducing a chemo-attractant to the center of the ring trap. Due to chemotaxis, a critical feature of sperm in response to the diffusion gradient of chemicals released by the egg and surrounding cells of the cumulus oophorus, sperm should start approaching to the chemo-attractant from all directions. As a result, the annular trap could be used to sort sperm according to their chemotactic response.

4.12. Conclusions

This chapter presented a new type of axicon trapping that allows for parallel 3-D manipulation of micro-particles. The special optical properties of axicons are used to create a continuous, size tunable annular trap with high power efficiency and constant numerical aperture. Experiments with microspheres and biological cells have proved the performance of the annular traps and their applicability to both inorganic and organic micro-particles.

Aiming at motility and biotropism studies on self-propelled cells, parallel sperm sorting with the annular laser trap is demonstrated. Under a specific laser power, two groups of sperm could be significantly differentiated ($p < 0.05$) based on their VAP or VCL. By confining a sperm's swimming along the ring, the impacts of external transverse force (magnitude — “power binary” and “power gradient”, applying period — “fatigue”) and obstacles (“load” and “block”) on sperm motility were studied. While most sperm experience degradations in VAP and VCL under a larger laser dose or a longer period of transverse force, the relationship between ALH

and transverse force has not been clarified. The observation of “fatigue” after 20 s is in agreement with previous research using single spot laser trap¹⁶.

In conclusion, the annular laser trap provides the possibility of multi-level, high-throughput sperm sorting based on motility and chemotaxis. With only tens of milliwatts devoted to each sperm, this new type of laser trap offers a more gentle approach to sperm analysis and laser-sperm interaction study. The strong optical gradient in the radial direction and the zero gradient force in the circumferential direction make it possible for sperm to swim along the ring without having to stop. The unique geometrical feature of the “ring” also provides a way to confine a swimming cell in the field of view for an extended period of time without having to deal with sharp turns or changes in swimming curvature. As a result, the effect of optical force, laser radiation and external obstacles on sperm swimming pattern and membrane potential (with the aid of specific fluorescence probes) could be investigated in more detail. The application could be extended to motility and biotropy studies of other self-propelled cells, such as algae and bacteria.

4.13. Acknowledgements

Jaclyn Nascimento is acknowledged for her collaboration on the experiments performed in this chapter along with co-authoring the publications that resulted from this research.

Dr. Elliot Botvinick, Dr. Mihrimah Ozkan, Dr. Michael Berns and Dr. Sadik Esener are acknowledged for their innovative ideas concerning this research.

Dr. Linda Shi is acknowledged for her software support with Labview programs.

We would like to thank IGO Medical Group for providing human semen samples.

Lastly, we would like to acknowledge the Scripps Institute of Oceanography, and the Beckman Laser Institute Inc. foundation for funding this research.

Sections 4.5, 4.6, and 4.7 of this chapter, in part, are a reprint of material as it appears in "Dynamically adjustable annular laser trapping based on axicons," by B. Shao, J. M. Nascimento, E. L. Botvinick, M. W. Berns, S. C. Esener, *Applied Optics*, in press, 2006.

Sections 4.5, 4.6, and 4.7 of this chapter, in part, are a reprint of material as it appears in "Axicon-based annular laser trap for sperm activity and chemotaxis study," by B. Shao, J. M. Vinson, E. L. Botvinick, S. C. Esener, M. W. Berns, Proceedings of the SPIE, v5930, 0D, SPIE 50th Annual Meeting, San Diego, California, USA, Jul. 31-Aug. 4, 2005.

4.14. References

1. M. Ozkan, M. M. Wang, C. Ozkan, R. A. Flynn, and S. Esener, "Optical manipulation of objects and biological cells in microfluidic devices," *Biomedical Microdevices* **5**, 47-54 (2003).
2. B. Shao, S. Zlatanovic, and S. C. Esener, "Microscope-integrated micromanipulation based on multiple VCSEL traps," presented at the Optical Trapping and Optical Manipulation, Denver, Colorado, 2004.
3. R. A. Flynn, A. L. Birkbeck, M. Gross, M. Ozkan, B. Shao, M. M. Wang, and S. C. Esener, "Parallel transport of biological cells using individually

- addressable VCSEL arrays as optical tweezers," *Sensors and Actuators, B, Chem* **87**, 239-243 (2002).
4. A. L. Birkbeck, R. A. Flynn, M. Ozkan, D. Song, M. Gross, and S.C. Esener, "VCSEL arrays as micromanipulators in chip-based biosystems," *Biomedical Microdevices* **5**(1), 47-54 (2003).
 5. M. W. Berns, "Laser scissors and tweezers," *Scientific American (International Edition)* **278**, 52-57 (1998).
 6. A. H. Forster, M. M. Wang, W. F. Butler, M. Chachisvilis, T. D. Y. Chung, S. C. Esener, J. M. Hall, O. Kibar, K. Lykstad, P. J. Marchand, E. M. Mercer, L. M. Pestana, S. Sur, E. Tu, R. Yang, H. Zhang, and I. Kariv, "Use of moving optical gradient Wells for analysis of apoptotic cellular responses in a chronic myeloid leukemia cell model," *Analytical Biochemistry* **327**, 14-22 (2004).
 7. D. A. B. Durrant, A. Anderson and M. Ann Olson, "Effect of extraction methods on cryopreservation of canine epididymal sperm," presented at the SSR 33rd Annual Meeting, Madison, WI, USA, July 15-18, 2000, 2000.
 8. H. Schmidt and G. Kamp, "Induced hyperactivity in boar spermatozoa and its evaluation by computer-assisted sperm analysis," *Reproduction* **128**, 171-179 (2004).
 9. J. Baumber and S. A. Meyers, "Hyperactivated Motility in Rhesus Macaque (*Macaca mulatta*) Spermatozoa," *J. Andrology* **27**(3), 459-468 (2006).
 10. K. Konig, L. Svaasand, Y. Liu, G. Sonek, P. Patrizio, Y. Tadir, M. W. Berns, and B. J. Tromberg, "Determination of motility forces of human spermatozoa using an 800 nm optical trap," *Cell Mol. Biol. (Noisy-le-grand)* **42**(4), 501-509 (1996).
 11. J. E. Araujo, Y. Tadir, P. Patrizio, T. Ord, S. Silber, M. W. Berns, and R. H. Asch, "Relative force of human epididymal sperm," *Fertil. Steril.* **62**(3), 585-590 (1994).
 12. E. A. Z. N. Dantas, Jr., Y. Tadir, M. W. Berns, M. J. Schell, S. C. Stone, "Effect of freezing on the relative escape force of sperm as measured by a laser optical trap," *Fertil. Steril.* **63**, 185-188 (1995).
 13. Y. L. P. Patrizio, G. J. Sonek, M. W. Berns, and Y. Tadir, "Effect of pentoxifylline on the intrinsic swimming forces of human sperm assessed by optical tweezers," *J. Andrology* **21**, 753-756 (2000).
 14. W. H. W. Y. Tadir, O. Vafa, T. Ord, R. H. Asch, M. W. Berns, "Micromanipulation of sperm by laser generated optical trap," *Fertil. Steril.* **52**, 870-873 (1989).

15. W. H. W. Y. Tadir, O. Vafa, T. Ord, R. H. Asch, M. W. Berns, "Force generated by human sperm correlated to velocity and determined using a laser generated optical trap," *Fertil. Steril.* **53**, 944-947 (1990).
16. J. M. Nascimento, E. L. Botvinick, L. Z. Shi, B. Durrant, and M. W. Berns, "Analysis of sperm motility using optical tweezers," in *Journal of Biomedical Optics*, (2006).
17. M. Eisenbach and I. Tur-Kaspa, "Do human eggs attract spermatozoa?," *BioEssays* **21**, 203-210 (1999).
18. J. H. McLeod, "The axicon: A new type of optical element," *J. Opt. Soc. Am.* **44**, 592-597 (1954).
19. J. H. McLeod, "Axicons and their uses," *J. Opt. Soc. Am.* **50**, 166-169 (1960).
20. Z. Ding, H. Ren, Y. Zhao, J. S. Nelson, and Z. Chen, "High-resolution optical coherence tomography over a large depth range with an axicon lens," *Optics Letters* **27**(4), 243-245 (2002).
21. R. T. M. Rious, and P. A. Belanger, "Linear, annular, and radial focusing with axicons and applications to laser machining," *Applied Optics* **17**(10), 1532-1536 (1978).
22. Q. Ren and R. Birngruber, "Axicon: a new laser beam delivery system for corneal surgery," *IEEE JOurnal of Quantum Electron* **26**, 2305-2308 (1990).
23. Y. B. O. I. Manek, R. Grimm, "Generation of a hollow laser beam for atom trapping," *Optics Communications* **147**, 67-70 (1998).
24. V. I. Balykin, V. S. Letokhov, V. G. Minogin, Y. V. Rozbdestvenskyt, and A. L. Sidorov, "Radiative collimation of atomic beams through two-dimensional cooling of atoms by laser-radiation pressure," *J. Opt. Soc. Am. B* **2**, 1776-1783 (1985).
25. Retrieved <http://www.physik.uni-regensburg.de/forschung/maier/bessel/basis/axicon.gif>.
26. V. G.-C. J. Arlt, W. Sibbett, K. Dholakia, "Optical micromanipulation using a Bessel light beam," *Optics Communications* **197**, 239-245 (2001).
27. E. L. B. J. M. Vinson, B. Durrant, and M. W. Berns, "Correlation of sperms' swimming force to their swimming speed assessed by optical tweezers," presented at the Optical Trapping and Optical Micromanipulation II, San Diego, CA, USA, 2005.

28. G. K. Batchelor, *An Introduction to Fluid Dynamics* (Cambridge University Press, Cambridge, 1991).
29. S. R. B. S.P. Smith, A.L. Brody, B.L. Brown, E.K. Boyda, M. Prentiss, "Inexpensive optical tweezers for undergraduate laboratories," *Am. J. Phys.* **67**(1), 26-35 (1999).
30. S. DiMarzo, J. Huang, J. Kennedy, B. Villanueva, S. Hebert, and P. Young, "Pregnancy rates with fresh versus computer-controlled cryopreserved semen for artificial insemination by donor in a private practice setting," *Am. J. Obstet. Gynecol.* **162**(6), 1483-1490 (1990).
31. T. E. C. o. t. A. F. Society, "New Guidelines for the use of semen donor insemination," *Fertil. Steril.* **53**(3 Suppl 1), 1S-12S (1990).
32. P. Serfini and R. P. Marrs, "Computerized staged-freezing technique improves sperm survival and preserves penetration of zona-free hamster ova," *Fertil. Steril.* **45**(6), 854-858 (1986).
33. S. DiMarzo and J. Rakoff, "Intrauterine insemination with husband's washed sperm," *Fertil Steril.* **46**(3), 470-475 (1986).
34. R. C. Toffle, T. C. Nagel, G. E. Tagatz, S. A. Phanse, T. Okagaki, and C. A. Warrin, "Intrauterine insemination: The University of Minnesota Experience," *Fertil. Steril.* **43**(5), 743-747 (1985).
35. M. Katebi, M. Movahedin, M. A. Abdolvahabi, M. Akbari, F. Abolhassani, A. Sobhani, and F. Aoki, "Changes in Motility Parameters of Mouse Spermatozoa in Response to Different Doses of Progesterone during Course of Hyperactivation," *Iranian Biomedical Journal* **9**(2), 73-79 (2005).
36. Z. Shi, E. L. Botvinick, and M. W. Berns, "Real-time Single Sperm Tracking and Laser Trapping: "Track and Trap"," presented at the Cell Motility III: The American Society for Cell Biology, San Francisco, 2005.
37. G. Taylor, "Analysis of the swimming of microscopic organisms," *Proc R Soc Lond A* **209**, 447-461 (1951).

5. Microscope-Integrated Micromanipulator Based on Multiple VCSEL Traps

This chapter demonstrates a microscope-integrated vertical cavity surface emitting laser (VCSEL) array trapping system capable of independent control, rotation, and batch processing of biological cells. In this system, a single VCSEL trap serves as a collector and distributor, while an array of VCSEL traps functions like a chip, enabling parallel processing of multiple objects. The trapping system here differs from earlier VCSEL tweezers setups in several ways, including (1) the optical traps are mobile with the addition of a static sample holder and (2) both a single and an array of optical traps can be controlled independently by tilting mirrors at the conjugate planes of the objective back aperture, and their relative depth can be adjusted without losing trapping power. These enhancements provide an advantage for lab-on-a-chip devices that contain microfluidics and offer more flexibility in multi-target manipulation.

The main contributions of this research are the design of a 2-D agile VCSEL tweezers array with negligible power clipping regardless of the dimension of the VCSEL array, and the collaboration of the independently-controlled single VCSEL trap and VCSEL trap array for multi-step operation on biological cells.

5.1 Background and Motivations

Optical trapping was first introduced in 1970 by Ashkin as a purely physical phenomenon of radiation pressure on micron-sized particles.¹ Since its discovery in 1986,² optical tweezers --- single beam optical trappings have been widely investigated as a noninvasive manipulation technique for microparticles, such as biological cells and microspheres. Experimentally, the use of laser traps has not been limited to the precise manipulation of living cells and organelles within cells,³⁻⁵ but also has been recently expanded to exploring the functions and forces applied by molecular motors on biomolecules such as DNA and RNA.⁶ However, integration of optical tweezers as a scientific tool for biochip technologies has been considerably delayed due to the prohibitive cost of conventional lasers and the large system volume they occupy. Vertical Cavity Surface Emitting Lasers (VCSELs) provide a solution to this problem in that they are semiconductor microlaser diodes that emit light vertically from the surface and can be fabricated in 2-D arrays efficiently on a 3-inch wafer using standard microelectronic fabrication methods. Substituting VCSELs and VCSEL arrays for standard diode and gas lasers provides the ability to meet the demands of current biochip and lab-on-a-chip technologies, which require that the controlling devices be small and have the ability of being replicated in large arrays, so that multiple, simultaneous experiments can be performed in parallel and at a low cost.

Previously, optical trapping and active manipulation of live biological cells and microspheres based on VCSEL array have been demonstrated by fixing the laser trap and moving the sample plane with a translation stage.^{7,8} However, when microfluidic

channel systems (lab-on-a-chip devices) come into play, the background flow introduces complexity and uncertainty in the velocity and forces on microparticles. Therefore the capability of transporting microparticles without moving the sample container becomes necessary. At the same time, independent control of multiple optical traps is highly desirable to obtain more flexibility in micro-object manipulation.

To utilize optical tweezers in biological applications, lasers with wavelength ranges from 800 nm to 1100 nm are preferred because of the low absorption by living specimens and the surrounding buffer solution. To extrapolate further on optical wavelength absorption, research on cell viability shows that cellular stress and photodamage are minimal in the range of 800-850 nm,⁹⁻¹² which includes the wavelength of the VCSELs (850 nm). Since the maximal optical output power of a present VCSEL is fairly low (~5 mW), and the relative refractive index of biological cells in the buffer medium is small (~1.05), the available optical force is relatively weak (<5pN). Fortunately, the Laguerre-Gaussian mode output from the VCSEL helps since the highest intensity is located at the outer ring of the optical aperture, resulting in a stronger 3-D optical confinement at a lower power level.¹³

As a precision optical instrument, a microscope has stable and well-aligned internal optics and multiple I/O ports for simultaneous access. Integrating optical tweezers into a microscope takes advantage of all those features, and provides a compact and robust laser-manipulating system with space for functional upgrade, such as fluorescence study. According to the mounting direction of the objective lens, various configurations are available for optical tweezers. For the inverted structure

used in our research, the laser beam enters the objective vertically from the downside, therefore the scattering force generated by photon momentum transfer is upwards. This counteraction of gravity and scattering force releases the requirement on the numerical aperture (NA) of the objective lens for 3-D trapping and alleviates the adhesion between samples and the slide, making particle manipulation easier.

5.2 Effect of beam symmetry and power clipping on laser trapping performance

To build an independently controlled multiple laser tweezers system, one needs to first create a single agile (movable) laser trap, then combine two or more such laser traps and make their operation uncorrelated. Generally, agile laser tweezers can be realized in three ways: (1) intensity adjustment between adjacent VCSELs in an array,¹⁴ (2) dynamic holography,¹⁵ and (3) beam deflection.^{16, 17} Intra-VCSEL array movement is not suitable for long distance continuous transportation due to the limitations in resolution and pitch of current VCSEL arrays. Dynamic holography has advantages in complex trapping patterns, especially for large, real time trapping arrays, but needs high computation volume and suffers from low efficiency and speed. Among beam deflectors, electrooptical deflectors (EOD) and acoustooptical deflectors (AOD) are cumbersome to be extended to 2-D applications and have relatively small tilting ranges ($\pm 0.6^\circ$). Based on factors such as speed, moving range, accuracy, stability, complexity, cost and system arrangement flexibility, tilting mirrors are chosen to realize the agile laser tweezers in our system¹⁸.

For a mobile laser trap, it is important to make sure that during its displacement from the origin, its performance degradation is within tolerance, i.e. the laser trap can work efficiently in a large enough spatial range to allow the required object manipulation. Best trapping performance is obtained when the largest NA, highest optical power, and symmetrical trapping beam are used. To satisfy the first requirement, the incoming laser beam should completely fill the back aperture of the microscope objective. In order to maintain symmetry of the beam regardless of the motion of trap, the laser beam should always pass through the effective back focal plane of objective. Because the effective back focal plane and the back aperture of a microscope objective do not coincide with each other, it is impossible to make incident beam pivot around the two planes simultaneously, which means, the two conditions cannot be satisfied at the same time when the incident angle changes (Figure 5-1). A small NA implies a low convergence angle of light, which results in a weak lateral force⁸ and leads to unstable trapping, whereas power clipping at the back aperture of the microscope objective decreases the NA and reduces the effective incident power as well. Accordingly, it is essential to study the effects of beam symmetry and power clipping on trapping performance and use the result as the guide for system design.

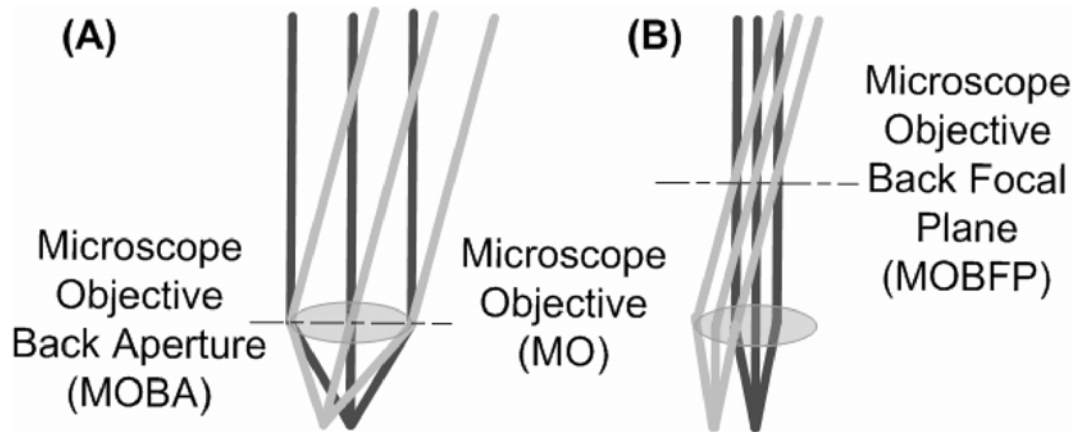


Figure 5-1: The back aperture and back focal plane of a microscope objective in optical trapping. (A) Trapping beam pivots around the back aperture to maximize the NA while beam symmetry cannot be maintained. (B) Trapping beam pivots around the back focal plane to maintain beam symmetry while the effective NA is considerably reduced.

Evaluation experiments are conducted with a finite microscope objective, but the results could also be applied for an infinity-corrected microscope objective. Power throughput is determined by dual-objective coupling, i.e. the laser coming out of the first microscope objective used for trapping is coupled into the other objective with the same parameters and the power out of the back aperture of the second objective is measured by a photodetector.

As shown in Figure 5-2(a), a laser beam of Laguerre-Gaussian mode from VCSEL (Honeywell EM., Santa Clara, CA, 850 nm) is collimated by lens L_1 and then focused by lens L_2 on a tilting mirror placed at a distance equal to 160 mm from the microscope objective (Edmund Scientific, 100 μ , NA1.25, oil immersion) back aperture. Initially, the incident beam completely fills the back aperture, and the trapping beam is under optimal conditions. When the mirror is tilted, power clipping is

introduced at the back aperture, consequently the effective NA is reduced and only a portion of the incoming power enters the microscope objective for trapping. At the same time, the trapping beam out of the objective becomes asymmetric. With the increase of the tilting angle, the power throughput (ratio between power out of microscope objective and power out of VCSEL) decreases, and strong trapping only exists near normal incidence where there is no power clipping. The variation of trapping power vs. tilting angle is shown in Figure 5-2(b), and the region of effective trapping is marked by dashed lines. The asymmetric power distribution in Figure 5-2(b) is due to the nonuniformity of beam profile at the trapping spot.

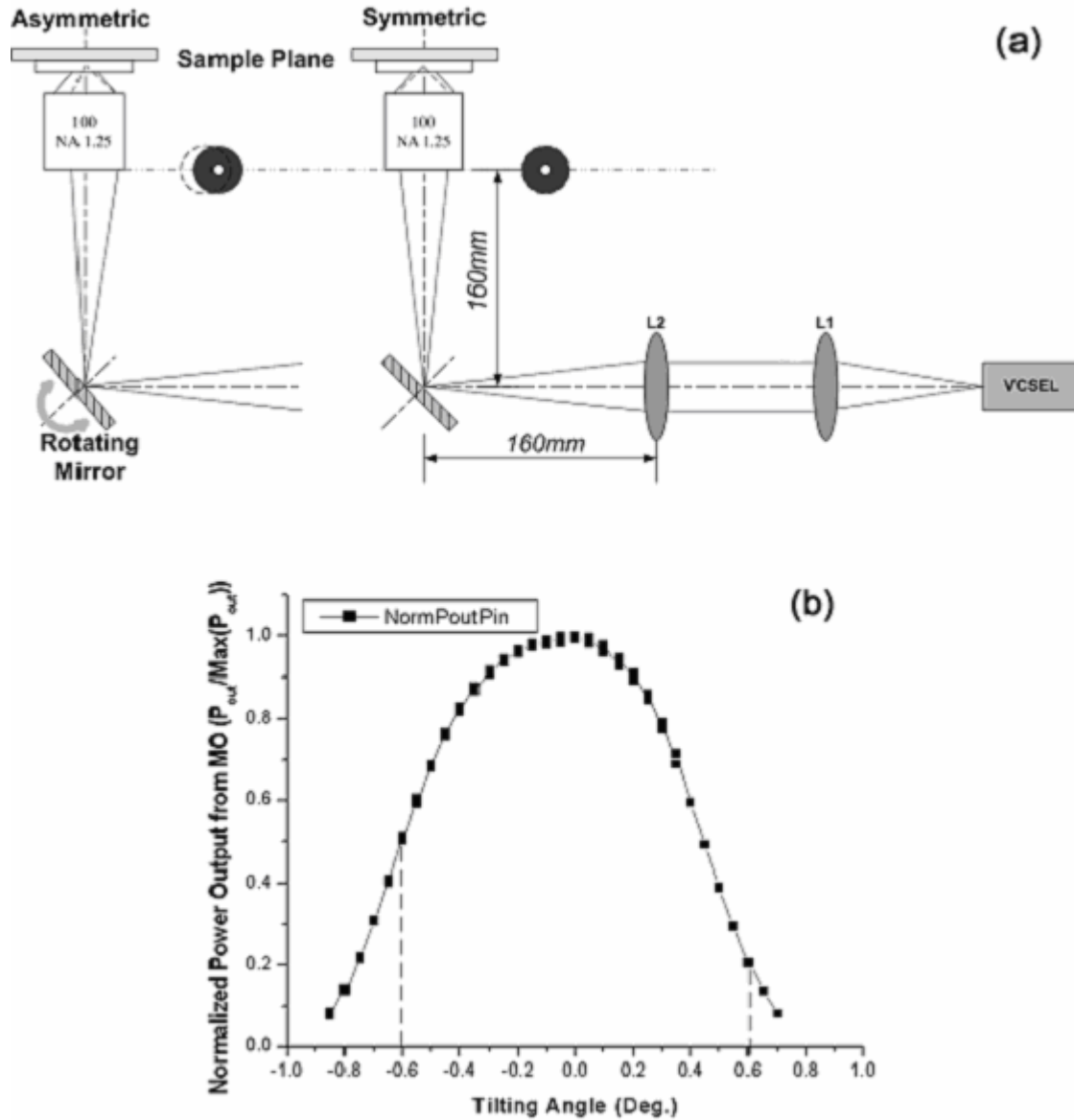


Figure 5-2: Asymmetric beam experiment with a fixed microscope objective. (a) Experimental setup, (b) Power throughput vs. tilting angle.

The degradation of trapping performance might arise either from a decreased incident power or from the asymmetry of the input beam. To investigate the pure effect of beam symmetry on optical trap, it is necessary to eliminate the effect of

power clipping. In the experimental setup shown in Figure 5-3(a) the microscope objective is translated to compensate the shift of beam spot at back aperture during mirror tilting. Under this condition, complete power filling is maintained throughout the whole angular range, and the only thing changes is the orientation of beam out of objective, i.e. beam symmetry (Figure 5-3(a)). The corresponding relationship between power throughput and the tilt angle is shown in Figure 5-3(b). Except for a little variation, the uniformity of power throughput is better than 92%, and strong trap is available in a much larger angle range.

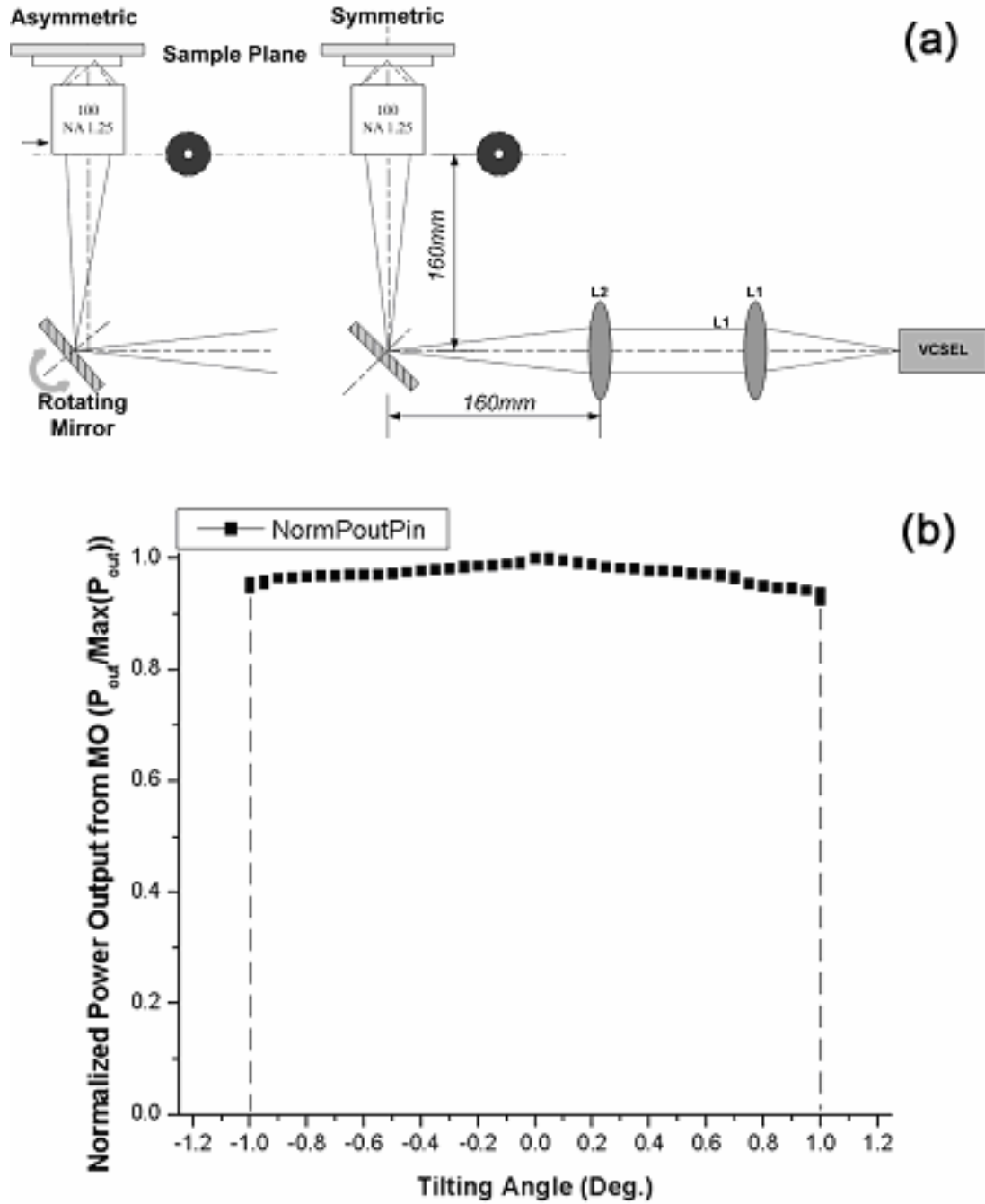


Figure 5-3: Asymmetric beam experiment with movable microscope objective. (a) Experimental setup, (b) Power throughput vs. tilting angle.

The above experiments showed that as long as the back aperture of microscope objective is filled completely, beam symmetry is not indispensable for stable trapping at small input angles. Making all the incoming beams pivot around the effective back focal plane of objective is the necessary condition for getting symmetrical output beam regardless of incident angle. However, it inevitably leads to a considerable reduction of the effective NA used in trapping, and significantly reduces the trapping performance. Accordingly, the guideline for multiplexing optical tweezers is to make the incident light pivot around the back aperture of the microscope objective instead of the effective back focal plane, such that a complete power filling could be retained.

5.3 Optical system design

5.3.1 Two-Dimensional Agile Laser Tweezers Array

To integrate the micromanipulator into a Nikon Eclipse TE200 inverted microscope, an infinity- corrected objective that requires collimated incident light is used. Accordingly, telescope optics are used in the system to serve four functions: keeping the incident light collimated, imaging the multiplexing plane (reflecting surface of the tilting mirror as shown in Figure 5-4) to the back aperture of the microscope objective and adjusting the angular resolution and the beam size.

According to Figure 5-4, the relationship between the shift δ of the laser trap on the specimen plane and the rotation angle θ_l of the mirror is:

$$\delta = -2f_{EFL}(f_a / f_b)\theta_l \quad (5.1)$$

where f_{EFL} is the effective focal length of the microscope objective, f_a, f_b are the focal length of L_a and L_b , respectively.

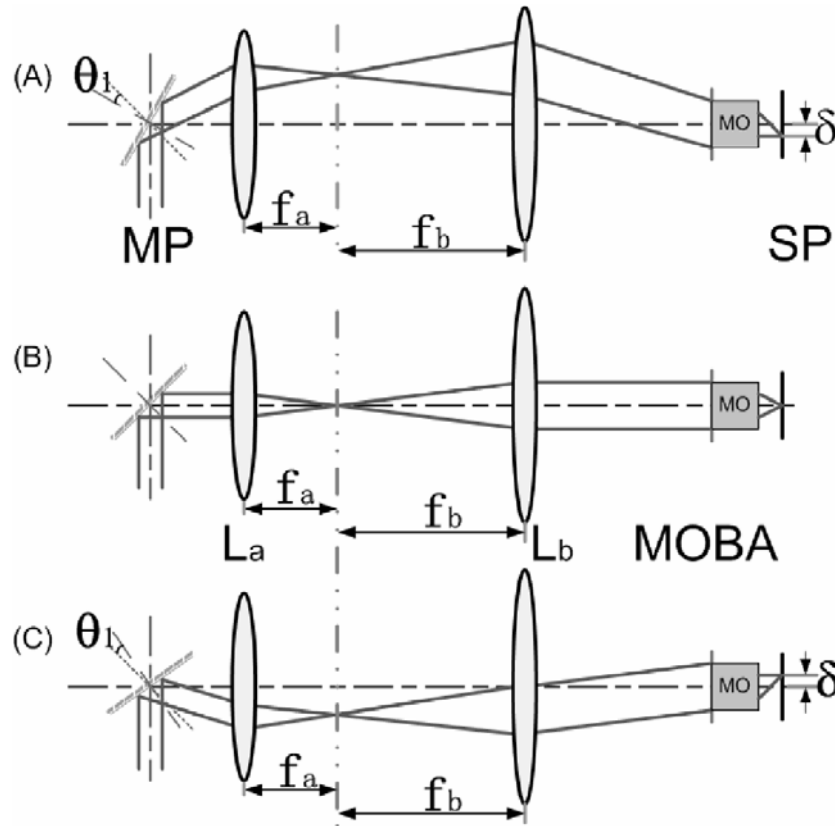


Figure 5-4: Experimental schemes for beam deflection. (A) Mirror is tilted upward and trapping beam is tilted downward. (B) Mirror is not tilted and trapping beam is normal to the specimen plane. (C) Mirror is tilted downward and trapping beam is tilted upward. L_a – first telescope lens; L_b – second telescope lens, MP—multiplexing plane, MOBA -- microscope objective back aperture, MO – microscope objective, SP – specimen plane.

The beam size at the back aperture of the objective is determined as:

$$D_o = D_M f_b / f_a \quad (5.2)$$

where D_M is the beam size at the multiplexing plane.

To have a simultaneously controlled 2-D agile optical trap array, each incoming beam from the laser array is required to completely fill the back aperture of the objective, thus all beams should overlap at the multiplexing plane that is conjugated to the objective back aperture. In Figure 5-5, the multiplexing plane is located at the back focal plane of the collimating lens CL, so that all beams coming from the laser array pass through the same area of the objective back aperture. Simulation of the spot diagrams at the microscope objective back aperture with a 4μ 4 VCSEL array (Code V, Optical Research Associates, Pasadena, CA) shows a centroid displacement smaller than 0.35% for each beam when the mirror is tilted from -2° to $+2^\circ$. Different from previous design where the size of the usable VCSEL array is limited by power clipping at back aperture, this new scheme maintains negligible power clipping regardless of the dimension of the VCSEL array.

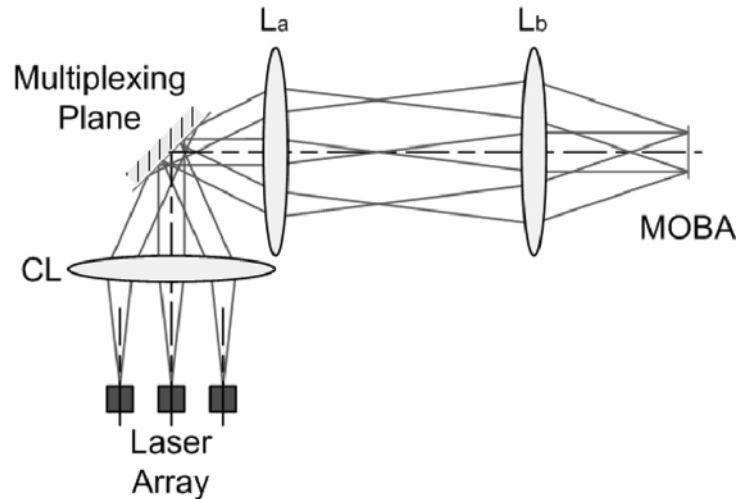


Figure 5-5: Experimental scheme for agile optical tweezers array. CL – collimating lens, L_a -- first telescope lens, L_b -- second telescope lens, MOBA -- microscope objective back aperture.

5.3.2 Depth Adjustable Laser Tweezers

Depth adjustment is an essential feature of 3-D agile laser tweezers. It can be realized by slightly varying the collimation degree of the incident beam. By tuning the spacing between a second pair of lenses (L_1 and L_2) placed in front of the telescope system (L_a and L_b), the beam incident into the microscope objective can change from collimated to slightly convergent or divergent (Figure 5-6).

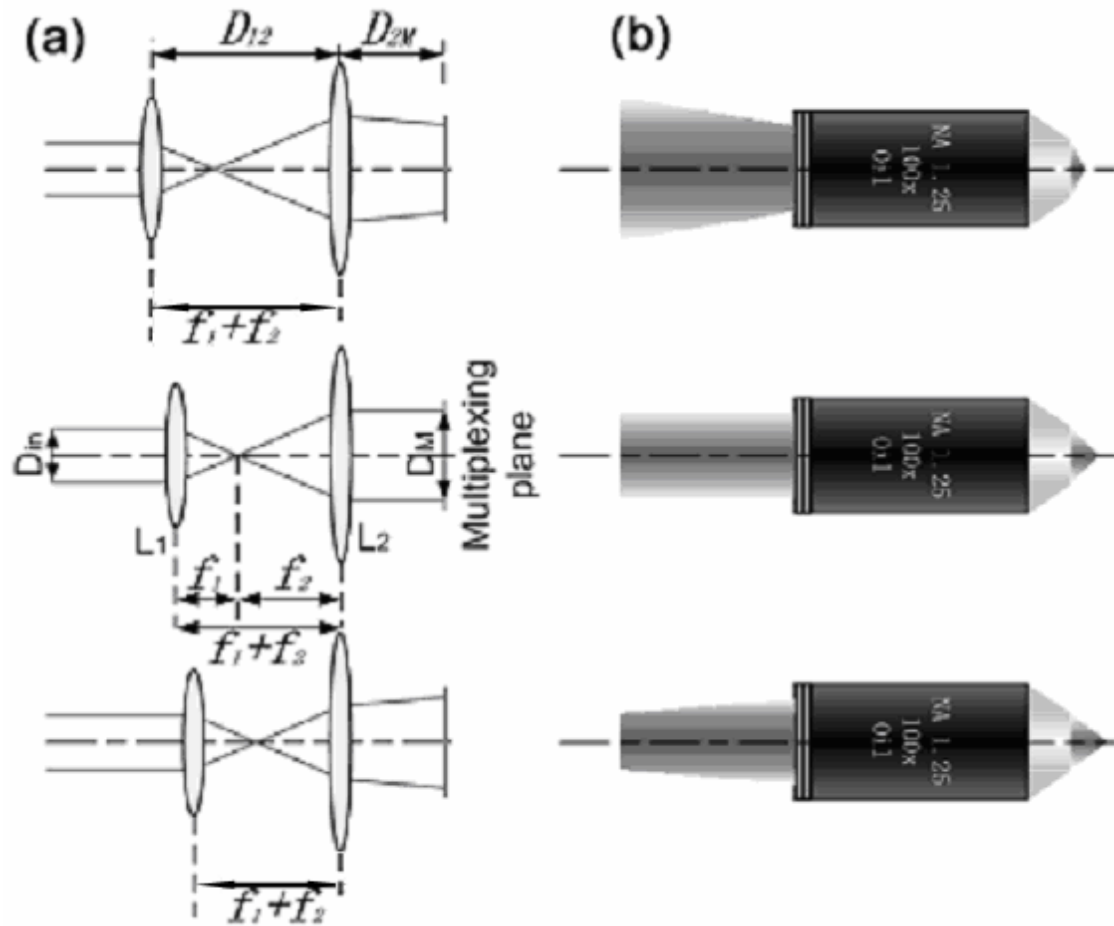


Figure 5-6: Depth adjustment in laser tweezers. (a) Lens pair with adjustable spacing in front of the telescope system. (b) Depth adjustment of objective focus.
 D_{in} – input beam diameter, D_M – beam diameter at multiplexing plane.

Stable trapping is ensured by filling the back aperture completely regardless of the change in the collimation degree. Accordingly to thin lens theory¹⁹, the relation between the beam size at the multiplexing plane D_M and that of the incoming beam D_{in} is derived as:

$$D_M = \frac{d_{2M}f_2 - (d_{12} - f_1)(d_{2M} - f_2)}{f_1f_2} D_{in} \quad (5.3)$$

where d_{2M} is the distance between L_2 and the multiplexing plane, d_{12} is the separation between L_1 and L_2 , f_1 and f_2 are the focal lengths of L_1 and L_2 , respectively. Equation (5.3) shows that to have D_M independent of the collimation degree of the incident light (which is controlled by d_{12}), d_{2M} should be equal to f_2 . When this condition is satisfied, $D_M = \frac{f_2}{f_1} D_{in}$, and $D_o = \frac{f_b}{f_a} \frac{f_2}{f_1} D_{in}$. Simulation on optics designed accordingly provides a spot size variation smaller than 0.02% at the back aperture of the objective for a z-direction displacement of L_1 1 mm (ZEMAX, ZEMAX Development Corporation, San Diego, CA). The variation of trapping depth around the specimen plane ΔZ_s can now be shown to relate to the axial shift of the first lens ΔZ_l by:

$$\Delta Z_s = \left(\frac{f_{EFL}}{f_b} \right)^2 \left(\frac{f_a}{f_2} \right)^2 \Delta Z_l \quad (5.4)$$

5.3.3 Independent Control of Multiple Laser Tweezers

To obtain independent control of laser traps, multiple trapping beams are required to enter the objective while each of them should be able to be moved around in the sample plane without affecting others. Therefore, each beam should obey the rule of laser trap multiplexing, i.e. pivot around the objective back aperture with complete power filling regardless of the incident angle, so that stable traps can be obtained. In this case, any multiplexing plane should be imaged to the back aperture, which implies that a beam-merging device must be employed before the microscope

objective. In our system, a polarizing beam splitter merges laser beams from two branches with orthogonal polarizations, allowing both beams to pivot around the objective back aperture.

5.4 Experiments

5.4.1 Experimental Setup

Based on the optical design presented in section 5.3, a microscope-integrated micromanipulator consisting of a single VCSEL and a $4\mu\text{m}$ VCSEL array (both from Honeywell EM, Santa Clara, CA, wavelength 850 nm) is constructed. The system is built around a Nikon Eclipse TE200 inverted microscope and a Nikon CFI Achromat 100μ oil immersion objective (1.25 NA, working distance 0.17mm) is used for optical trapping. The dichroic mirror and broad band lenses are from Thorlabs (Newton, NJ), the NIR reflecting mirrors are from New Focus (San Jose, CA), and the $4\mu\text{m}$ VCSEL array is fitted with a microlens array from Weible OpTech (Neuchatel, Switzerland).

The complete experimental optical setup is shown in Figure 5-7. For clarity, only the chief rays are shown for the VCSEL array branch. The focal lengths of telescope lens L_a and L_b are $f_a=f_b=160\text{ mm}$ to make $D_O=D_M$. By choosing $d_{Ma}=d_{bO}=160\text{ mm}$, where d_{Ma} is the separation between the multiplexing plane and L_a , a $4-f$ system is created. The tilting mirrors are imaged to the objective back aperture and the effective focal length of the microscope objective is $f_{EFL} = f_{tube}/M = 200/100 = 2.0\text{mm}$, where M is the magnification and f_{tube} is the focal length of tube lens. According to equation (5.1), for each branch, a mirror tilting of $2\pm$

induces a trapping spot shift of 140 microns in the specimen plane. The uniformity of the power measured at objective back aperture is better than 85% of the peak power.

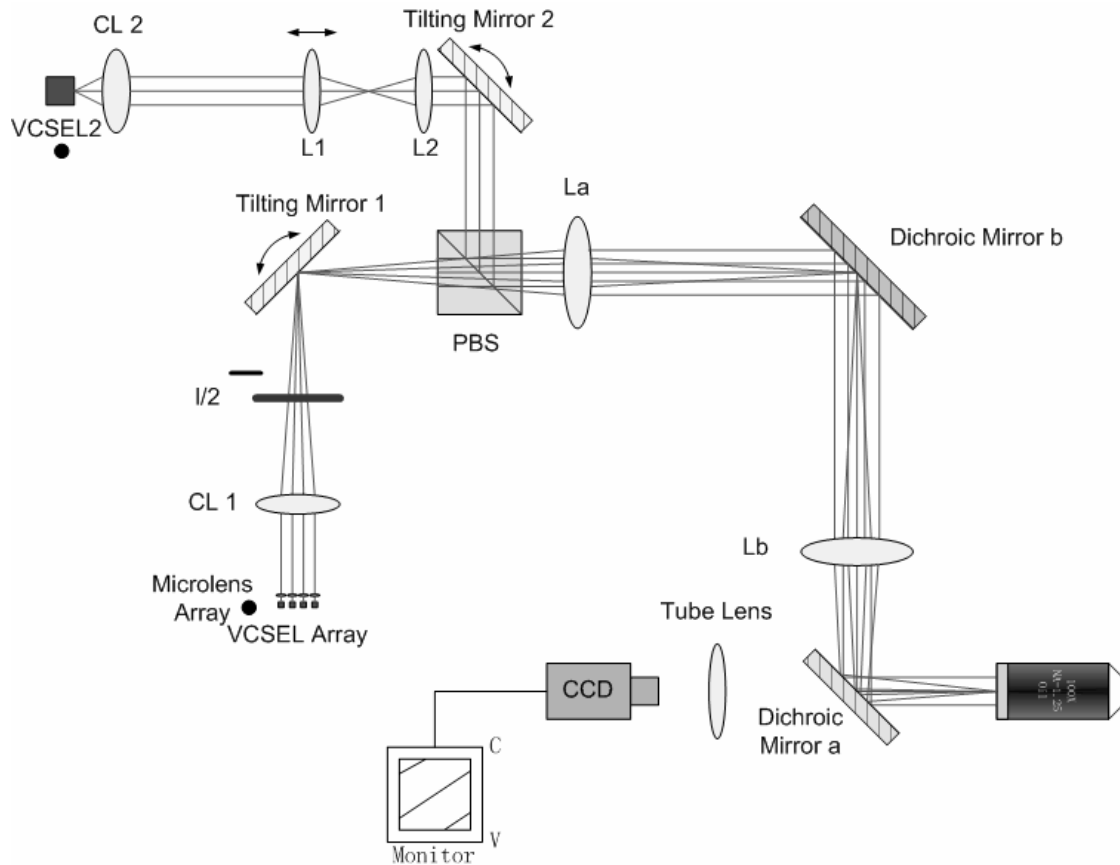


Figure 5-7: Experimental setup of microscope-integrated micromanipulator based on VCSELs. CL 1, CL 2---collimating lenses, $\lambda/2$ ---half wave plate, PBS---polarizing beam splitter.

Depth adjustment of the single trap with respect to the trap array is carried out by moving the lens L_1 along z-direction (Figure 5-7). For multiplexing, a half wave plate is used to make the polarization direction in one branch orthogonal to the other. A dichroic mirror is then placed under the inverted microscope objective to reflect the

impinging near infrared light for trapping and to transmit the visible light for CCD imaging at the camera port of the microscope pedestal. The sample holder consists of one 1-mm-thick glass slide and one 80-micron thick glass coverslip separated by a 150-micron-thick plastic film spacer.

5.4.2 Sample Preparation

Yeast cells are obtained from bread powder, dissolved in DI water and diluted to an appropriate concentration. The PC-12 cells are harvested from a rat adrenal gland and stored in Dulbecco's Modified Eagle Medium (DMEM) with 10% fetal bovine serum (FBS). Polystyrene microspheres (Duke Scientific, Palo Alto, CA) are used for calibration of depth adjustment.

5.4.3 Experimental Results

Experiments on depth adjustment using 5 μm polystyrene beads in DI water show that in the vicinity of the sample plane, a larger trapping depth results in stronger trapping. Moving L_1 along optical axis for 2 mm results in a depth shift of approximate 14 microns (Figure 5-8), and the difference of escape velocity between the maximal and minimal trapping depth can be as large as 5 times. When the measured laser power at the objective back aperture is 3.5 mW, the escape velocity of the trapped bead is 50 $\mu\text{m/s}$ for the deepest trapping, corresponding to a trapping force of 2.4 pN, while 10 $\mu\text{m/s}$ for the shallowest trapping, corresponding to a trapping force of 0.5 pN.

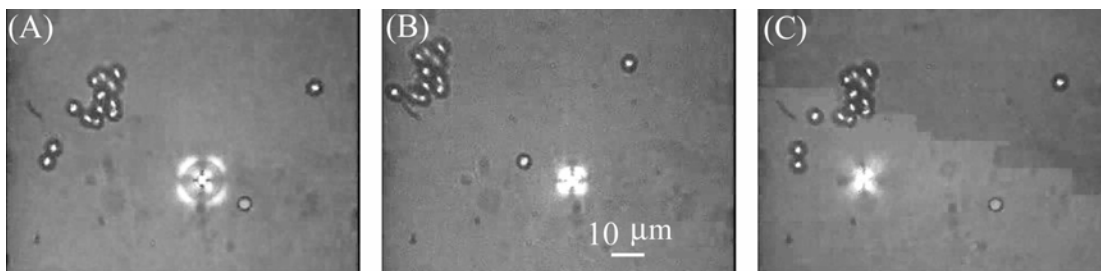


Figure 5-8: Depth adjustment of VCSEL tweezers while trapping a 5 μm polystyrene microsphere. (A) Trapping at the maximal depth, which is about 7 μm under the origin on the specimen plane. (B) Trapping at the original depth, which corresponds to the location of the specimen plane. (C) Trapping at the minimal depth, which is about 7 μm above the specimen plane.

An experiment on intra-array shift showed that particles could be relocated inside an array by switching on and off adjacent components in the VCSEL array. Figure 5-9 shows the shift of a 4 μm polystyrene bead (inside white circle) from the 1st component to the 10th component in a VCSEL-trap array.

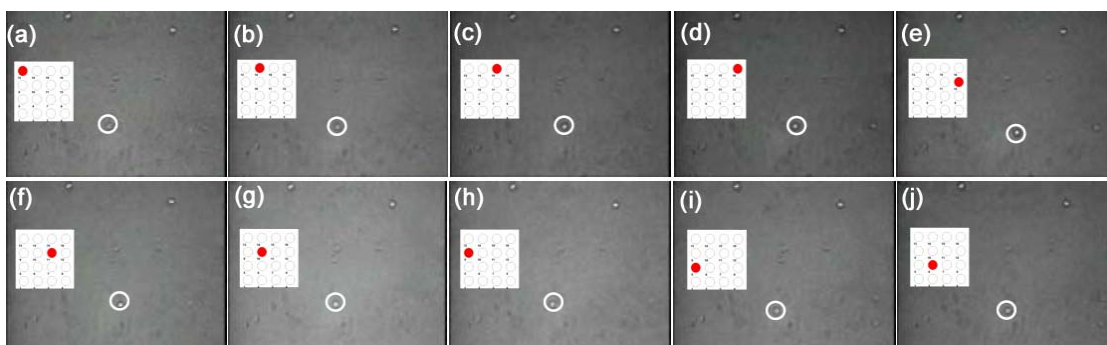


Figure 5-9: Intra-array shift of a 4 μm bead in DI water. Inset: corresponding ON VCSEL in the 4 \times 4 VCSEL array.

In the experiment of multi-object manipulation, the polarization variation of the laser beams originating from the $4\mu 4$ VCSEL array (Figure 5-10(a)) decrease the actual number of VCSELs available for trapping in the present system (Figure 5-10(b)). To ensure stable and interference-free traps, a conservative minimum trap separation of 1.5 times the microsphere diameter is required. For a VCSEL array with 250- μm pitch, the resultant inter-tweezers spacing on the specimen plane is 3.33

$$\text{microns (determined by the optics: } p_S = p_{VA} \cdot \frac{f_a}{f_{CL}} \cdot \frac{f_{EFL}}{f_b} = 250 \times \frac{160}{150} \times \frac{2.0}{160} = 3.33 \mu\text{m} ,$$

where p_S is the pitch on the specimen plane, and p_{VA} is the pitch on the VCSEL array, f_{CL} is the focal length of the collimating lens). All the factors mentioned above limited the number of active tweezers in the array. As a demonstration, an arbitrary trapping pattern satisfying the above conditions is used (Figure 5-10(c)) and the power at the objective back aperture for each corresponding VCSEL beam is approximately 3.5 mW.

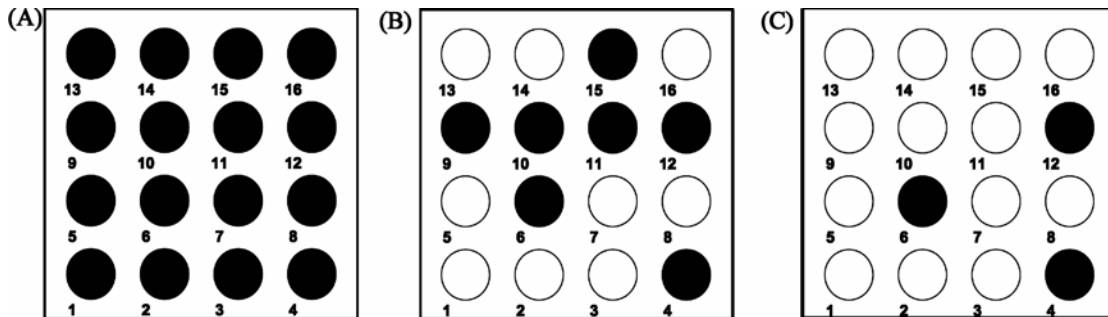


Figure 5-10: $4\mu 4$ VCSEL array used for microscope-integrated manipulator. (A) Layout of an ideal VCSEL array with all 16 VCSEL illuminating. (B) In the VCSEL array we used, only those VCSELs marked as black have appropriate polarization direction (polarization orthogonal to that of the single VCSEL used in the system). (C) VCSELs selected for the demonstration of micromanipulator.

During the operation of the micro-manipulator, the single VCSEL trap can collect multiple cells from various part of the specimen plane, and locate them to the trapping spots defined by the VCSEL array. After all the cells are trapped by the VCSEL array, they can be transported around the specimen plane as a group by tilting the mirror 1 (Figure 5-7). Finally, the single VCSEL trap can be used to disband the group by delivering cells to different locations. Figure 5-11 shows some frames extracted from a video clip taken in the micromanipulation experiment, where 3 yeast cells are collected, grouped into a triangle, transported around and dismissed. The different appearance between the single VCSEL trap and the VCSEL array traps on the frame is the result of depolarization introduced by a high NA objective.²⁰

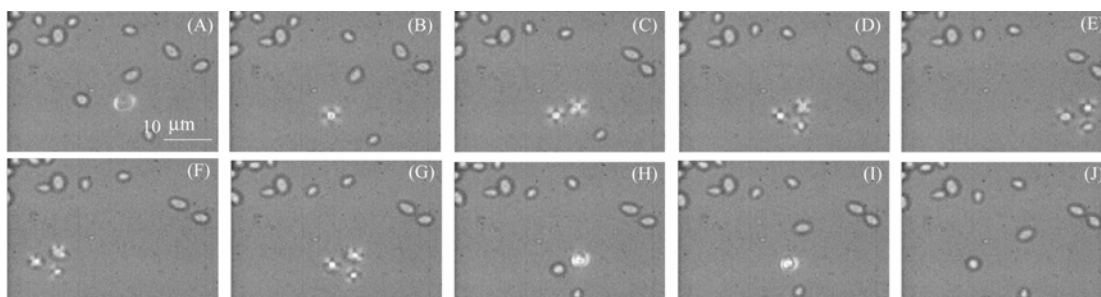


Figure 5-11: Frames from micromanipulation experiment. (A) Initial state, (B) - (D) Single VCSEL tweezers collects 3 yeast cells and form them into a predefined array trapped by a VCSEL tweezers array, (E) - (G) Cell group is transported by agile VCSEL tweezers array, (H) - (J) Cell group is disbanded by single VCSEL tweezers.

With the single VCSEL and one component from the VCSEL array, rotation of cells can also be achieved. In Figure 5-12(A1-A5), a pair of conglutinated yeast cells is rotated by trapping one cell with a fixed VCSEL trap and orbiting the other laterally

around the static one with an agile VCSEL trap. The measured angular velocity is approximately 0.22 rad/s. In Figure 5-12(B1-B5), a single PC-12 cell (Pheochromocytoma nervonal cells from rat adrenal gland, stored in DMEM with 10% FBS) is rotated in the same way at an angular velocity of 0.02 rad/s, except that, in this case, each VCSEL tweezers focused on each end of the single cell.

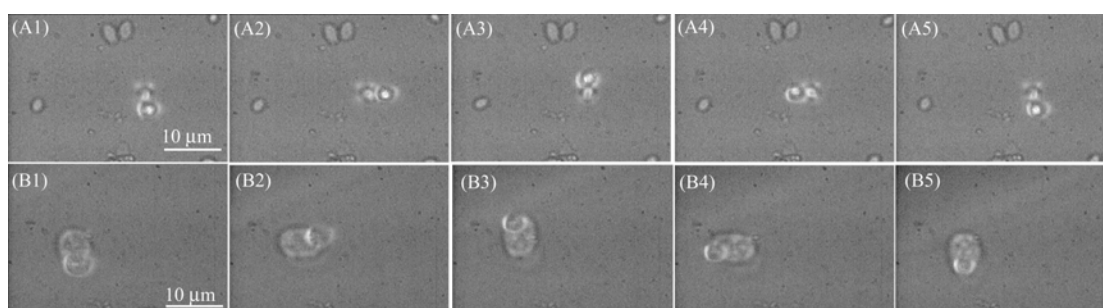


Figure 5-12: Cell rotation with VCSEL tweezers. (A1-A5) Rotation of a pair of yeast cells counter-clockwise with double VCSEL traps. (B1-B5) Rotation of a PC-12 cell counter-clockwise with double VCSEL traps.

5.5 Discussion

The VCSEL-based micromanipulator shows great promise for various applications in biomedical fields. With the aid of microfluidic channels, the independently controlled multiple optical tweezers can be used to build biomolecule-DNA networks, where nanoscale molecules like DNAs are manipulated by laser traps via attaching to microparticles, such as polystyrene spheres. Following the operation procedure similar to the demonstrated experiments, group reactions can be facilitated

for cellular assay, diagnostics and drug screening. The 3-D mobility and rotation ability of the micromanipulator make it possible to be combined with dielectrophoresis (DEP) to facilitate and improve the investigation of protein-ligand interaction.²¹ In this case, multiple pairs of protein-ligand interaction could be studied simultaneously, and to get a protein interact with a different ligand on the other side of a cell, it is no longer necessary to change the phase of the AC field to rotate the cell, instead, a laser trap could transport the protein carrier to the specified location and let the interaction occur. The study of RNA folding/unfolding kinetics²² with nanopores could also be made more efficient with two independent optical tweezers working in opposite directions.

Recently, an optically actuated parallel near-field scanning optical microscopy (NSOM)²³ where microlenses are introduced into a microfluidic environment for measurement and high resolution biological imaging has been developed. Substituting the cells in our micromanipulator system with solid immersion lenses (SIL) will bring significant improvements to the optically actuated parallel NSOM by allowing independent, mobile measurement and imaging. Powered up with a VCSEL array and a large number of independently controlled SILs, the novel microscope can be expected to have enhanced resolution at multiple points of interest.

In future research, substituting the tilting mirrors with 2-D MEMS mirrors will afford faster, programmable, more accurate and quantitative performance of the micromanipulator system. The combination of a micromirror array and a VCSEL

array should enable individual operation of the optical tweezers in an array. To expand the trapping dimension or enhance the efficiency of parallel operation on multiple micro-objects, two independently controlled optical tweezers array could be built with two VCSEL arrays.

5.6 Conclusions

In this chapter, a microscope-integrated micromanipulator is designed and developed to realize independently controlled agile laser traps on a static sample plane according to the requirements of micro-particle manipulation in micro-fluidic system (minimized background flow and control flexibility). The manipulator consists of a single 3-D agile VCSEL tweezers and an array of VCSEL tweezers, and each of them is controlled independently by a tilting mirror. The optical system is designed to sustain constant and complete power filling at the microscope objective back aperture rather than persist in beam symmetry for stable trapping. Experiments including collection, grouping, transportation, disbandment and rotation of biological cells are demonstrated.

5.7 Acknowledgements

Sanja Zlatanovic is acknowledged for her collaboration on the experiments performed in this chapter along with co-authoring the publications that resulted from this research.

Dr. Sadik Esener is acknowledged for his innovative ideas concerning this research.

Thomas Pisanic is acknowledged for providing PC-12 cell samples.

In addition, we would like to thank all the coauthors of our publications relating to this research, Dr. Mihrimah Ozkan and Dr. Aaron Birkbeck.

Lastly, we would like to acknowledge the Defense Advanced Research Project Administration (DARPA) via the CHIPS Opto-Center and the University of California, San Diego for funding this research.

Sections 5.2, 5.3, and 5.4 of this chapter, in part, are a reprint of material as it appears in "Microscope-integrated micromanipulation based on multiple VCSEL traps," by B. Shao, S. Zlatanovic, and S. C. Esener, Proceedings of the SPIE, v5514, p62, SPIE 49th Annual Meeting, Denver, Colorado, USA, Aug. 2-6, 2004.

Sections 5.3 and 5.4 of this chapter, in part, are a reprint of material as it appears in, "Manipulation of microspheres and biological cells with multiple agile VCSEL traps," by B. Shao, S. Zlatanovic, M. Ozkan, A. Birkbeck, and S. C. Esener, *Sensors and Actuators, B, Chem*, v113, n2, p866-874, 2006.

5.8 References

1. A. Ashkin, "Acceleration and trapping of particles by radiation pressure," *Phys. Rev. Lett.* **24**, 156-159 (1970).
2. A. Ashkin, J. M. Dziedzic, J. E. Bjorkholm, and S. Chu, "Observation of a single-beam gradient force optical trap for dielectric particles," *Optics Letters* **11**, 288-290 (1986).
3. M. W. Berns, "Laser scissors and tweezers," *Scientific American (International Edition)* **278**, 52-57 (1998).
4. M. Ozkan, M. M. Wang, C. Ozkan, R. A. Flynn, and S. Esener, "Optical manipulation of objects and biological cells in microfluidic devices," *Biomedical Microdevices* **5**, 47-54 (2003).

5. M. Ozkan, T. Pisanic, J. Sheel, C. Barrow, S. C. Esener, and S. Bhatia, "Electro-Optical Platform for the Manipulation of Live Cells," *Langmuir* **19**, 1532-1538 (2003).
6. K. Hirano and Y. Baba, "Manipulation of single coiled DNA molecules by laser clustering of microparticles," *Applied Physics Letters* **80**, 515-517 (2002).
7. R. A. Flynn, A. L. Birkbeck, M. Gross, M. Ozkan, B. Shao, M. M. Wang, and S. C. Esener, "Parallel transport of biological cells using individually addressable VCSEL arrays as optical tweezers," *Sensors and Actuators, B, Chem* **87**, 239-243 (2002).
8. A. L. Birkbeck, R. A. Flynn, M. Ozkan, D. Song, M. Gross, and S.C. Esener, "VCSEL arrays as micromanipulators in chip-based biosystems," *Biomedical Microdevices* **5**(1), 47-54 (2003).
9. G. Leitz, E. Fallman, S. Tuck, and O. Axner, "Stress response in *Caenorhabditis elegans* caused by optical tweezers: wavelength, power, and time dependence," *Biophys. J.* **82**, 2224-2231 (2002).
10. K. C. Neuman, E. H. Chadd, G. F. Liou, K. Bergman, and S. M. Block, "Characterization of photodamage to *Escherichia coli* in optical traps," *Biophys. J.* **77**, 2856-2863 (1999).
11. H. Schneckenburger, A. Hendinger, R. Sailer, M. H. Gschwend, W. S. L. Strauss, M. Bauer, and K. Schutze, "Cell viability in optical tweezers: high power red laser diode versus Nd: YAG laser," *Journal of Biomedical Optics* **5**, 40-44 (2000).
12. Z. X. Zhang, G. J. Sonek, X. B. Wei, C. Sun, M. W. Berns, and B. J. Tromberg, "Cell viability and DNA denaturation measurements by two-photon fluorescence excitation in cw Al: GaAs diode laser optical traps," *Journal of Biomedical Optics* **4**, 256-259 (1999).
13. A. T. O'Neil and M. J. Padgett, "Axial and lateral trapping efficiency of Laguerre-Gaussian modes in inverted optical tweezers," *Optics Communications* **193**, 45-50 (2001).
14. Y. Ogura, K. Kagawa, and J. Tanida, "Optical Manipulation of Microscopic Objects by Means of Vertical-Cavity Surface-Emitting Laser Array Sources," *Applied Optics* **40**, 5430-5435 (2001).
15. P. C. Mogensen and J. Gluckstad, "Dynamic array generation and pattern formation for optical tweezers," *Optics Communications* **175**, 75-81 (2000).

16. K. Visscher, S. Gross, and S. Block, "Construction of multiple-beam optical traps with nanometer-resolution position sensing," *IEEE Journal of Selected Topics in Quantum Electronics* **2**, 1066-1076 (1996).
17. C. Mio, T. Gong, A. Terray, and D. Marr, "Design of a scanning laser optical trap for multiparticle manipulation," *Review of Scientific Instruments* **71**, 2196-2200 (2000).
18. B. Shao, S. Zlatanovic, and S. C. Esener, "Microscope-integrated micromanipulation based on multiple VCSEL traps," presented at the Optical Trapping and Optical Manipulation, Denver, Colorado, 2004.
19. E. Hecht, *Optics*, 2nd ed. (Addison-Wesley, 1990).
20. L. Novotny, R. D. Grober, and K. Karrai, "Reflected image of a strongly focused spot," *Optics Letters* **26**, 789-791 (2001).
21. C. Reichle, K. Sparbier, T. Muller, T. Schnelle, P. Walden, and G. Fuhr, "Combined laser tweezers and dielectric field cage for the analysis of receptor-ligand interactions on single cells," *Electrophoresis* **22**, 272-282 (2001).
22. U. Gerland, R. Bundschuh, and T. Hwa, "Mechanical pulling through a nanopore can reveal the secondary structure of single RNA molecules," *Soft Condensed Matter* **1**, 1-9 (2003).
23. A. L. Birkbeck, S. Zlatanovic, M. Ozkan, and S. C. Esener, "Laser tweezer controlled solid immersion lens for high resolution imaging in microfluidic and biological samples," presented at the Proceedings of SPIE, Smart Materials, Nano-, and Micro- Smart Systems, Perth, Australia, Dec. 10, 2003, 2003.

6. Conclusions and Outlook

6.1. Conclusions

The central focus of this dissertation is to provide new information (submicron to micron-sized cell characterization, self-propelled cell analysis) and improvement (high throughput) to noninvasive manipulation and analysis of biological objects with optical scattering techniques. Toward this goal, the use of angularly-dependent light scattering for submicron-cell characterization, the employment of an annular laser trapping based on axicons for self-propelled cell analysis, and the utilization of vertical cavity surface emitting laser arrays (VCSEL arrays) for improving the throughput and flexibility of biological-object manipulation have been demonstrated.

Chapter 2 laid the theoretical groundwork for the use of light scattering and optical trapping throughout the dissertation. The basic physics were explained. The relationship between light scattering and optical force were emphasized. After reviewing the theories of light scattering in three size regimes, generalized Lorentz-Mie theory (GLMT) for solid sphere and its extension to coated-sphere and solid spheroid were depicted. Various physical models that have been used to describe optical traps were laid out, according to the different particle size regimes that give rise to different assumptions. Finally, a brief overview was given on the applications of optical trap in biomedical research.

Chapter 3 demonstrated the application of elastic light scattering for submicron to micron-sized cell characterization. To be specific, in pursuit of a rapid, simple, and

inexpensive *in situ* instrument for ocean microbes classification, which is an important problem in oceanic microbial ecology, the use of angularly resolved light scattering in order to identify different groups of picoplankton was explored. Scattered light from suspensions of three types of marine picoplankton: *Synechococcus sp.* strain CC9311, *Ostreococcus sp.* strain CCE9901 and *Flavobacterium sp.* strain ALC1 was collected over the region of $0.5 - 179.5^\circ$ with a resolution of 0.5° . The signal to noise ratio of the scattering pattern in the middle angular range ($40 - 140^\circ$) was high enough to allow for cell characterization. Computer simulations employed a hybrid algorithm that combined Generalized Lorentz-Mie Theory (GLMT) and the Rayleigh-Debye method (RM-I). Prokaryotes cells were approximated as homogeneous spheroids, whereas the picoeukaryote was modeled with an extended RM-I method that was developed for a coated spheroid with a spherical core. Good overall agreement was obtained between predicted and measured scattering patterns. The system's ability to distinguish various marine picoplankton based on their scattering diagram heralds the identification of sub-micron to micron-sized cells with very similar morphology without the use of markers. Potential improvements on system performance are discussed.

In chapter 4, a dynamically resizable three-dimensional annular laser trap system was proposed, which can not only be used to manipulate tens to hundreds of microparticles in parallel, but also promise high-throughput, multi-level sorting of self-propelled cells such as sperm according to their motility and biotropism response. The special optical properties of axicons were used to create a continuous, size tunable annular trap with high power efficiency and constant numerical aperture. Parallel

three-dimensional trapping of microparticles and biological cells proved the performance of the annular traps and their applicability to both inorganic and organic micro-particles. Parallel sorting and swimming pattern analysis of sperm with the annular laser trap were carried out. Compared with single spot laser trap, this new type of laser trap offers a more gentle approach (less laser power per sperm) to sperm analysis, and allows a more detailed investigation on the effect of optical force, laser radiation and external obstacles on sperm swimming pattern and membrane potential (with the aid of specific fluorescence probes). The application could be extended to motility and biotropy studies of other self-propelled cells, such as algae and bacteria.

Toward more parallel and flexible system, chapter 5 described the utilization of VCSEL and VCSEL arrays to forming stable three-dimensional optical traps which can independently and synchronously manipulate biological cells without moving sample plane. VCSEL arrays serve as a valuable optical trapping tool both for creating independently controlled arrays of traps and providing a compact laser light source for miniaturizing optical trap systems. Consisting of a single 3-D agile VCSEL tweezers and an array of VCSEL tweezers, the microscope-integrated micromanipulator developed here is capable of independent control, rotation, and batch processing of biological cells. Based on this research, it will be possible to build a fast hand-held device that can rapidly carry out different types of multi-step manipulation on a group of biological objects.

6.2. Innovative Contributions

6.2.1. Submicron cell characterization with angularly dependent light scattering

- Matlab simulation based on GLMT for homogeneous sphere --- modeling scattering from microspheres
- Matlab simulation based on extended GLMT for coated sphere --- modeling scattering from monodispersed liposome suspension
- Matlab simulation based on polydispersed sample (normal and lognormal distribution) --- modeling scattering from real liposome suspension)
- Matlab simulation based on RM-I for homogeneous spheroid (single orientation) --- modeling scattering from prokaryote cells
- Matlab simulation based on RM-I for homogeneous spheroid (random orientation) --- modeling scattering from prokaryote cells
- Extended RM-I method for coated spheroid with different core shape and shell thickness distributions (uniform shell thickness, spherical core, spheroid core, arbitrary thickness distribution).
- Matlab simulation based on extended RM-I for coated spheroid --- modeling scattering from eukaryote cells
- System calibration with liposome
- High angular resolution ($\approx 0.5^\circ$) in a continuous large angular range ($0.5^\circ - 179.5^\circ$)
- Discriminating particle types according to the shape of scattering diagram in the middle angular range ($40^\circ - 140^\circ$).

6.2.2. Annular laser trap for self-propelled cell analysis

- A new application of axicon in optical trapping --- generating a continuous ring focus with optical gradient force only exist in the radial direction
- A new type of optical trapping capable of manipulating tens to hundreds microparticles in parallel and pattern them into a ring shape
- Creating a force shield (with optical gradient) to prevent analytical field (inside the ring) from unwanted interference
- Spatial confinement for cell division analysis or migration study
- A unique way to confine a swimming cell in the field of view for an extended period of time without having to deal with sharp turns and changes in the swimming curvature.
- A new and more gentle way to study the relationship between the escape trapping power of a sperm and its swimming velocity (low power, dynamical)
- 3-D parallel trapping of microparticles
- Analysis of the 3-D structure of the ring focus
- Analysis of the effect of incident beam profile on the trapping performance of the ring
- Self-propelled cell sorting based on motility and chemotaxis response
- Self-propelled cell swimming pattern analysis under the effect of laser illumination or optical force

- self-propelled cell swimming pattern analysis under the effect of external object and optical force
- Utilizing an axicon lens pair to dynamically resize the annular laser trap for multi-level sorting
- Optical design and simulations
- High power efficiency and no mechanical scan

6.2.3. Micromanipulator based on multiple VCSEL traps

- Experimental analyzing the effect of beam symmetry vs. power clipping on the trapping performance of single spot VCSEL trapping
- 3-D agile VCSEL tweezers with constant power filling at the back aperture of the objective
- Precision pick, place, batch processing and rotation of biological cells without moving the sample container
- Independently-controlled single VCSEL trap and VCSEL trap array work together for multi-step operation on biological cells
- 2-D agile VCSEL tweezers array with negligible power clipping regardless of the dimension of the VCSEL array

6.3. Further Directions

The objective of this dissertation is to develop new technologies for noninvasive characterization and analysis of biological objects with optical scattering techniques, which could bring new information and improvements to biomedical

research. This was established by angularly dependent scattering and micromanipulation with optical forces. Although preliminary results are given for concept proof and possible limitations are addressed, a number of unanswered questions remain as avenues for further research.

For submicron particle characterization with elastic light scattering, based on the preliminary results on liposome, it is possible to conduct scattering measurement on liposome with a series of different sizes and refractive indices (by means of osmoregulation¹) and study the optical changes in unilamllar vesicles experiencing osmotic stress. At the same time, the optical scattering properties of cell membrane could be studied in detail with liposome due to its resemblance to the former. In suspension measurements, fine details of a cell's phase function are lost due to the statistical average of the natural size, shape, orientation, and morphological variations over a population, it is therefore always desirable to measure scattering diagram from a single cell. Since optical trapping of submicron cells is challenged by strong Brownian motion, attaching live cells to a microsphere handle could be a solution. However, the biochemical procedure for attaching a cell without killing it needs to be figured out. Replacing the current 10-mm diameter cuvette with a smaller-diameter container and pass a stream of low concentration cell suspension through the exciting beam is another solution worth trying. With some modifications, the developed system could also be used for studying microbe swimming behavior and orientation. 1/3 of the *Synechococcus* genus has a mysterious form of motility characterized by the ability to swim without flagella.^{2,3} The current scattering setup allow time-dependent

scattering signals at specific angles to be collected. With the help of phase locking or interference technologies⁴, information on microbe swimming could be extracted by comparing the time-dependent scattering from swimming *Synechococcus* and non-swimming ones. This could also be applicable to other self-propelled cells in order to provide additional way for cell motility study. As illustrated in chapter 1, the scattering signature of a nonspherical particle changes with its orientation. If the orientation of biotrophic microbes could be affected by introducing some stimuli, the scattering system could then be used to investigate orientation of spheroid microbes with respect to the stimuli and vice versa to detect the existence and location of stimuli.

Annular laser trapping of sperm and other self-propelled cells should be conducted in a large volume under different conditions (laser power, ring diameter, etc.) so that accurate and reliable conclusions could be obtained on sorting threshold, swimming pattern, and biotropism response, etc. Annular laser trap also has potential applications in studying cell growth and migration. By placing a dividing cell in the cage made of trapped particles, the effect of spatial confinement on cell division could be investigated (Figure 6-1). The migration behavior of fibroblast cells can be affected by environment such as mechanical force, flow, or foreign matter. By changing the trapping pattern from a full circle to an arc (blocking part of the conjugated ring image with a spatial filter), the response of surrounding fibroblast to the change in spatial distribution of foreign matter, in this case trapped beads, could be analyzed (Figure 6-2).

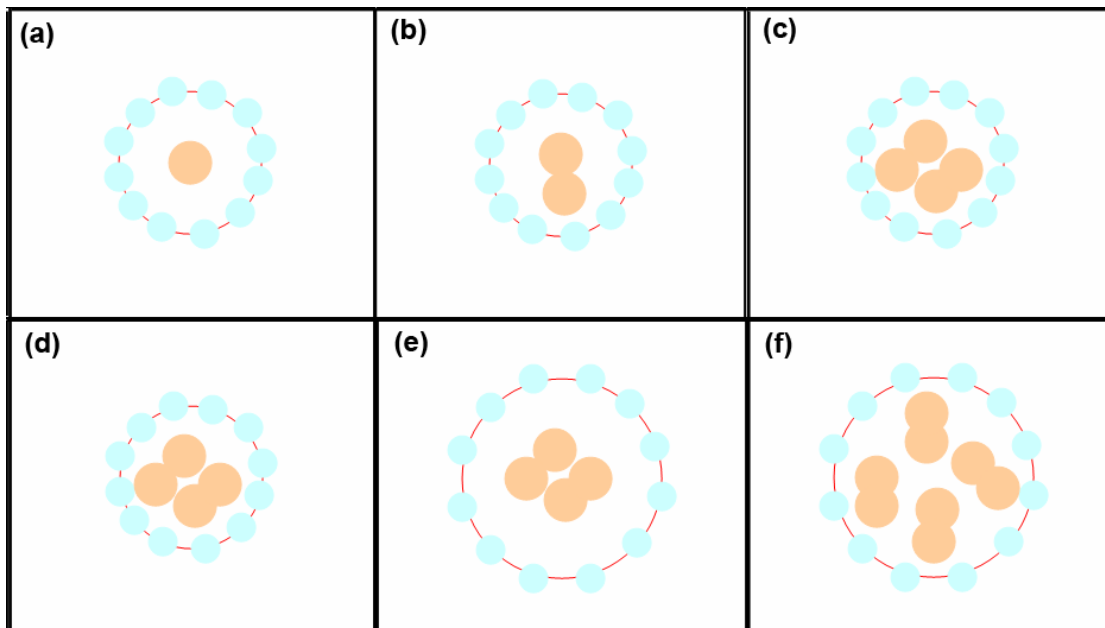


Figure 6-1: Utilizing annular trapped microspheres to impose spatial confinement to cell dividing. (a) A single cell before dividing. (b) - (c) The mother cell is dividend into two daughter cells and then four cells. (d) Due to the spatial confinement imposed by the trapped microspheres, the cells stop dividing. (e) - (f) After the size of the ring is increased, there are more room for cell dividing, and the four cells resume to divide into eight cells.

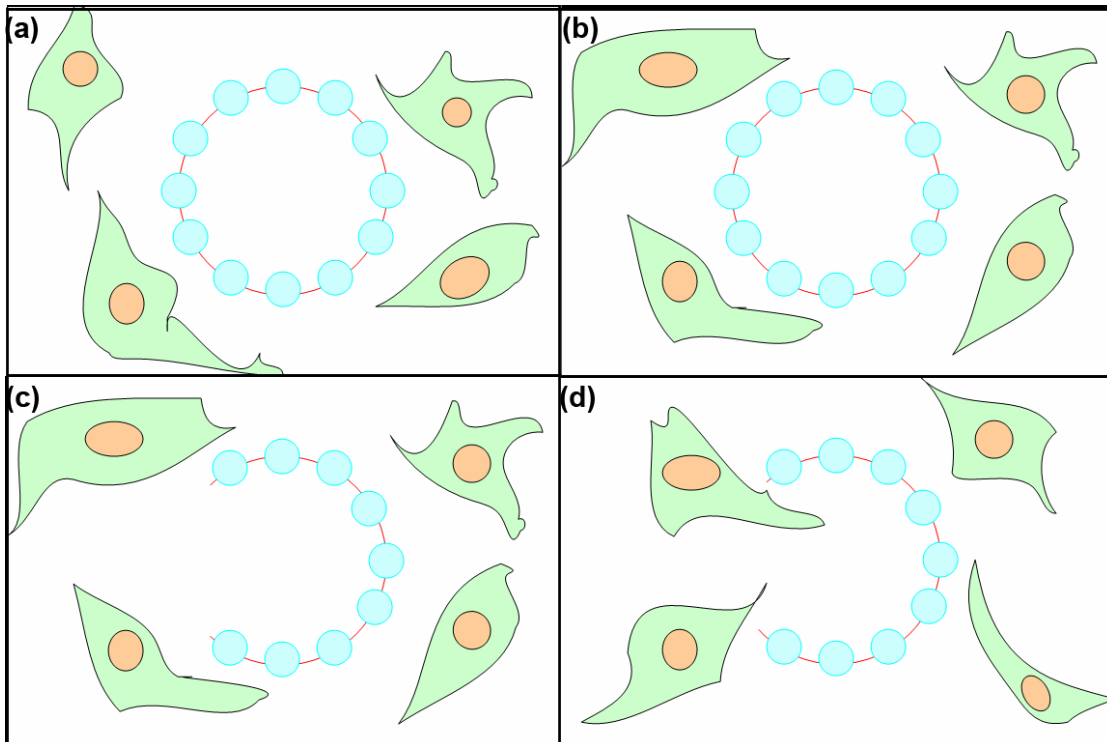


Figure 6-2: Utilizing annular trapped microspheres to impose external obstacle for 3T3 cell migration. (a) - (b) Four 3T3 cells are migrating around the ring of microspheres. (c) Part of the ring trap is blocked so that the fence of microspheres is broken. (d) Without the trapped microspheres as obstacle, 3T3 cells start migrating into the ring.

For the agile manipulation of biological cells using VCSEL array sourced laser optical tweezers, there is always the desire of increasing the dimension and changing the resolution of the VCSEL array such that a larger scale operations is achievable. By replacing the single VCSEL in the micromanipulator with another VCSEL array, a high density, large dimension array of optical traps capable of 2-D scanning can be created (Figure 6-3). This system could be integrated with the annular trap for enhanced cell manipulation. Besides biological objects, micro-optic spatial filter⁵ and

the microfluidic SIL^{6, 7} could be manipulated with this micromanipulator so that spatial filtering operations or imaging operations can be performed in parallel.

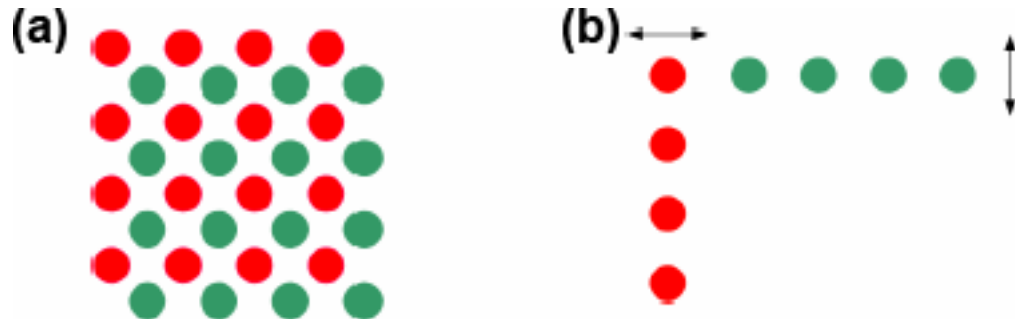


Figure 6-3: Expanding the dimension and resolution of VCSEL tweezers array.
(a) Interlacing two 4 μ 4 VCSEL tweezers array. (b) Scanning two 1 μ 4 VCSEL tweezers array independently in two orthogonal directions.

6.4. References

1. G. White, J. Pencer, B. G. Nickel, J. M. Wood, and F. R. Hallett, "Optical changes in unilamellar vesicles experiencing osmotic stress," *Biophys J.* **71**(5), 2701-2715 (1996).
2. B. Palenik, B. Brahamsha, F. W. Larimer, M. Land, L. Hauser, P. Chain, J. Lamerdin, W. Regala, E. E. Allen, J. McCarren, I. Paulsen, A. Dufresne, F. Partensky, E. A. Webb, and J. Waterbury, "The genome of a motile marine *Synechococcus*," *Nature* **424**(6952), 1037-1042 (2003).
3. N. Touchette, "How the Other Half Lives: Marine Microbes Capture the Limelight" (Genome News Network, 2003), retrieved September 5, 2003, 2003, http://www.genomenewsnetwork.org/articles/09_03/ocean.shtml.
4. S. Sudo, Y. Miyasaka, and K. Otsuka, "Quick and easy measurement of particle size of Brownian particles and plankton in water using a self-mixing laser," *Optics Express* **14**(3), 1044-1054 (2006).
5. A. Birkbeck, S. Zlatanovic, and S. Esener, "Self-Aligned Spatial Filtering Using Laser Optical Tweezers," *Applied Optics* (In press) (2006).

6. A. L. Birkbeck, S. Zlatanovic, M. Ozkan, and S. C. Esener, "Laser tweezer controlled solid immersion lens for high resolution imaging in microfluidic and biological samples," presented at the Proceedings of SPIE, Smart Materials, Nano-, and Micro- Smart Systems, Perth, Australia, Dec. 10, 2003, 2003.
7. A. L. Birkbeck, S. Zlatanovic, S. C. Esener, and M. Ozkan, "Laser-tweezer-controlled solid immersion microscopy in microfluidic systems," *Optics Letters* **30**(20), 2712-2714 (2005).